2011

3D Quantification of Particle Interaction of Compacted Powders Using Synchrotron Micro Tomography (SMT)

Md. Nafiul Haque
Louisiana State University and Agricultural and Mechanical College, mhaque3@tigers.lsu.edu

3D QUANTIFICATION OF PARTICLE INTERACTION OF COMPACTED POWDERS USING SYNCHROTRON MICRO TOMOGRAPHY (SMT)

A Thesis

Submitted to the Graduate Faculty of the
Louisiana State University and
Agricultural and Mechanical College
in partial fulfillment of the
requirements for the degree of
Master of Science in Civil Engineering

in

The Department of Civil and Environmental Engineering

By
Md. Nafiul Haque
B.Sc. Bangladesh University of Engineering and Technology, 2008
December 2011

This thesis is dedicated

To my mother Nargis Akther

ACKNOWLEDGEMENTS

This thesis is a result of years of research accomplished since I joined Louisiana State University. The preparation of this thesis was made possible through the support, hard work, and endless effort of a large number of individuals and institutions. It is a pleasure to convey my gratitude to them all in my humble acknowledgement. First of all, my profound appreciation goes to God Almighty, my Maker, who has helped me tremendously in all my academic endeavors.

I would like to express my deepest and most sincere gratitude to my advisor, Dr. Khalid Alshibli, for his supervision, advice, and guidance from the earliest stage of this research, as well providing extraordinary experiences throughout the work. With much pleasure, acknowledge his untiring help in providing valuable references and information, as well as financial support, without which this research could not have been completed. I would like to thank my thesis committee members, Dr. Clinton Wilson and Dr. Guoping Zhang, for the valuable discussions and support in my research. A special thanks goes to the entire Civil and Environmental Engineering Department of Louisiana State University for teaching me to move forward as an independent researcher. I also would like to express my deep thankfulness to my laboratory mates Mehmet Burak Cil, Yang Yi, and Zachary Autin for their companionship and support during this research work. A special thanks is also extended to Dr. Alsidqi Hasan for his previous laboratory work, together with the useful information given during this entire research. No acknowledgement is complete without mentioning the friends I made at LSU Hang Yin, Hao Ying, Tanvir Hossain, and Imtiaz Hossain.

I would like to thank Dr. Mark Rivers at Argonne National Laboratory for his advice, technical help, and useful information during the scanning period. I would also like to

acknowledge the visualization service center of LSU for providing me a remote license facility of AVIZO software.

Last, but certainly not least, heartfelt thanks must go to members of my family, who have all listened to my complaints and provided support in a variety of ways. Thank you for always being there for making my goals possible via positive expectations, patience, and love. You have all been part of the lighted torch that guided me along the way.

TABLES OF CONTENTS

LIST OF TABLES

Table Caption Page No

LIST OF FIGURES

Figure Caption Page No

ABSTRACT

Synchrotron Micro Tomography (SMT) is a powerful, non-destructive scanning technique for studying the internal structure of materials. SMT was utilized for two applications in this thesis. The first application involves tracking particle rotation of aluminum powder under different compaction strains. The experiments were conducted on two geometrical configurations by applying axial load to compact the powder in the die and acquiring SMT scans at different strain levels. The SMT scans were processed using AVIZO visualization software for further analyses. The analyses included tracking the same particle at different compaction strain levels, analyzing their volume compressibility, and then quantifying their rotational behavior with respect to the z-axis and xy plane. Particles were first tracked, colored, and then 3D volume was generated. The main findings of this analysis include: 1) the volumetric strain of the particles decreased at high compaction strain due to breakage of the particles into small fragments and elastic volumetric strain of aluminum powder; 2) initially, particles showed no rotation, followed by significant rotation, due to an increase of compaction strains; 3) the majority of the particles exhibited significant rotations near the loading plate and the curved boundary; 4) the 3D shape of the tracked particles under different compaction strains provided a significant contribution to the research area of powders by demonstrating that particles change their shape during the application of compaction.

SMT was utilized to quantify sand particles position during a Cone Penetration Test (CPT) as a second application. CPT is a fast and reliable in situ method for characterizing soil properties. A CPT was conducted on a sand specimen and the scans were acquired at different penetration depths using SMT. AVIZO was used to analyze the SMT scans with an objective of identifying how the particles change their position under different penetration depths. Individual particles were tracked and colored to perform this analysis. The results of

the analyses include: 1) most particles near the top of the specimen moved upward during initial penetration, due to a small overburden pressure; 2) particles belonging to the middle and bottom of the specimen showed a downward movement with CPT advancement; 3) the tracked particles provided an insight into particle interaction with advancing cone penetration.

CHAPTER ONE
INTRODUCTION

1.1 MOTIVATION

The application of external loads or compaction to granular materials causes a relative movement between the particles. Particle orientation and rotation during compaction has a profound influence on the stress-strain behavior. Very few studies were reported in literature quantified particle sliding and rotation, as a result of compaction strain increase. Researchers are often challenged with problems dealing with granular materials at different states of motion. The three distinct conditions of static, slowly deforming, and rapidly flowing are represented by typical examples in each regime, respectively: designing retaining structures, working with soil creep and settlement, and land slide prevention. Currently, extensive research is reported in the literature, predicting whether static, slowly deforming, or rapidly flowing behavior will govern the powder/soil behavior and how to determine the stress distribution within the soil/structure interface in each regime and, if in motion, the kinematics of the deforming field. It is not a simple task to identify the regime of granular material. Researchers successfully characterized the transition between static and moving granular materials by studying soil stability. However, the concept of the orientation of particles during flow is still not clear. Experimental 3D measurements of particle sliding and rotation during compaction of granular materials is an essential step for calibrating constitutive models dealing with the behavior of such materials.

Particle morphology significantly influences the constitutive behavior of granular materials and powders. Experiments are typically performed by using aluminum powder in order to simulate the behavior of granular materials. Powder represents a special sub-class of granular materials. Generally, powders that have fine grain sizes and a tendency to form

clumps are referred to as granular materials. It is defined as a dry-bulk solid, composed of a large number of very fine particles that flow freely when shaken or tilted.

The aluminum powder is produced by Aluminum Powder Metallurgy (PM). The mechanical properties of Aluminum PM are essential for many applications. Aluminum PM also offers an extensive economical advantage in the fabrication field when compared to other powder metallurgy products. Aluminum possesses engineering properties such as low density, high thermal conductivity, excellent finishing characteristics, and corrosion resistance that are not available in other PM materials. The process of producing aluminum PM consists of three different stages. Aluminum powders are mixed with alloying powder in controlled quantities during the first step. A lubricant is added for a consistent production of high density. The premix is then compacted in a specially designed PM press. Then the compact is immediately heated in a controlled environment furnace at a regulated temperature. This process bonds the particles together to develop the desired properties. The specimens prepared using such a process can be subjected to different non-destructive tests such as x-ray computed tomography (CT), impedance tomography, nanotomography, non-invasive 3D microscopy for evaluation, and characterization of their properties.

CT is an effective technology to investigate the internal structure of a specimen. It is a technique in which an object is placed between a detector and an x-ray source, and rotated continuously to acquire the internal information of the specimen. The information is reconstructed to generate a 2D slice to view the internal structure. The 2D slices are compiled together to build a 3D rendering (Cromwell, 1984). However, CT was used extensively in powder analysis. It was applied for studying row statistical density, column statistical density, and compaction responses, in order to understand density change in compacted powder. Alshibli et. al (2010) showed the density calibration of compacted powder analysis using

Synchrotron Microtomography (SMT). The results of this research might result in improving the current understanding about the rotational behavior of granular materials.

In addition to the application of CT for studying the behavior of granular materials, it was employed successfully to monitor the sand-cone interaction during Cone Penetration Test (CPT). CPT is one of a reliable and efficient method for stratigraphic profiling and obtaining soil-engineering parameters for geotechnical design. It has become widely accepted and encouraged by regulators as an effective environmental investigation method. Soil properties such as shear strength, permeability, in situ stresses, and compressibility can be computed with the help of CPT data (Alshibli et al., 2008). CPT is advantageous due to its fast data acquisition facilities, which provide a detailed subsurface information and option of immediate data availability. It can be applied for seismic-hazard mapping, paleoseismic exploration, ground-water-quality studies, regional or the site-specific three dimensional mapping of shallow sedimentary deposits. Moreover, it minimizes the retrieval of subsurface materials during exploration, an inconvenient and occasionally expensive byproduct of conventional drilling (USGS, 2005). However, at the present time no thorough studies have been attempted to explain the change in the properties of sand particles during the cone penetration test. This thesis will provide a key answer how the particles change their position during CPT.

1.2 OBJECTIVES

The main objective of the first part of the thesis is to develop a better quantitative understanding of the particles movement when compacted under different compaction strains and to analyze the rotational behavior of the particles. The objectives of the powder analysis are:

a) Develop 3D visualization images of the same particle under different compaction strain levels and provide a quantitative measurement of the location and shape of particles.

b) Quantify the volumetric strain of aluminum powder under different compactions strain levels.

c) Compare the rotational behavior of powder under different compaction strain levels.

The objective of the second part of this thesis is to provide a quantitative measurement of sand-cone interaction during CPT. The outcome of the analysis will provide key answers to the following question:

a) What is the amount of percentage change in the movement of particles in lateral and axial directions as the cone advanced further into the soil?

1.3 THESIS OUTLINE

The thesis contains seven chapters. The first chapter is an introduction to the thesis. Chapter two presents a literature review of x-ray computed tomography and brief introduction about powder flow. It includes the history of CT scans, generations of CT scanners, a description of the scanning process, and the working principle of synchrotron microtomography (SMT). The basic principles of powder flow and flow patterns are also presented in Chapter two.

Chapter three describes the experimental work with a description of the materials and apparatus, the procedure to conduct the scans at Argonne National Laboratory, the scanning process, and an image reconstruction. SMT scans analysis is presented in Chapter four, which includes the image processing and the compilation process to generate a full scan image. Chapter four also presents the analysis steps in AVIZO, such as tracking of particles, volume generation, and determination of angles.

The experiments were conducted to visualize the particles at different compaction strains. The image of those particles and the results of analysis are presented in Chapter five. A Cone Penetration Test (CPT) was conducted to quantify sand-cone interaction at different penetration depths. Chapter six describes the preparation of the specimen, the experimental procedure, and the results of that test. Chapter seven presents the conclusions, together with recommendations for future research on this particular topic.

CHAPTER TWO
LITERATURE REVIEW

2.1 INTRODUCTION

This chapter presents a literature review of the x-ray computed tomography and a brief introduction regarding the powder flow. It also includes history of CT scans, CT scanner generations, a description of the complete process of scanning, and the principles associated with the working of synchrotron microtomography. It presents fundamental principles of powder flow and its corresponding pattern. Finally, the chapter ends with a description of the process of powder compaction.

2.2 X-RAY COMPUTED TOMOGRAPHY (CT)

2.2.1 Historical Background of CT

X-ray computed tomography (CT) is used to acquire a three dimensional (3D) image of the scanned object. It is a powerful, nondestructive diagnostic technique with applications in the medical field and material science. Extensive research was conducted in the last two decades for industrial applications in order to analyze the internal structure and to identify the mechanical and physical properties of test specimen.

CT was introduced to characterize the internal structure of the scanned object in order to quantify rotation, size, shape, and volumetric change, as a nondestructive technique to generate 2D cross-sectional images of an object, using x-ray images. CT is also known as computer axial tomography scanning (CAT). The word “tomography” is composed of two Greek words ‘tomos’ and ‘graphia’. ‘Tomos’ means slice or section, whereas ‘graphia’ means describing.

The development of CT is proven to be one of the best inventions, after the discovery of x-rays, in the field of radiology. Nowadays, CT scan is widely used for better visualization of a wide range of engineering materials that cannot be visualized using other techniques. It became a paramount source of successful innovation after the introduction of spiral CT in the 1890. The history of CT scanning dates back to the late 19th century, when the eminent physicist Wilhelm Contrad Roetgen first discovered x-ray radiation in November of 1895. The first silver bromide coated photographic x-ray plate was developed in Frankfort in 1896 followed by a collimator to suppress scattered radiation, introduced by Pasche in 1903. A significant development in CT technology occurred in 1913. In order to improve image quality, scattered radiation was removed before it striked the x-ray film. Bucky (1913) developed the scattered radiation grid in Berlin, while the first high vacuum hot-cathode tube was built by Willam Coolidge in Massachusetts, USA in the same year. Before 1930, there was a probability of losing relevant structural information due to the practice of super imposing a 2D display of a 3D object. However, Bernard Ziedses des Plantes developed planography in order to produce perfect geometrical images in 1930-31. This further refined the tomographic technique. In 1930-31, Allesandro Valleborn also developed stratigraphy which later led to the development of tomography. Godfrey N. Hounsfield made a historical contribution in the field of CT in 1972. His contribution allowed the production of non-superimposed images for the first time. From 1978 to 1990, there was a tremendous growth in the scanning system throughout scientific discovery. The invention of ECG-synchronized CT images, integrated gantry cooling, and heat exchangers were among these findings. Following the development of the first spiral CT scanner in 1989, used for continuous volume measurement, there was a remarkable development in the field of medicine with the medical CT scanning system. Some of these advancements included the use of an ultra fast ceramic detector (UFC), a real time image display, a volume rendering technique (VRT), a

reconstruction algorithm for multiple slices spiral scanning, multiple slice scanning with 16 slices per rotation, and an isotropic resolution of up to 0.6 mm. At present, CT is extremely efficient in acquiring 2D and 3D renderings of scanned materials. Figure 2.1 represents a timeline in the key development of CT scanners (http://www.medical.siemens.com/siemens).

Different types of scanners are used in various fields of industry, based on the size of the object and purpose. Typical industrial CT systems include ImagiX, X-View, Coordinate x-ray Measurement Machine (CXMM), and Inline. ImagiX tomography is used to scan small objects varying in size from 0.02 to 6 inches. It is convenient to properly size an x-ray source, as well as the detector, with the aid of x-view CT systems. CXMM has been applied mainly for 3D computational purposes. It is useful in providing internal and external dimensions for any part with very high resolution. Automatic and fast CT inspection and 3D modeling of an object are necessary to perform; therefore, an in-line CT system has been employed successfully to fulfill this purpose (http://www.xviewct.com/).

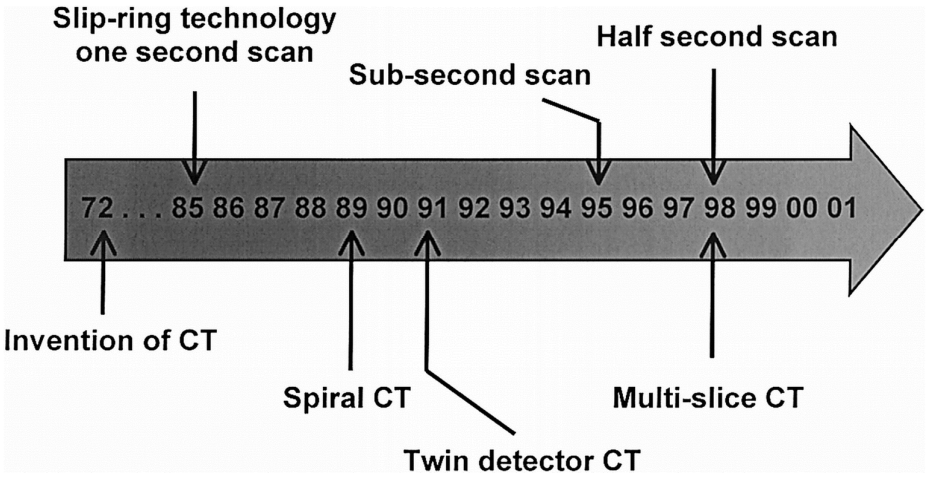

Figure 2.1 Timeline of the key technological development in CT (Mahesh, 2002).

One of the primary reasons for using CT in industrial applications is mainly due to its non-destructive nature that permits visualization of the internal structure of an object. Moreover, it is convenient to validate the design requirements for both internal and external components, as well as inspection and analysis costs from the first stage to production stages. The inspection quality is also better, since it contains much more information than single x-ray facilities. Internal dimensions may be measured only with the aid of CT. As a result, CT has been used for various purposes, such as an analysis for material structure, NDT inspection, surface rendering, rapid prototyping, density analysis, measurements, meteorology, 3D digitalization, and reverse engineering.

Rapid prototyping is another industrial application of CT. It is a manufacturing process that produces objects directly by the computer-aided design (CAD). Stereo lithography is one of the techniques that directly produces a 3D representative by assembling the 2D images which are acquired from CT scans. The data used in a stereo lithography system are chosen, based on rapid tooling techniques with applications to specific areas (Hughes et al., 2000).

CT assisted reverse engineering methods are successful in enabling older designs without CAD files to access the many available rapid tooling techniques currently available, in contrast to rapid prototyping. Reverse engineering is a technique typically used to discover the technical principles of a device by analyzing its structure, function, and operation. The 2D images in reverse prototyping may also be assembled to produce 3D representation, such as rapid prototyping. The CT data of reverse engineering not only provides surface information, but also accurate measurements of all internal structures, without the use of special programming. CT images can be generated for any object, regardless of the complexity of structure (Hughes et al., 2000).

Metrology is another field where CT has significantly implemented like reverse engineering. The main purpose is to evaluate the physical measurements. Reverse

engineering is one of the techniques used to perform this task. A huge number of points which resemble the surface of the part are collected to compose a surface cloud, and then registered in the computer to generate design files. A statistical deviation is made between the inspection and computer-aided design data; thus a tolerance is created, depending on allowable factors (Hughes et al., 2000).

2.2.2 Generation of CT Scanners

CT scanners are typically classified, based on the mechanical equipment configuration which correlates a corresponding motion between the specimen, the detectors, and the source. All CT machines have the same principles; however, their scanners vary depending on the configuration of the components.

2.2.2.1 First Generation Scanner

First generation scanners used a single x–ray detector and a thin slit x–ray beam to acquire the entire CT image. A C-arm frame consists of an x-ray head and a detector that can be rotated through an arc of 180 degrees (Figure 2.2). However, sometimes the scanners have two x-ray beams. Therefore, a second detector makes it possible to acquire two full section scans simultaneously. The x-ray head and the detector were set on a synchronized linear scan system. The linear scanning system moved a narrow slit x-ray beam across an anatomical view to produce one view or x-ray image, while the C-arm continued to rotate in the same position. The C-arm could be placed in 10 steps for organizing 180 linear scans along the 180 degree arc. This system would allow 240 detector measurements at 1.7 mm intervals to produce each of the 180 scans. It took approximately 10 minutes to complete the CT scans and the process of image reconstruction (Carlton and Adler, 2006).

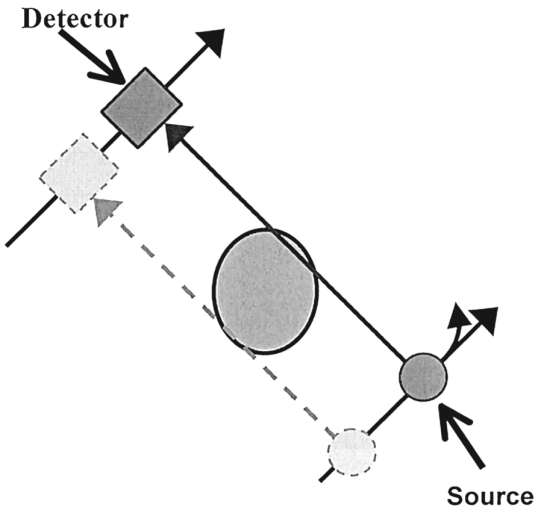

Figure 2.2 First generation CT scanner (Mahesh, 2002).

2.2.2.2 Second Generation Scanner

The second generation CT systems used the same rotation scan geometry as the first generation system (Figure 2.3). The main objective of increasing the number of detectors was that it reduced the number of linear scans. The C-arm frame contained an x-ray head and detectors, similar to the first generation scanner. The time required for scanning was reduced significantly in the second generation scanning. However, a scattered radiation artifact was introduced, due to use of fan-shaped beam (Carlton and Adler, 2006).

2.2.2.3 Third Generation Scanner

The third generation scanner is the first scanner to rotate an image 360 degrees (Figure 2.4). As a result, the need for a linear scanning system was eliminated. It became possible to acquire approximately 700,000 measurements per anatomical section in third generation scanners. The scanners were able to capture the image of the entire specimen in a single exposure by utilizing an entire beam and a large detector which contained a wider, fan-shaped x-ray beam and an array of 250-750 detectors. The scanning time was faster in the

third generation scanner than in the second generation scanner and approximately four scans could be done per minute. The scan arcs of 360 degrees were possible in the third generation scanner, in lieu of 180 degree scans of the second generation scan; the scan arc will vary (Carlton and Adler, 2006).

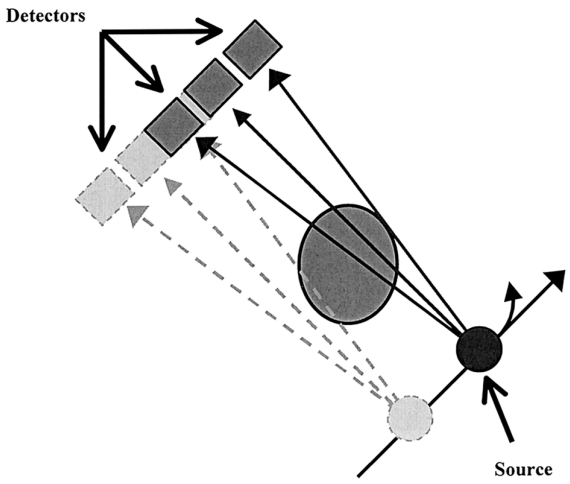

Figure 2.3 Second generation CT scanner (Mahesh, 2002).

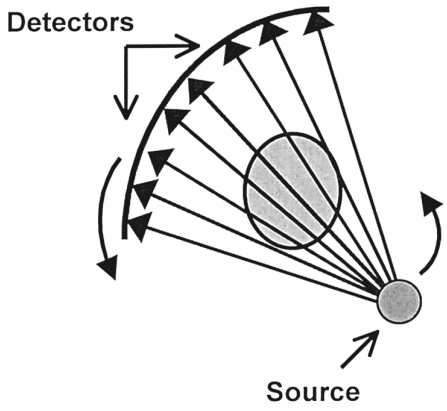

Figure 2.4 Third generation CT scanner (Mahesh, 2002).

2.2.2.4 Fourth Generation Scanner

The fourth generation scanning system can rotate an image 360 degree, much like the third generation scanning system (Figure 2.5). However, they used a stationary circular array of detectors which allowed only the source to move. The detectors made a circle around the test specimen. The fan beam rotated around the test article and illuminated the test specimen. As a result, a view was acquiring successive absorption measurements of a single detector at successive positions of an x-ray source. Fourth generation scanners were more complex and costly, compared to previous ones, since they combined an artifact resistance of the second generation scanner with the speed of the third generation scanning system. It was also more susceptible to scattered radiation (Hughes et al., 2000).

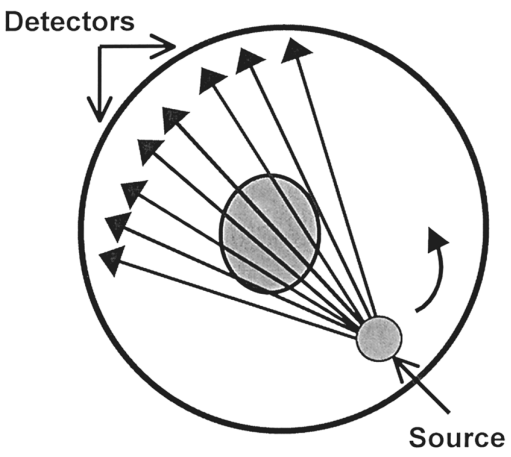

Figure 2.5 Fourth generation CT scanner (Mahesh, 2002).

2.2.2.5 Fifth Generation Scanner

Fifth generation scanning was suitable for precise imaging of a rapidly moving object, which was different from the previous systems in that there was no mechanical motion

involved. A circular array of x-ray sources were used in this scanner system, which could be electronically switched on and off. When an x-ray source was powered on, the scanner used a circular array of x-ray sources, which were projected onto a curved fluorescent screen for attaining a large quantity of an image simultaneously. Such method of data collection was essentially different from the previous four, since a series of 2D projections of a 3D object was acquired rather than a series of 1D projections of a 2D object (Hughes et al., 2000).

2.2.2.6 Sixth Generation Scanner

Sixth generation CT scanners are normally known as Helical CT scanners (Figure 2.6). Slip-ring technology was developed in this system, and it allowed gantry to rotate continuously without wires. It was a new scanning technique in which data were continuously acquired, while the table was transported through the gantry. Along with the development of this technique, a larger anatomic extent in the direction of table transport was imaged in a shorter time, compared to previous conventional scanners. The use of helical CT scanners either eliminated or limited wrong respiratory registration artificats; therefore, an image display in multiple places became more realistic (Ibukuro et al., 1994).

2.2.2.7 Seventh Generation Scanner

The seventh generation scanner is known as a multiple detector array system (Figure 2.7), that overcame the x-ray tube output limitation. The collimator space is wider in this system, and the x-rays generated by the tube are used to produce image data. The detector size determines the slice thickness, due to the advantages of multiple detectors, rather than a collimator. The benefits of a multi array scanner system over a helical system are significant. These advantages include an improved temporal resolution, an increased concentration of intravascular contrast material, a decreased image noise, an efficient x-ray tube. It also

includes isotropic viewing with the help of multi-planar reformation in spatial situations (Rydberg et al., 2000).

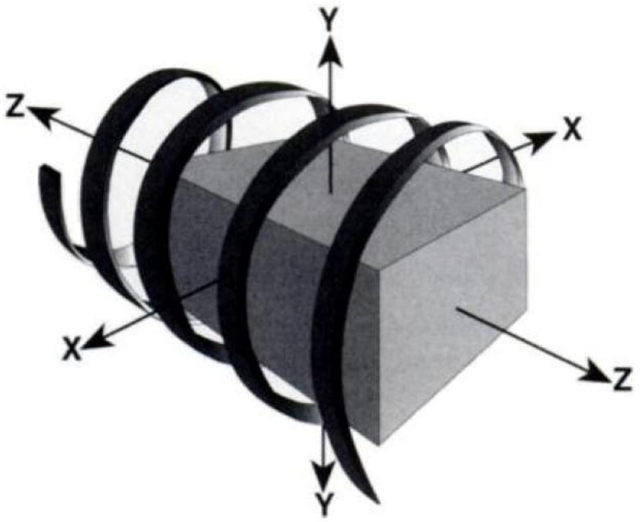

Figure 2.6 Sixth generation CT scanner or Helical scanner (Ibukuro et al., 1994).

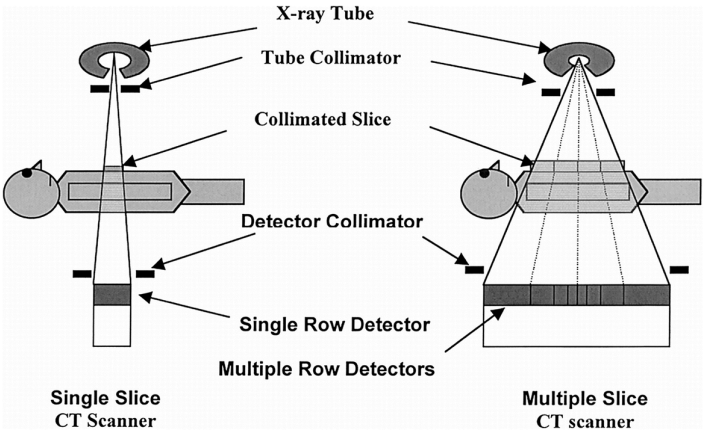

Figure 2.7 Seventh generation CT scanner (Mahesh, 2002).

2.2.3 Principle of CT System

The CT system is composed of a rotating stage, a radiation source, and an imaging system (Figure 2.8). A computer is connected to a rotating stage and the imaging system such that x-ray images are collected and correlated to the position of the test component. The CT system collects the image of the test specimen when the specimen volume is projected onto the detector. The attenuation of the material depends on its density, composition elements, and x-ray energy. The specimen is again rotated to collect the data for the next projection. The imaging system produces a 2D dimensional shadowgraph image of the object, much like a film radiograph. These scans are then processed with a computer-aided program, and subsequently stacked together to develop a 3D image of the specimen.

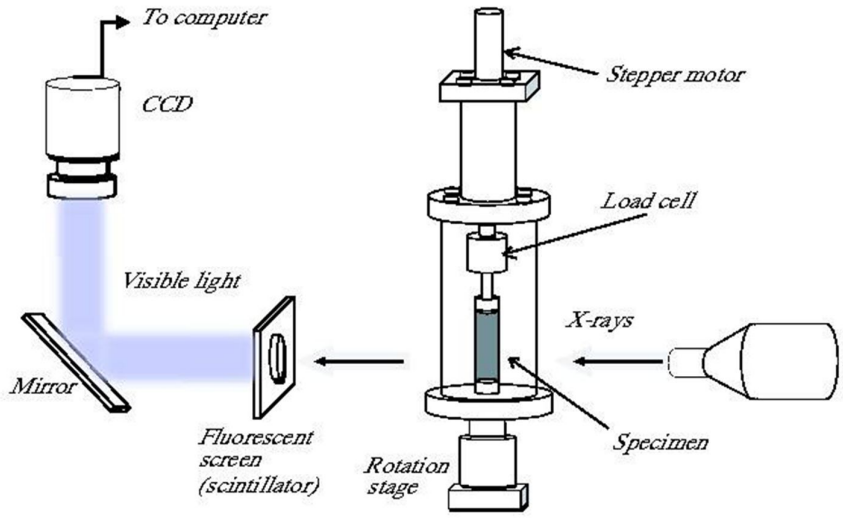

Figure 2.8 Schematic diagram of Synchrotron Computed Tomography (Hasan, 2009).

2.2.4 Synchrotron X-ray Tomography

Synchrotron x-ray tomography is a technique visualizes the 3D interior structure of real objects nondestructively and with a high spatial resolution. The detailed microstructural analysis of different kinds of materials can be analyzed with the aid of this tomographic system. The extremely high intensity of the original source, provides images with a high signal to noise ratio on short time scales, which ultimately enables a quick radiographic system. The option of varying radiation energy enables the investigation of objects with different absorption coefficients within the same measuring environment. The implementation of high beam coherence for phase contrast imaging provides a much higher image contrast, when compared to other tomographic systems. Figure 2.9 shows the synchrotron CT facility of Agonne National Laboratory.

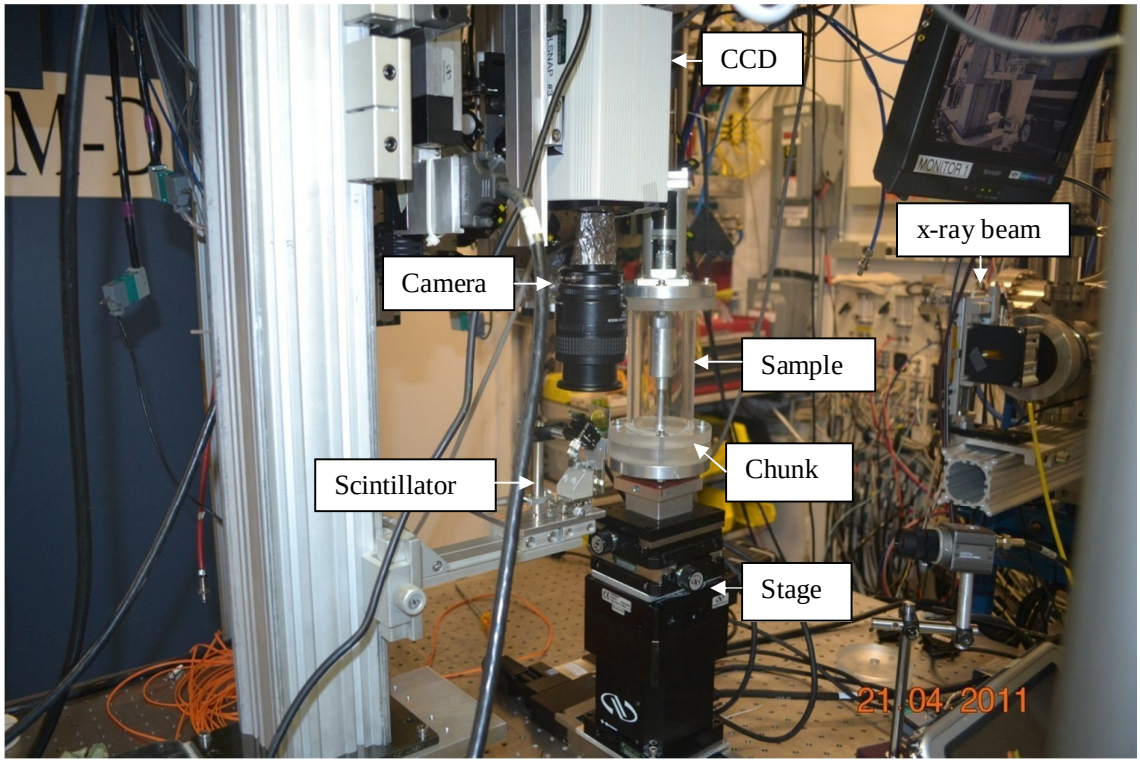

Figure 2.9 Schematic diagram of the CT system at Argonne National Lab.

2.3 POWDER FLOW

The elements of powder mechanics have long been known and widely investigated in extant literature. First, Hagen reported on the flow of sand in 1852, and Reynolds observed dilatancy during the deformation of a mass of sand in 1885. However, the principal equations of powder mechanics are identical to soil mechanics. These are based on the preliminary works of Coulomb (1776) and Rankine (1857) on the frictional behavior of a mass of sand. Dawes (1952) and Jenike et al. (1960) made excellent advances in this direction. Jenike (1961) and Richmond and Gardner (1962) defined the boundary condition of powder mechanics. The equation of motion was investigated by Geniev (1958) and Brown (1961), who proposed an energy theorem for freely flowing granules. Athey et al. (1966) investigated the flow patterns of powder by x-ray and effects of particle size, with powder strengths investigated by Farley et al. in 1968.

Over the last 50 years, many experiments and studies were conducted to characterize the flow and patterns of powders and to calculate the rates of discharge. Presently, powder mechanics is developing rapidly, allowing an expectation that theoretical and experimental connections will be established between stress distribution and flow patterns. However, more research is needed to identify the factors that affect the packing and flow of powders. Discharging the powder though bin outlets, flow through hoppers and filling, as well as compacting the die cavities, will require information about the flow patterns, strength of powders, and their adhesion to surfaces.

2.3.1 Basic Principles of Powder Flow

Powder behavior is mainly governed by three principles during flow; they are the principle of dilatancy, the principle of mobilization of friction, and the principle of minimum energy of flowing granules. Reynolds (1885) observed that a “tightly packed mass of

granules enclosed within a flexible envelope invariably increases in volume when the envelope is deformed: if the envelope is inextensible but not inflexible, no deformation is possible until the applied forces rupture the bag or fracture the granules." Fundamentals of dilatancy was expressed by this quotation**.** The simple conclusion about dilatancy was presented by Jenkin (1931), stated as "shearing causes some granules, previously in contact, to separate so that the contacts become 'slack': surfaces of sliding, permitting relative displacements of granules, are thereby formed" (Brown and Richards, 1970).

The second principle is known as the principle of mobilization of friction. The frictional force between any two granules in a powder at rest can occupy any value between zero and a limiting value, where the limiting value depends on the normal force between the granules. It states that the stress distribution in a powder at rest is indeterminate. However, a surface of sliding is formed when the frictional force reaches its limiting value, due to the shearing of powder.

As the powder starts to move from its rest condition, the granules are slowly rearranged. The steady flow of powder suggests that the state of the powder in motion can be determinate. In such a case, the energy is minimized, due to a restriction on the generality of the principle of mobilization of friction, known as the principle of minimum energy of flowing granules (Brown and Richards, 1970).

2.3.2 Factors Influencing Powder Flowability

It is difficult to predict the flowability of the powder, due to a large number of influencing factors, which control the rheological properties. The physical variables include particle size, shape, size distribution, particle interaction, hardness, strength, stiffness, and fracture roughness, whereas flow rate, compaction condition, vibration, and humidity act as external factors to control the properties of powder flow. Powder flow depends mainly on

particle size, variation of size, and the shape of the particles. Generally, powders with large particles (>100 μm) are considered to be non-cohesive, permeable, have low compressibility, and possess relatively low shear strength, whereas fine powder (<10 μm) is considered to be cohesive, compressible, and with a high shear strength.

The flowability of powder depends on an adhesive force between the individual particles, as well. Adhesive forces are created due to a different mechanism. Van der Waals interaction results adhesive force in fine grained dry bulk powder, in opposite, for moist bulk powder liquid bridges between particles are most important. However, both of these adhesive forces are dependent on the distance between particles. It is found that the influence of adhesive forces increases with a decreasing particle size; as a result, a bulk solid flows poorly with a decreasing particle size. The compressive force acting between the particles may be increased if the particles are pressed by external forces. This leads to plastic deformation of the particles in the contact area, which results in an increase of the contact area. As a result, an adhesive force increases in compact. The adhesive forces may then be increased, due to an application of compressive force from the outside (Schulze, 2006).

2.3.3 Types of Flow

Powder flow has been extensively studied due to its technological importance and granular material handling industries. In general, the flow pattern depends on the die geometry, and the friction between the particles and die, as well as material internal friction. It normally classified into two categories-mass flow and core flow. In mass flow, the entire contents are in motion and normally there is no dormant zone (Figure 2.10). As a result, the risk of product degradation is reduced. However, the stresses are usually constant throughout the die, giving a low powder compaction of the powder. The quality of the bulk solids normally remains constant, following a “first in-first out” flow pattern, whereas a core flow maintains “last in-first out” flow pattern which means the bulk solid last filled is extracted

first. Generally, core flow is characterized by a powder discharge through a preferential flow channel from the top free surface of the die. Sometimes it induces a poor bulk solid quality. There is the possibility of a reduction in the active volume region, due to the uncertainty in the hardening of stagnant zones. However, mass flow is advantageous over core flow since, a segregation of particles according to size is far less of a problem in mass flow.

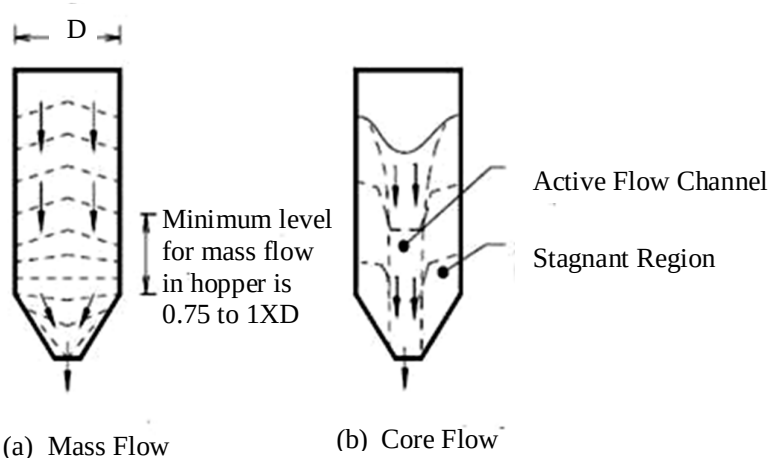

Figure 2.10 Schematic diagram of Mass flow and Core flow (Modern tools for hopper design, 2009).

2.3.4 Flow Patterns

During the flow, the powder often changes velocity in a rapid scale over a small region. There seems to be no specific reason behind this behavior. Literature suggests that there may be thin regions of dilated material across which the powder flow continuously changes. Thin regions as a surface where the stresses, velocities, and some of their derivatives with displacement are discontinuous is known as a “surface of sliding” or shear band. The shape of the surface of sliding depends on both stress distribution and yield location. Resources are

scant to identify this type of relation without the knowledge of free-fall arch and the principle of minimum energy. The free fall arch refers to the surface below which the powder can fall freely, and there are no constraints. At the free fall arch, the energy is the sum of kinematic and potential energies and assumed to be a minimum. These two factors determine the flow of powder and conclude that the fluid phase has no impact on the flow of powders.

2.4 POWDER COMPACTION

Powder compaction is a complex engineering process. It is a process which includes filling a die with powder, then compressing the powder by using rigid punches to produce a dense compact and ejection of die (Sinka, 2007). Die compaction, pellitization, and slugging are used to improve the flow characteristics or to produce a uniform compact. Post-compaction operations like sintering, sizing, and coating are usually applied depending on the application. Die compaction is effectively employed in powder metallurgy, pharmaceuticals, ceramics, and other industrial sectors.

Die compaction is regarded as the most widely used, conventional technique. This includes rigid dies and special mechanical presses. It is utilized to consolidate the powder into a desired shape, to acquire a desired level and type of porosity, and to gain sufficient strength of the powder for subsequent handling.

2.4.1 Compaction Technique and Machinery

The compaction technique may be classified by referring to the movement of the individual tool parts as an upper punch, lower punch and die compaction in single action and double action. The lower punch and the die remain stationary in a single action. The entire action is mainly carries out by an upper punch, which moves slowly to the fixed die. Since only the top part of the die becomes compacted, the specimen that rests on top of the die has the greater density. In a double action, high density exists in both the top and underside of the

die, as the upper and lower punch operate simultaneously. However, there remains a “neutral zone” which is preferred as weak, in between the highly density zone. Compaction machinery can be classified into two categories-single action and rotary presses to perform these actions. The single action press is mainly used for those components in which manufacturing takes place on a larger scale, the tools have a complex geometry, and the task requires high compressive force. In contrast, rotary presses used for smaller parts as well, have a relatively simple geometry.

2.4.2 Compaction Process

A compaction process essentially involves three basic steps: the application of stress to the powder, the removal of that stress, and the ejection of the compact. Initially, the particles rearrange themselves to produce a higher density when the stress is applied. This results in the powder behavior transferring from an elastic to a plastic deformation. The powder flows smoothly within the compact due to the application of stress and an increase in bulk density. The strength of the compact depends on an applied maximum solids pressure, which is equal to applied total pressure, minus an interstitial air pressure. The total pressure developed within the compact is a function of the initial pressure, the compressibility of the powder, and the geometry of the die. However, application of a higher total pressure does not mean that a result of entrained air due to interstitial air pressure can be neglected. The compact might fail shortly after the removal of the applied load if the interstitial air pressure is higher than the applied pressure. The permeability of the compact can be used to measure the ability of the entrained air to escape after the removal of the load. The last two steps of compaction include elastic recovery, air expansion, escape flow development, and possible fracture initiation, such as capping and lamination (Prescott et al., 2000).

The compact may fail due to several factors, such as elastic recovery or air entrainment in the powder. The elastic recovery introduces stresses that contribute to a

potential failure of the compact. Moreover, when compression is applied to the die, air flows upward, against the downward flow of powder; this process would eventually retard the flow of the powder. Finally, the acceptable rate of the compaction mainly depends on the permeability of the powder. Methods that accelerate the rate of compaction can be employed to improve the rate of compaction (Miller, Handbook of Granulation Technology).

CHAPTER THREE
COMPACTION OF ALUMINUM POWDER

3.1 INTRODUCTION

This chapter mainly provides an overview of the materials that were used in the experiments, describes the apparatus, and explains the experimental process. The preparation of the specimens, the compaction procedure, and the procedure for analyzing the scans is also described in detail.

3.2 EXPERIMENT MATERIAL

Aluminum powder AMB-2712 (Al-3.8, Cu-1, Mg-0.7, Si-0.1, Sn-1.5% Acrawax) was used in the experiments. It is manufactured by U.S. Ampal Inc., Flemington, NJ. The SEM image of AMB 2712 used in the experiments is shown in Figure 3.1, and Table 3.1 lists the vendor, composition, mesh size, and density of the powder.

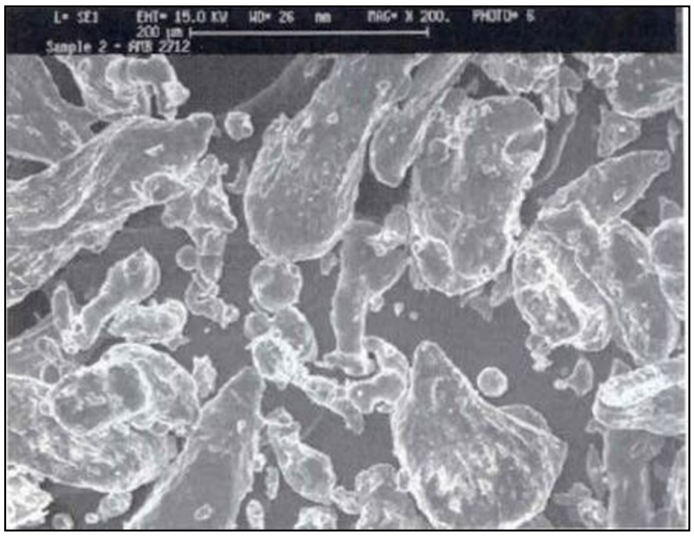

Figure 3.1 SEM image of ampalloy AMB 2712 aluminum alloy powder.

3.3 DIE GEOMETRY

Two different compaction die configurations were used in the compaction experiments. Compaction configuration I has an upper punch, a lower punch, a die, and a spacer, whereas configuration II is composed of an upper punch, a lower punch, two dies, and a spacer. The schematics of the two configurations are illustrated in Figure 3.2. The die used in this compaction experiment is made of aluminum. The punch is made of steel and can apply a high axial pressure on the powder without risking breakage. The purpose of the spacer was to keep the punch by accurate application of pressure in the axial direction without eccentricity. The geometry of all compaction tool sets is depicted in Figures 3.3 through 3.8, and the compaction process for both configurations is shown in Figures 3.9 through 3.13.

Table 3.1 Specification of the Aluminum powder.

Vendor	Ampal
Powder	AMB2712
Composition	Al-3.8, Cu-1, Mg-0.7, Si-0.1, Sn-1.5%
Mesh	-100/+325
Pycnometer Density (g/cm^3)	2.7146
Apparent Density (g/cm^3)	1.22
Tap Density	1.51
Grain Size	93±7 μm
Fatigue Endurance Strength	145 MPa

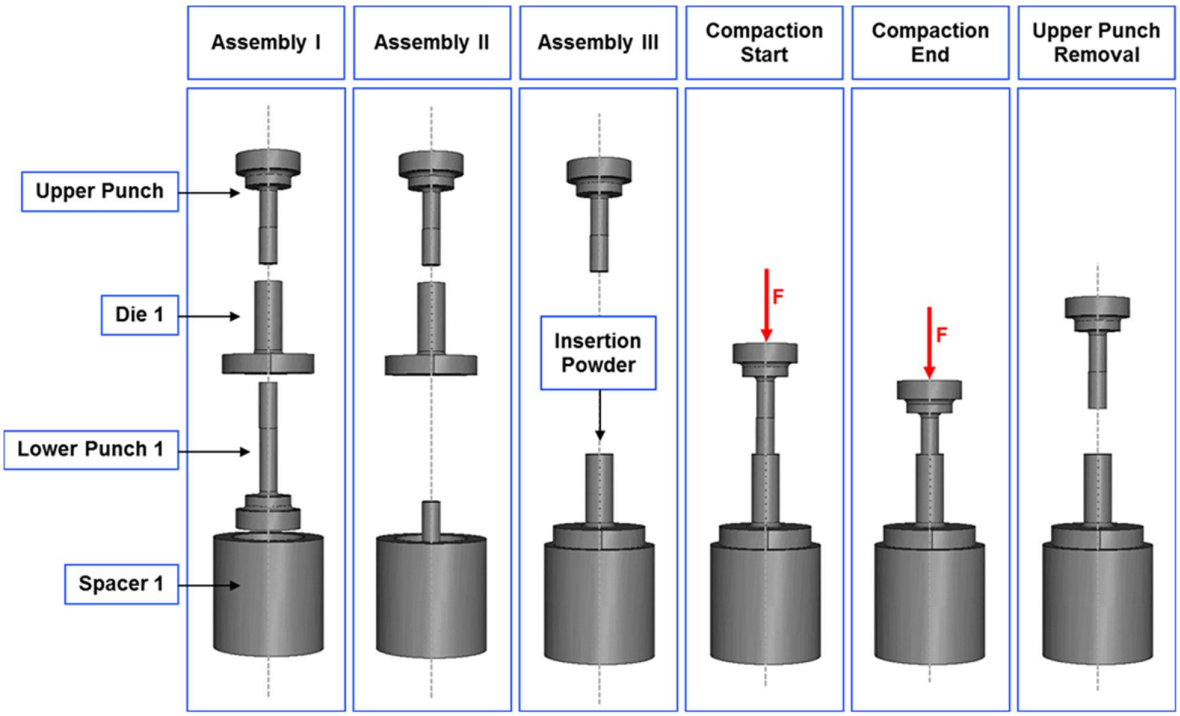

Figure 3.2 Assembly and compaction process for configuration I.

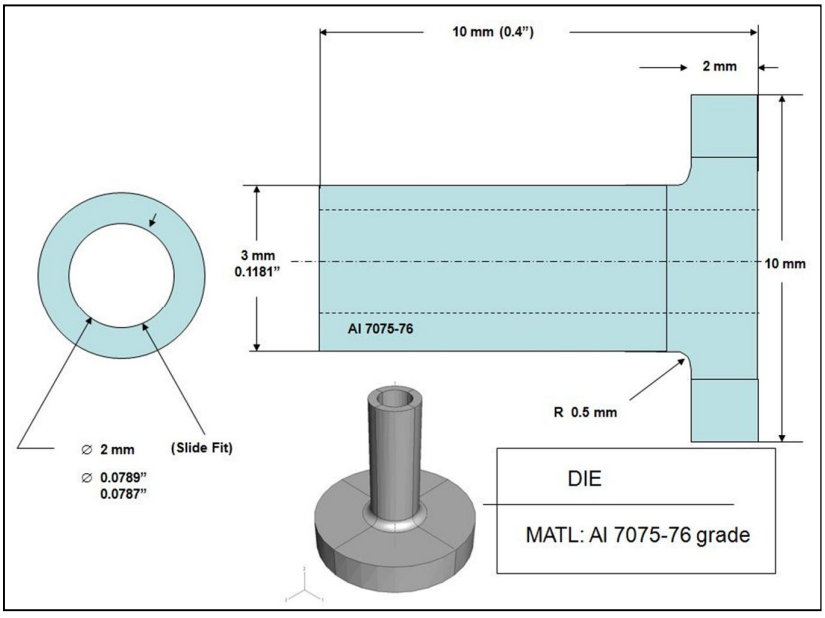

Figure 3.3 Details of the die.

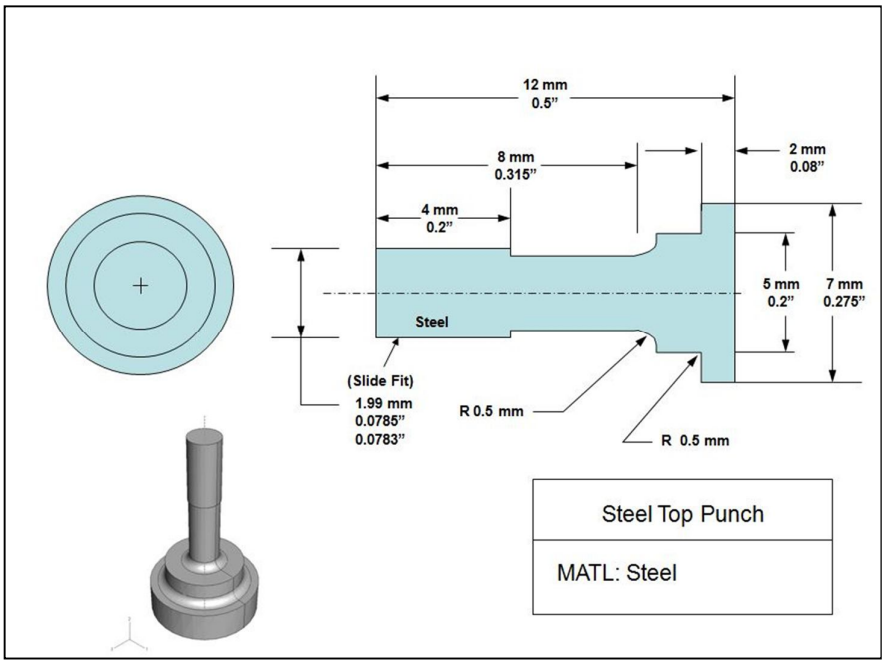

Figure 3.4 Details of steel top punch.

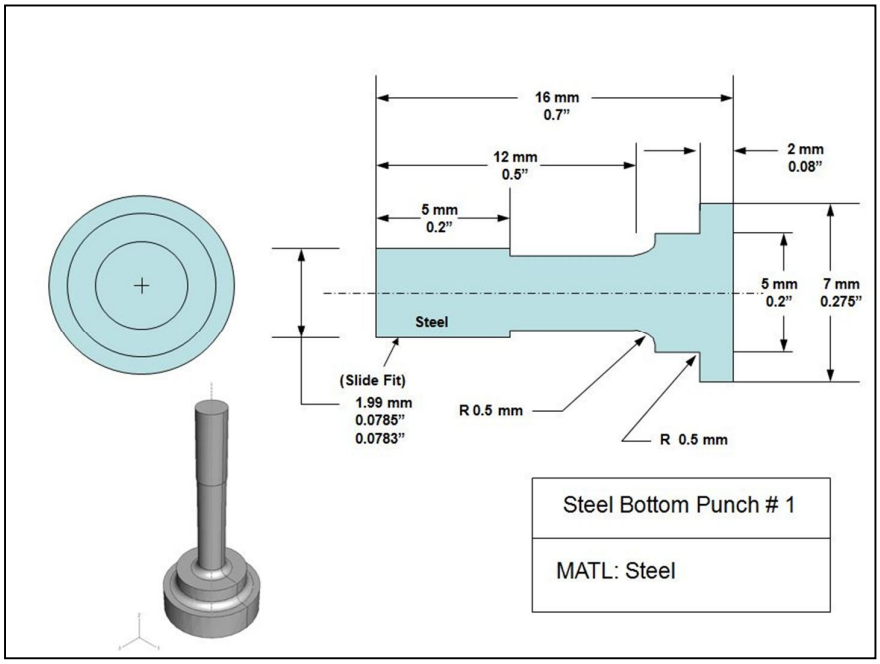

Figure 3.5 Details of steel bottom punch #1.

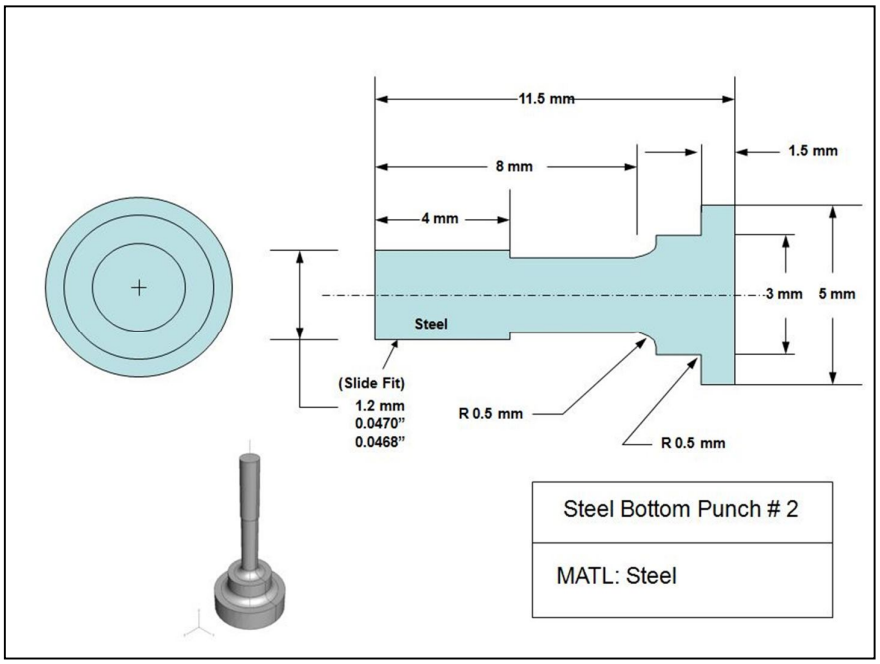

Figure 3.6 Details of steel bottom punch #2.

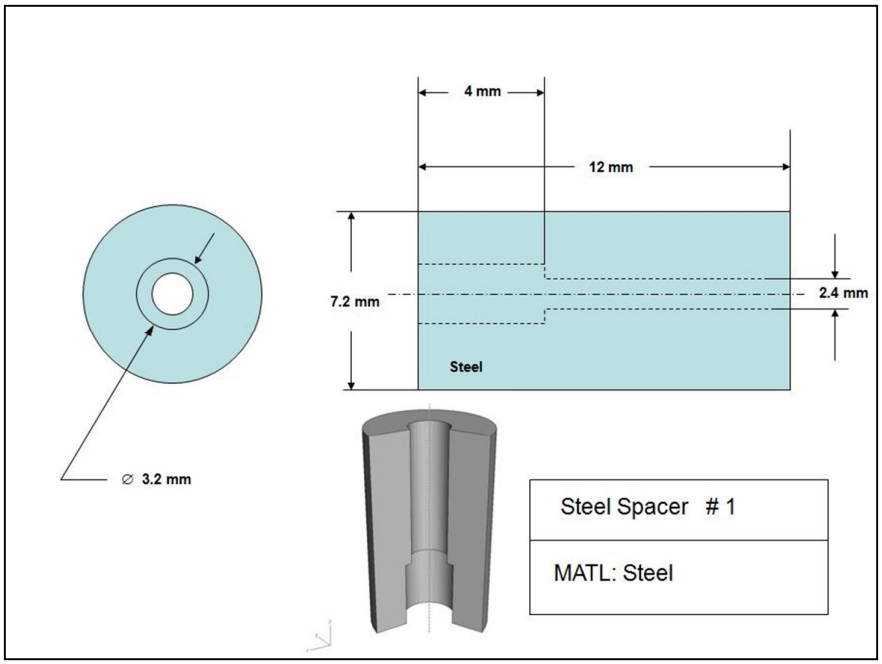

Figure 3.7 Details of steel spacer #1.

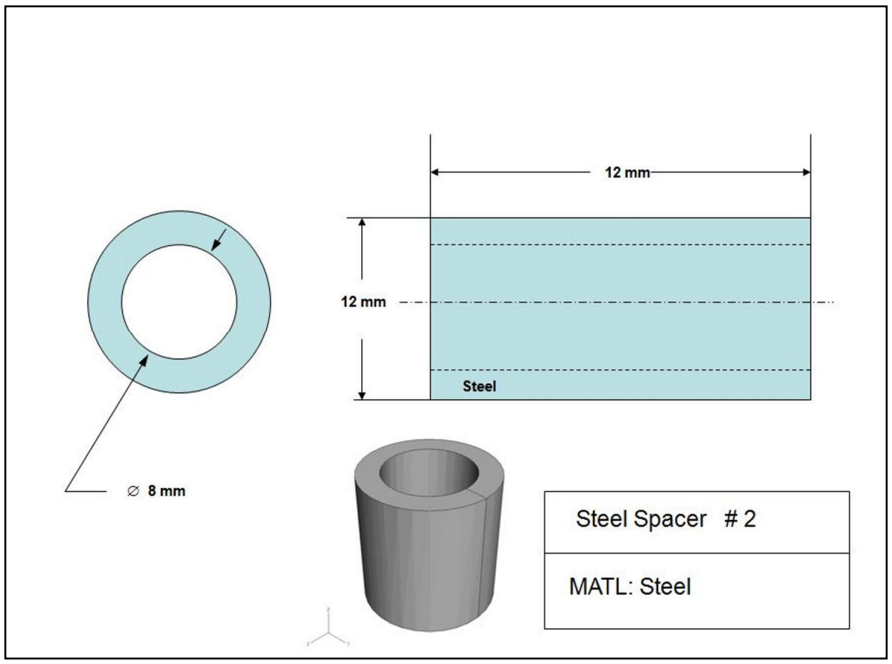

Figure 3.8 Details of steel spacer #2.

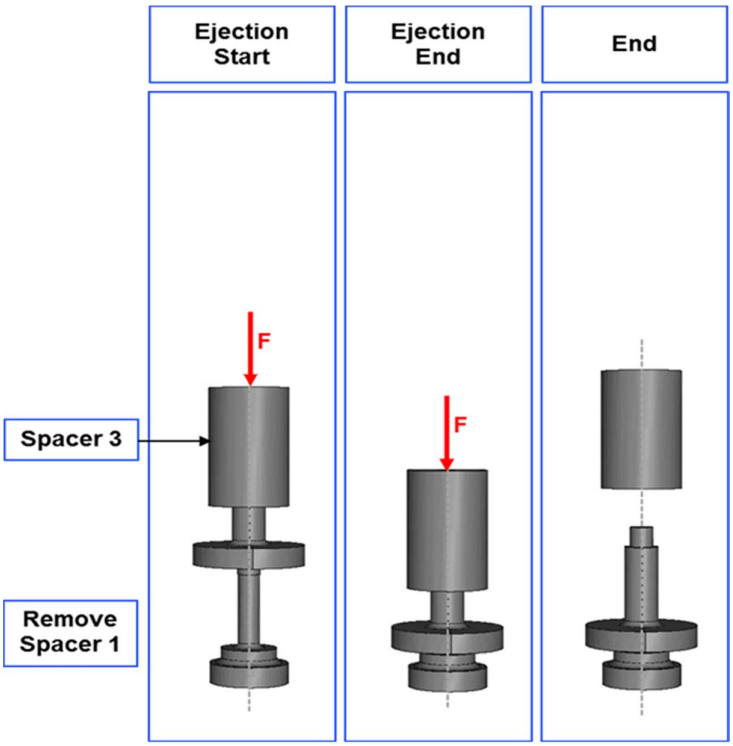

Figure 3.9 Ejection process for configuration I.

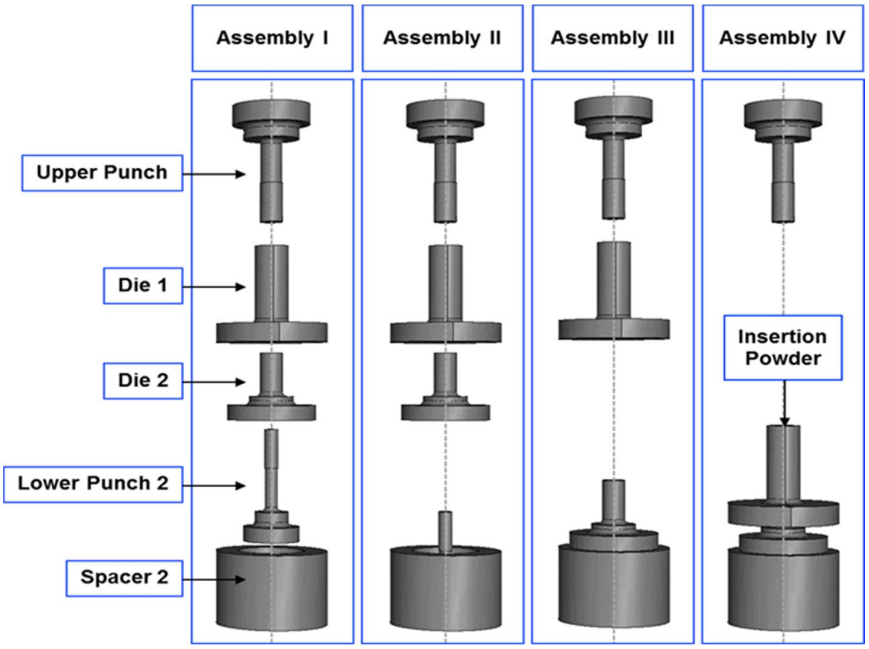

Figure 3.10 Assembly process for configuration II.

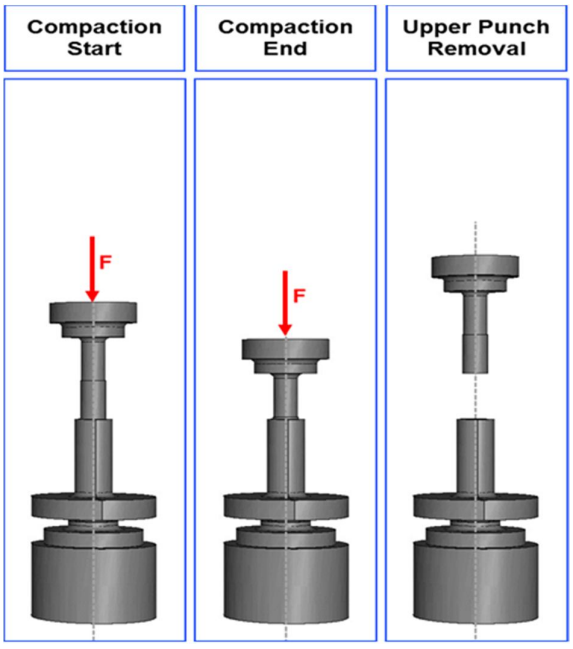

Figure 3.11 Compaction process for configuration II.

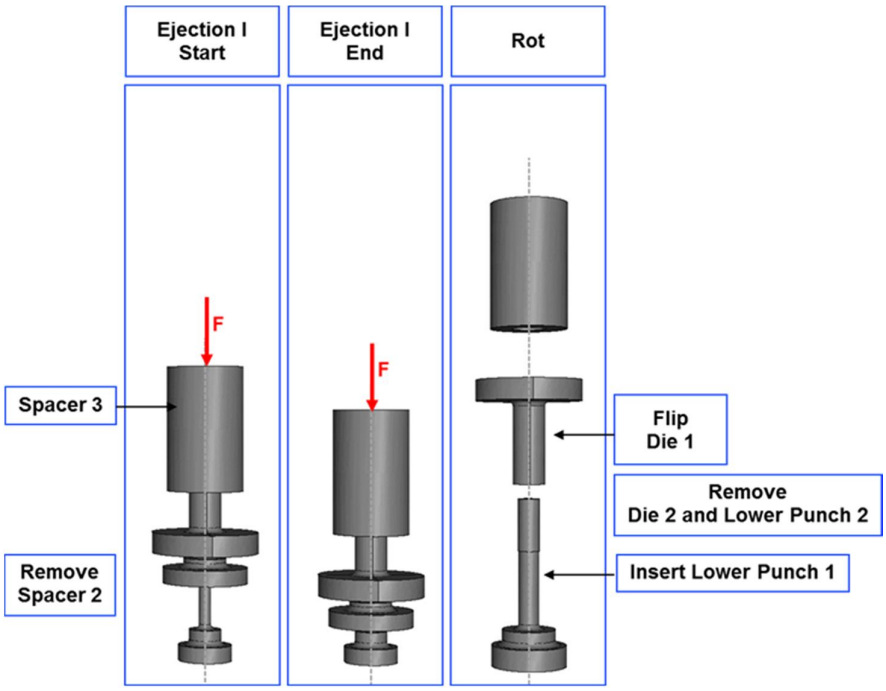

Figure 3.12 Ejection process I for configuration II.

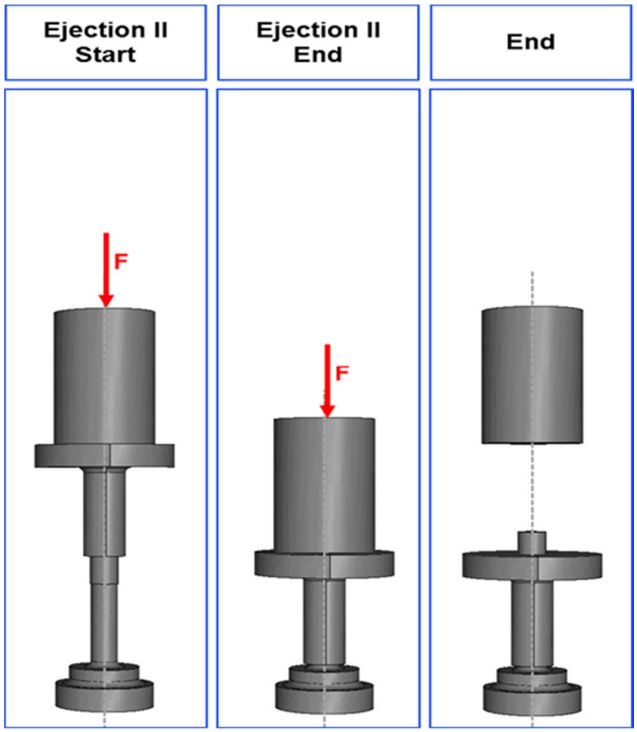

Figure 3.13 Ejection process II for configuration II.

3.4 EXPERIMENTAL PROCEDURE

On March 29, 2008, the scans were acquired using Beam 13 of the Advanced Photon Source (APS) of the Illinois Argonne National Laboratory. The CT scans were conducted on two die configurations. The die was first filled with the powder, using a funnel to avoid contact with the wall and to attain uniformity. The dies were especially fabricated to carry out the experiment. The specimen was required to be small enough to obtain a high resolution in the CT scans. To acquire the scans, the die of the test specimen should be made of a low atomic number, in order to permit passage of an x-ray. Figure 3.14 shows a photo of the compaction experiment on the stage of CT scanner. A computerized loading frame was used for application of the load at an axial strain rate of 1%/min. Finally, it was scanned, and a data acquisition system was used to acquire the load from the load cell.

3.4.1 Scanning Process

The specimen was clamped to the stage of the scanned load (Figure 3.14). The source was emitting an x-ray beam using a 27 kev of energy. The specimen was rotated at 0.5 degree increments in a process to collect attenuated x-ray. The scintillator converted the attenuated x-ray into a visible light, which was then recorded after reflection through a mirror, using a CCD camera.

Configuration I has a uniform diameter, whereas the diameter is not constant in configuration II (Figure 3.15). Both specimens were compressed at a constant strain rate up to 50% and 12% maximum strains in configurations I and II, respectively. The stress-strain behavior for both configurations is depicted in Figures 3.16 and 3.17, respectively. A total of 11 scans were acquired for configuration I at 5% strain increments. Scans for configuration II were acquired at 3% strain increments, up to 12%. The initial conditions of both configurations are summarized in Table 3.2.

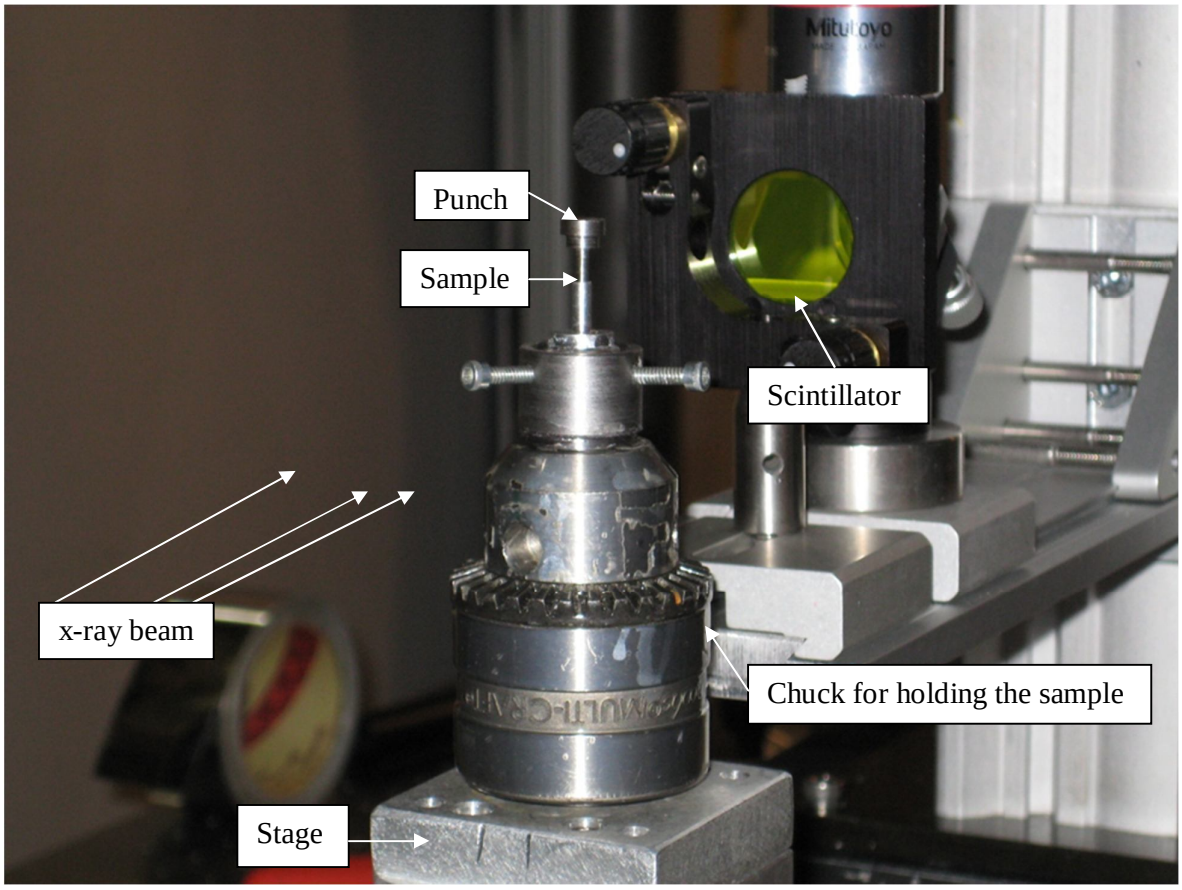

Figure 3.14 Photo of specimen ready for scanning at Argonne National Laboratory.

3.4.2 Scan Analysis and Image Reconstruction

The CT scanning process generates the raw data of the image in binary format. Three different scans (labeled as A, B, and C) were acquired to cover the entire height of the specimen for both configurations, since it was not possible to scan the entire specimen at once. The Interactive Data Language (IDL) software was used to process the raw data. IDL procedures were developed by the research team to truncate the overlapping area between adjacent scans and to reconstruct the images. A new volume file was generated, which was

applied in further analysis. The summary of both configuration scans is summarized in Table 3.2.

The analysis included visualization of particle, particle tracking, and volume rendering. A commercial visualization software, AVIZO, was used to meet the research goals. The steps followed in both IDL and AVIZO are briefly described in Figure 3.18. The analysis steps in AVIZO and results will be presented in Chapter four.

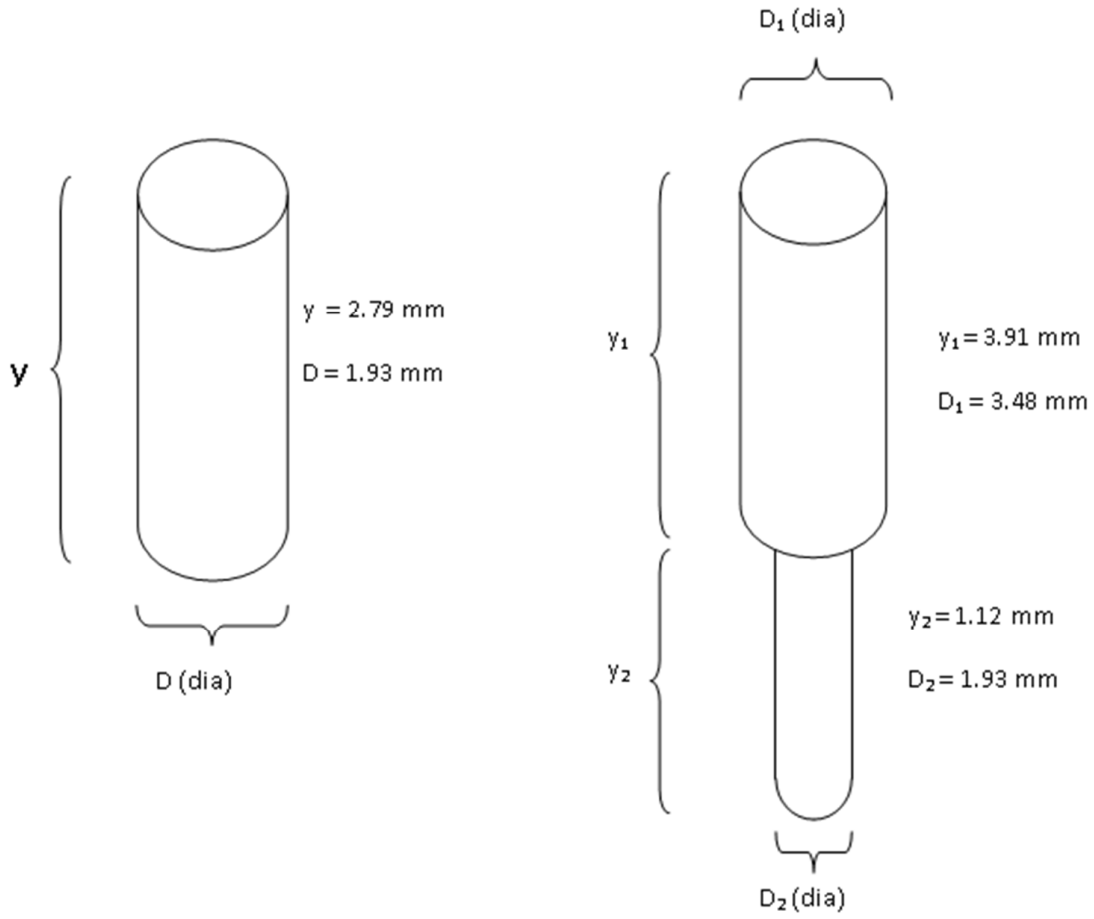

Figure 3.15 Dimensions of the dies.

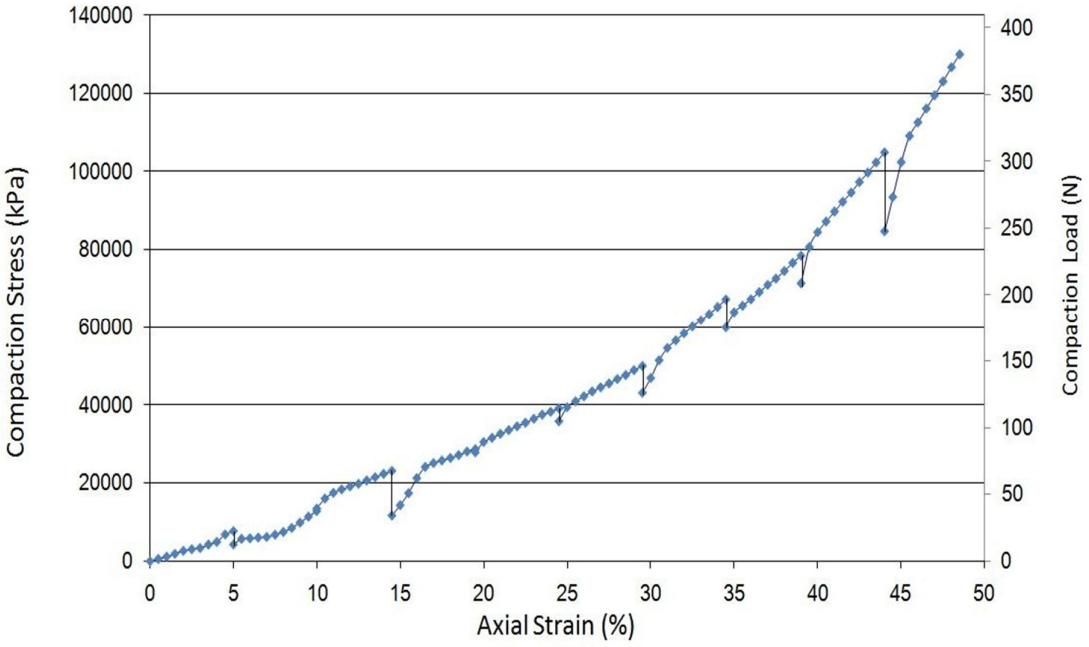

Figure 3.16 Stress versus strain relationship of compaction configuration I (Yang, 2011).

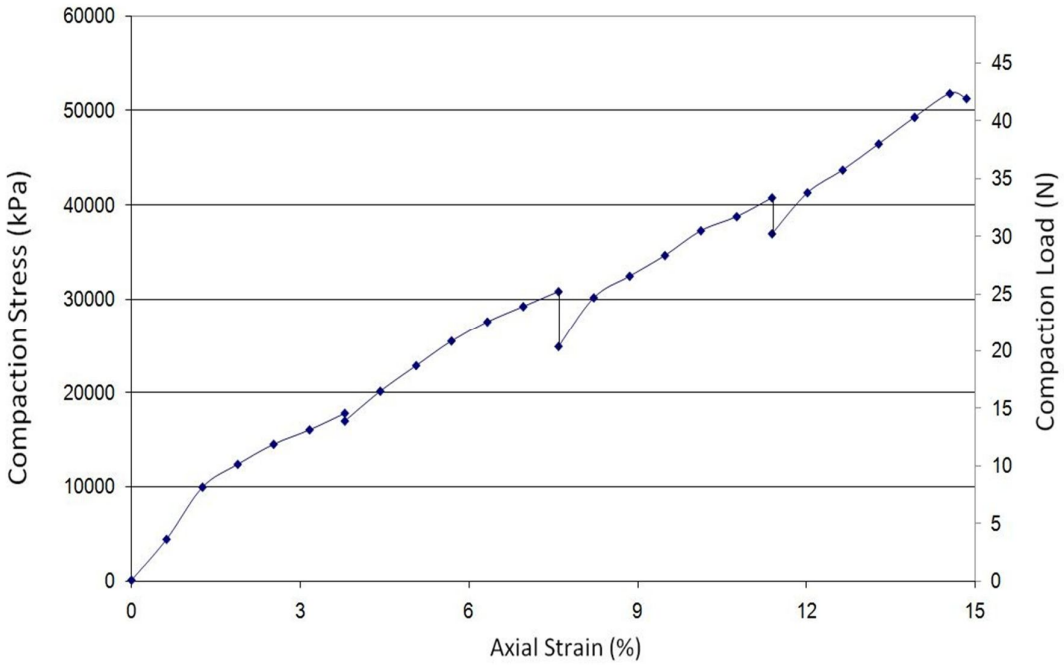

Figure 3.17 Stress versus strain relationship of compaction configuration II (Yang, 2011).

Table 3.2 Summary of test scans.

Material	Conf.	Specimen Dimensions	Initial Volume (mm^3)	Initial Weight (g)	Initial Density (g/cm^3)	Maximum Stress (kPa)	Maximum Load (N)	Maximum Strain (%)	Scanning Energy (kev)	Voxel Size (μm)	Scanning Strain (%)
Aluminum Powder CERAC A-1208 (grain size = less than 149 μm)	I	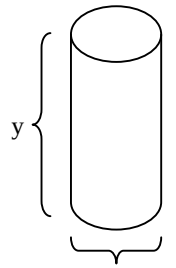	8.17	$9.97x10^{-3}$	1.22	$1x10^{6}$	44.68	50	27	4.96	0 5 10 15 20 25 30 35 40 45 50
	II	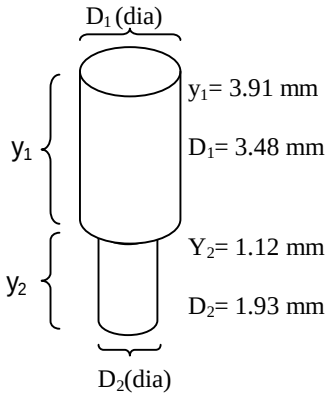	14.86	$2.31x10^{-3}$	1.56	$1x10^{6}$	14.97	12			0 3 6 9 12

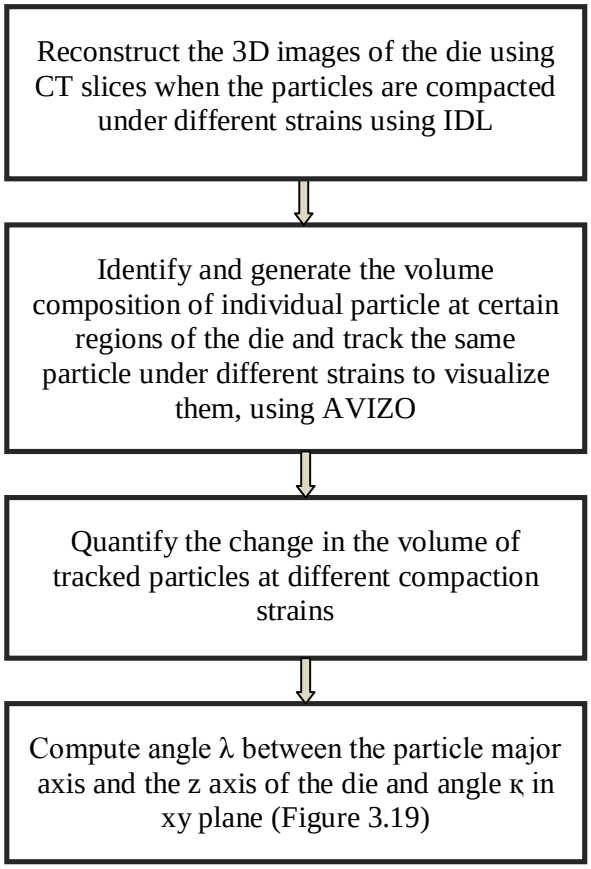

Figure 3.18 Flowchart describes analysis steps.

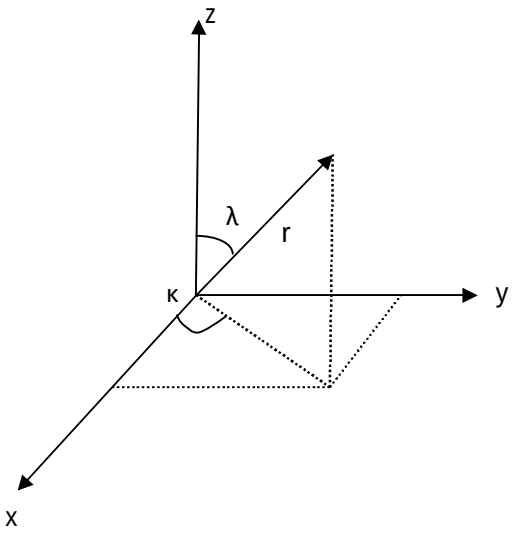

Figure 3.19 Definition of rotation angles.

CHAPTER FOUR
SYNCHROTRON MICRO TOMOGRAPHY (SMT) SCANS

4.1 INTRODUCTION

The preparation of the specimen, the scanning process, and the geometry of the two configurations are described in Chapter three. This chapter mainly focuses on image processing, the procedure to generate a full volume image, the process of tracking the particles, volume generation, and an analysis of rotation of particles.

4.2 IMAGE PROCESSING

The scans were saved as "*recon.volume"* file format after finishing the scanning process. They were processed by using IDL and MS DOS programs to convert them from "*recon.volume"* format to *binary* format. The process is described in Figure 4.1.

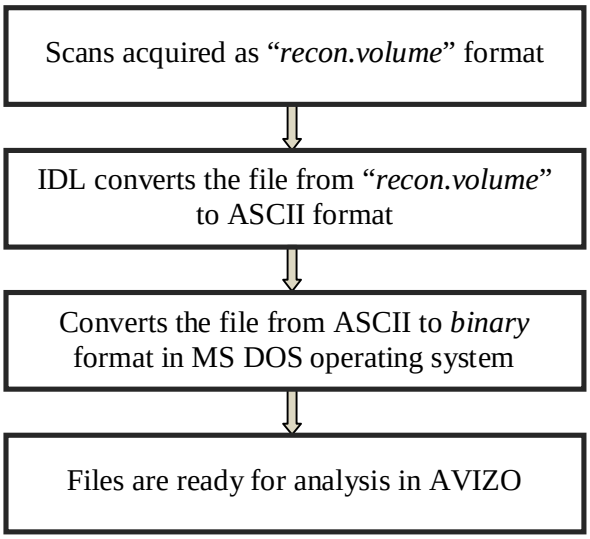

Figure 4.1 Flowchat describes the process of converting the files format.

4.3 COMPILATION OF FULL VOLUME IMAGE

As mentioned in Chapter three, it was not possible to acquire the scan of the entire specimen height at once, due to the large height of the specimen. The scans were saved in two different volume files up to 20% compaction strain, and labeled as A and B for configuration I. The specimen was compressed due to a large compaction strain; the scans were saved in one file after a 20% compaction strain. All scans were saved in three different parts, and labeled as A, B, and C for all the compaction strains of configuration II. The scans have common overlapping portions for each compaction strain. It was necessary for the overlapping portions to be removed, and the remaining portions jointed for the generation of the full volume image. The removal and combination of images were done by means of AVIZO and IDL softwares.

Two different scan sets of a specific compaction strain were opened in two different windows in AVIZO for conducting the analysis. Every single scan is composed of a specific number of slices in x, y, and z axis. The overlapping parts exist only in the z-axis. The entire volume image was generated by removing the overlapping portions from the z-axis. The slice number that matched for both scans was noted carefully. For example, Figures 4.2 and 4.3 display similar slices of two different parts for 0% compaction strain of configuration I. The next step was to remove the overlapping slices. The final slice number for different compaction strains is summarized in Table 4.1, and the details of the image stitching process are depicted in Figures 4.4 and 4.5.

4.4 TRACKING OF PARTICLES

Tracking of the same particle at different compaction strains was the most challenging task of this research. The following properties were the main identifying factors during the tracking process.

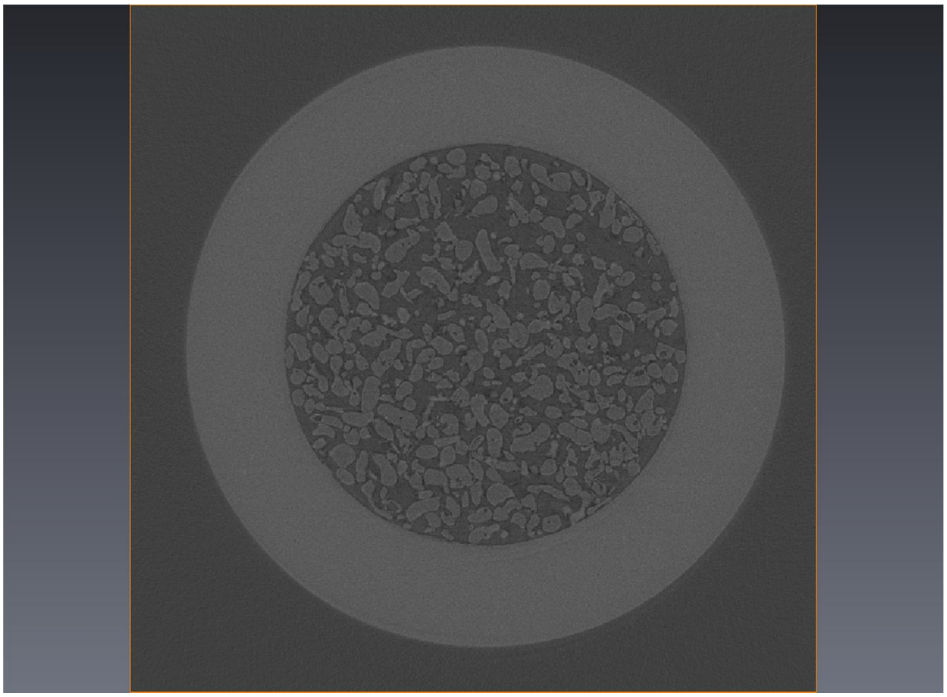

Figure 4.2 Slice number 519 of part A at 0% compaction strain for configuration I.

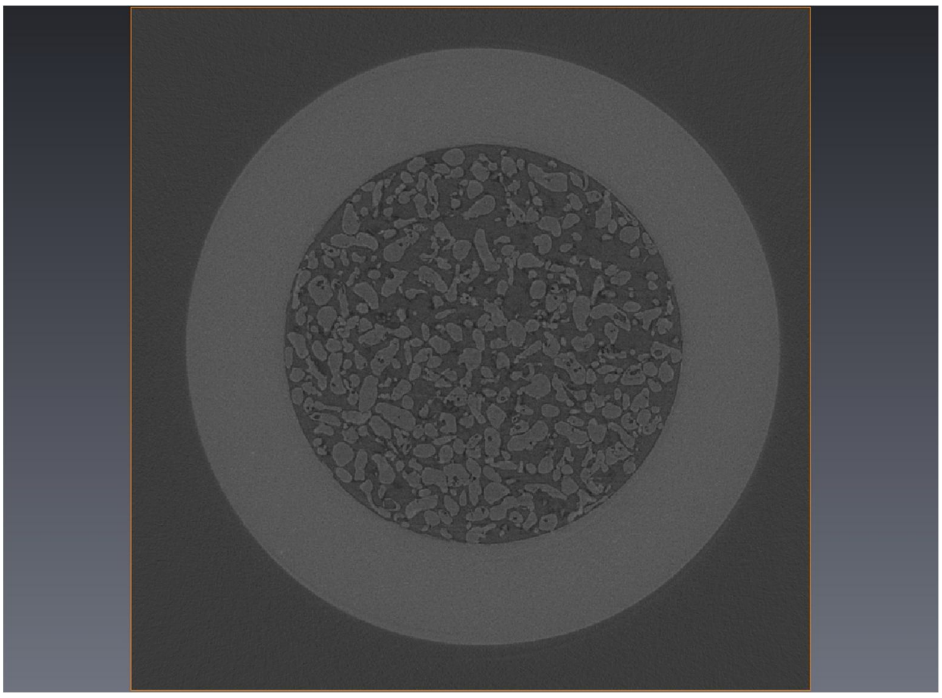

Figure 4.3 Slice number 398 of part B at 0% compaction strain for configuration I.

Table 4.1 Summary of scans in both configurations. Size of each slices in x and y directions are 696 x 696 pixels.

Configuration Type	Number of Slices in z-directions	Compaction Strain (%)
I	642	0
		5
		10
		15
		20
	520	25
		30
		35
		40
		45
		50
II	1171	0
		3
		6
		9
		12

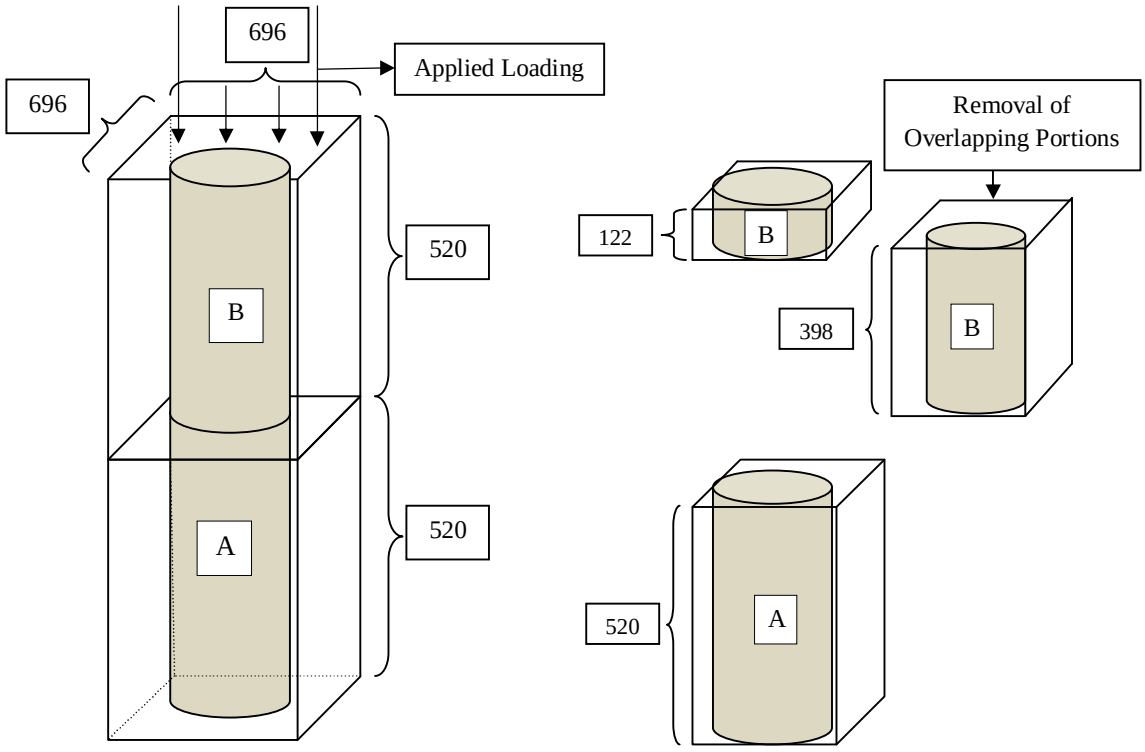

Figure 4.4 Number of slices in parts A and B for configuration I.

- Shape of the particles.
- Relative position of the adjacent particles.
- Coordinates of the particles.

Few particles were chosen in regions of interest for the purpose of identifying and tracking. For configuration I, two clusters were chosen near the top and bottom punches as illustrated in Figure 4.6, whereas, for configuration II, the clusters were chosen to be near the loading plate and the curved boundary, as depicted in Figure 4.7.

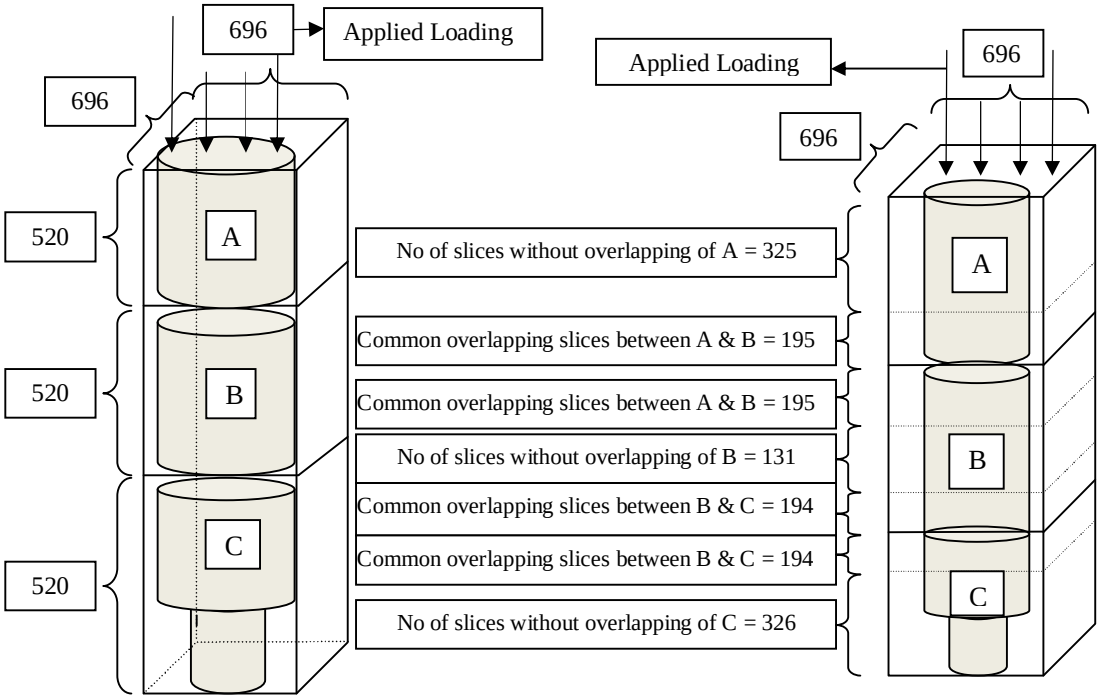

Figure 4.5 Number of slices in parts A, B, and C for configuration II.

At first, the volume image data file was opened by using AVIZO. The software can display the slices in xy, yz, and zx axes. The particles in a specific zone were first selected for 0% compaction strain and would be tracked for the subsequent compaction strains. The next images of the compaction strain data file (e.g. 5%, 10%, etc.) were opened in another AVIZO window. The slices of yz axes were then slowly monitored to find the same particles. If a particle at 0% compaction strain was located in yz axes at slice # 10, it would be found for the next compaction strain at slices # 30 to 40 of yz axes, as well as slice # 60 to 70 for the next compaction strain due to compaction.

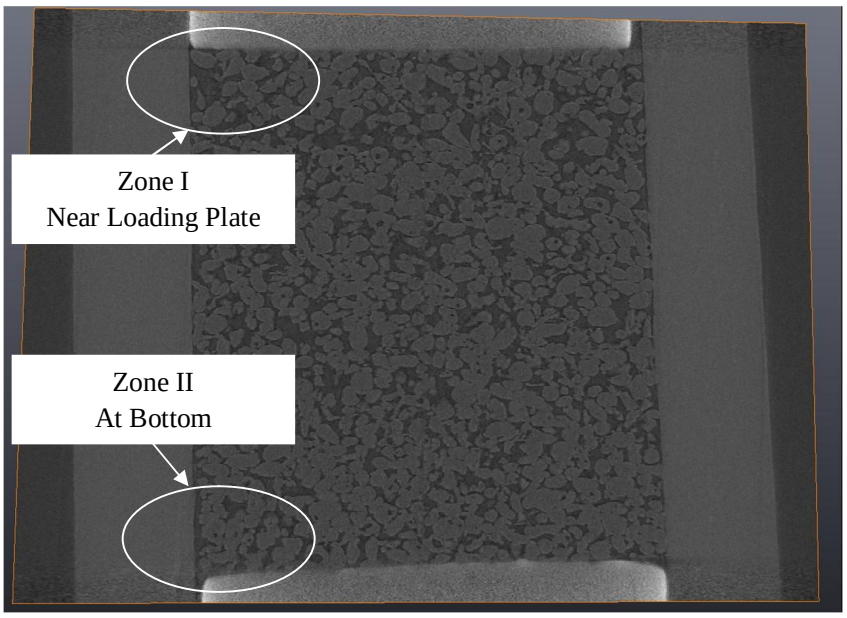

Figure 4.6 Zone of interest to track particles for configuration I.

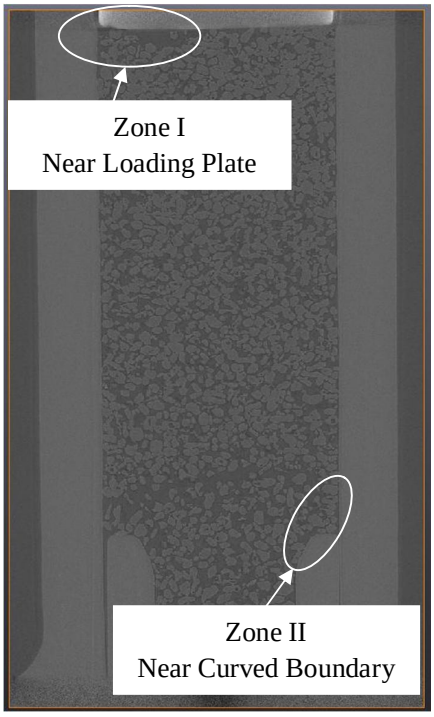

Figure 4.7 Zone of interest to track particles for configuration II.

The other fact in tracking the particles was the relative position of adjacent particles. It was found that the particle position, with respect to other particles never changes drastically throughout the scans. In addition, the particles x,y coordinate rarely changed as compaction progressed. The changes occurred only in the z coordinate, due to compaction. A group of particles tracked at different scans for a specific compaction strain is depicted in Figure 4.8 as an illustrative example.

4.5 VOLUME GENERATION

Particle volume identification and generation was the next step in the analysis and the entire process was conducted using AVIZO software. The image was first segmented and the particle of interest was identified by coloring it, using the "brush" tool of AVIZO. Figure 4.9 illustrates the three different directions of a single data file. It should be noted that the region that was selected for the first compaction strain level must be maintained in all other strain levels to avoid an error in volume calculation. Different tools are available for coloring in AVIZO, such as "pick region", "brush tool", "lasso", "magic wand", "blow", etc. "Brush" tool was used in this research. Each particle was identified using a separate name during coloring; otherwise, volume calculation would be in error if all particles were colored under one particle name. The process was repeated for the other two directions after finishing the coloring in one direction. The full volume of a single particle was generated after coloring the slices of all three directions contained in that particle. The whole process for volume generation is described elaborately in Figure 4.10. Figure 4.11 presents an illustration of the same generated particle at different compaction strains.

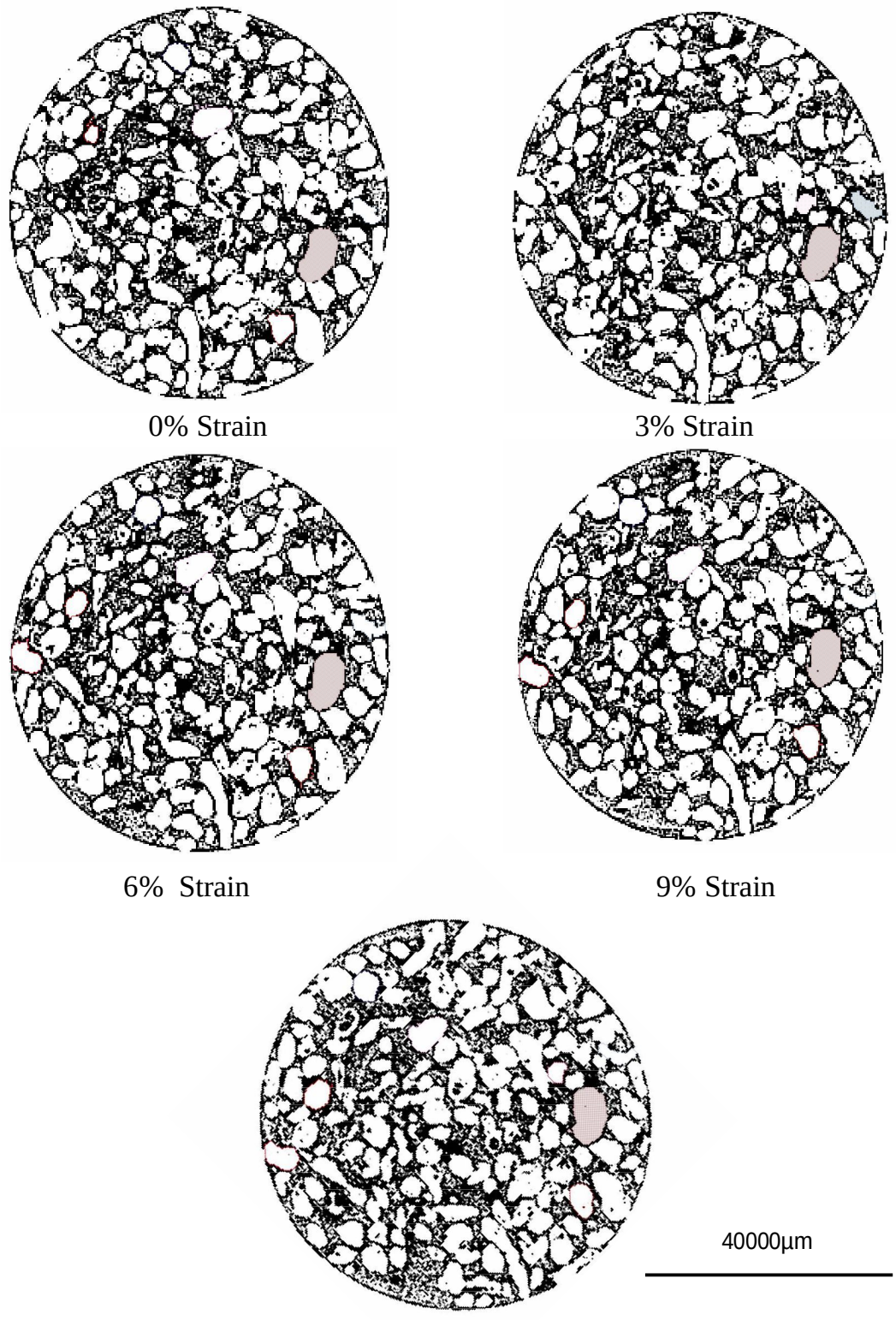

Figure 4.8 Same group of particles at different strains in configuration II.

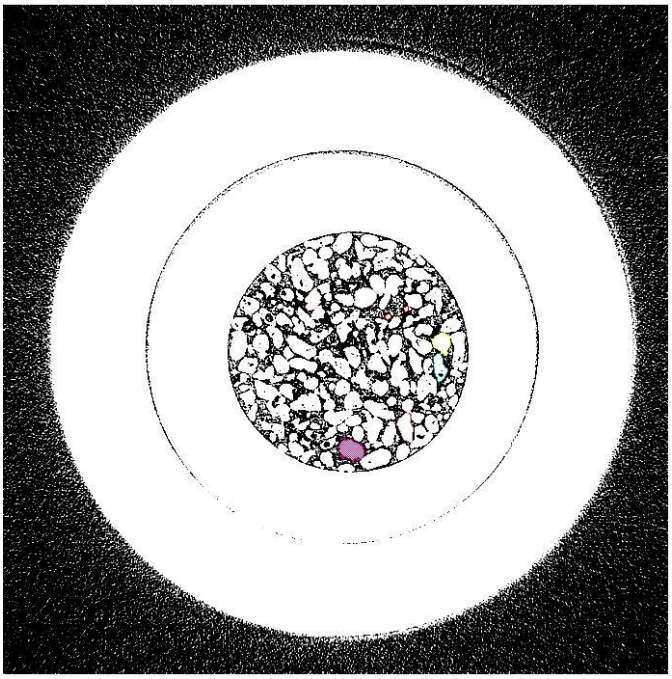

Direction xy

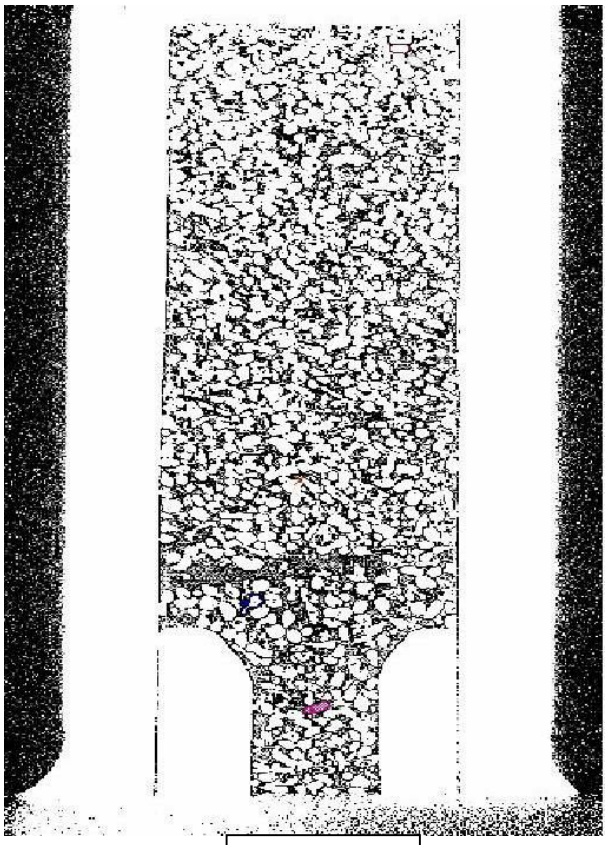

Direction xz

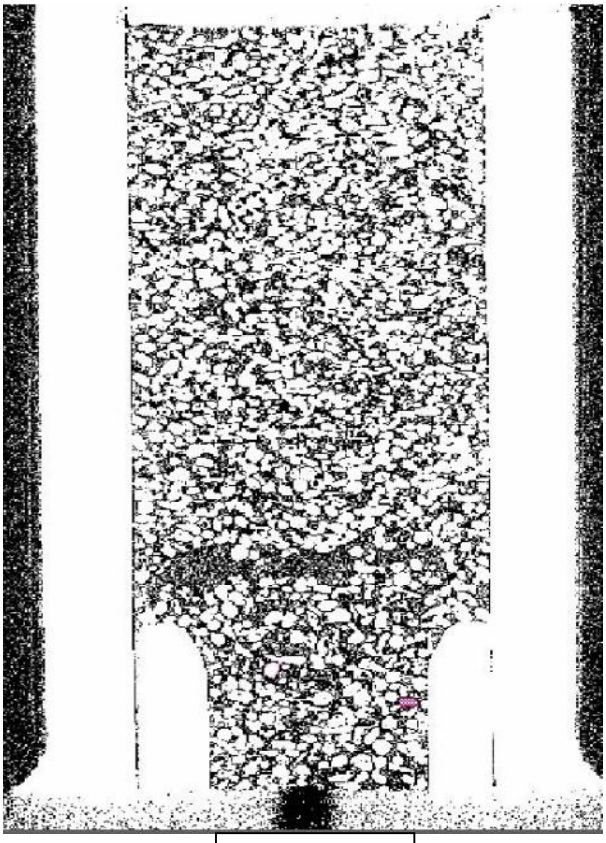

Direction yz

Figure 4.9 Example of three different directions of a single volume file.

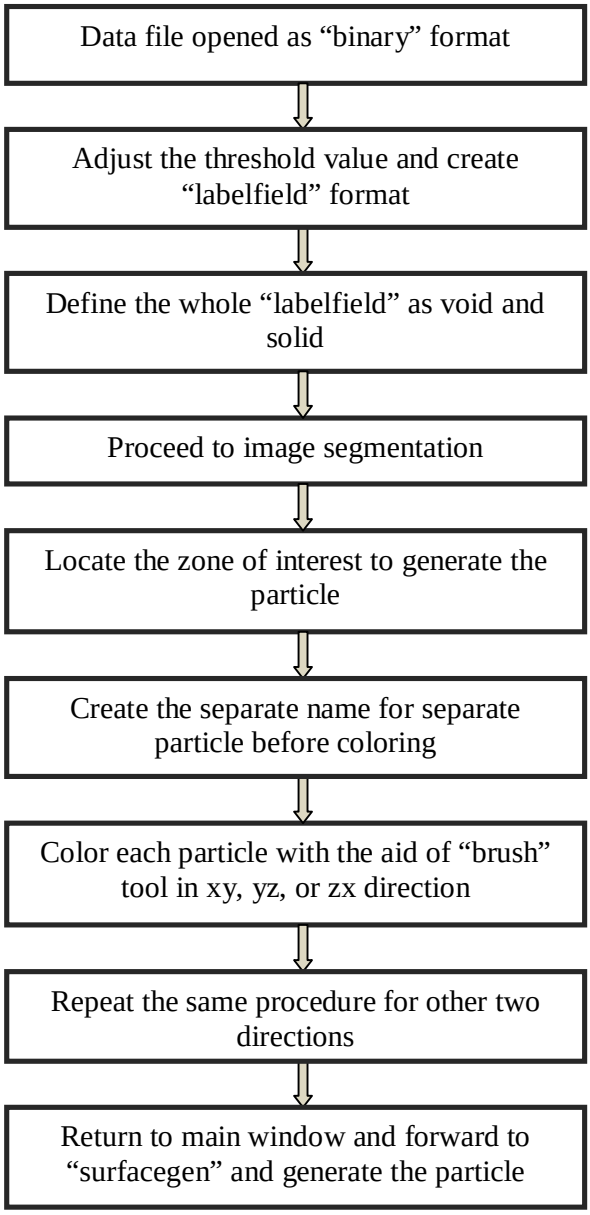

Figure 4.10 Flowchart for volume generation.

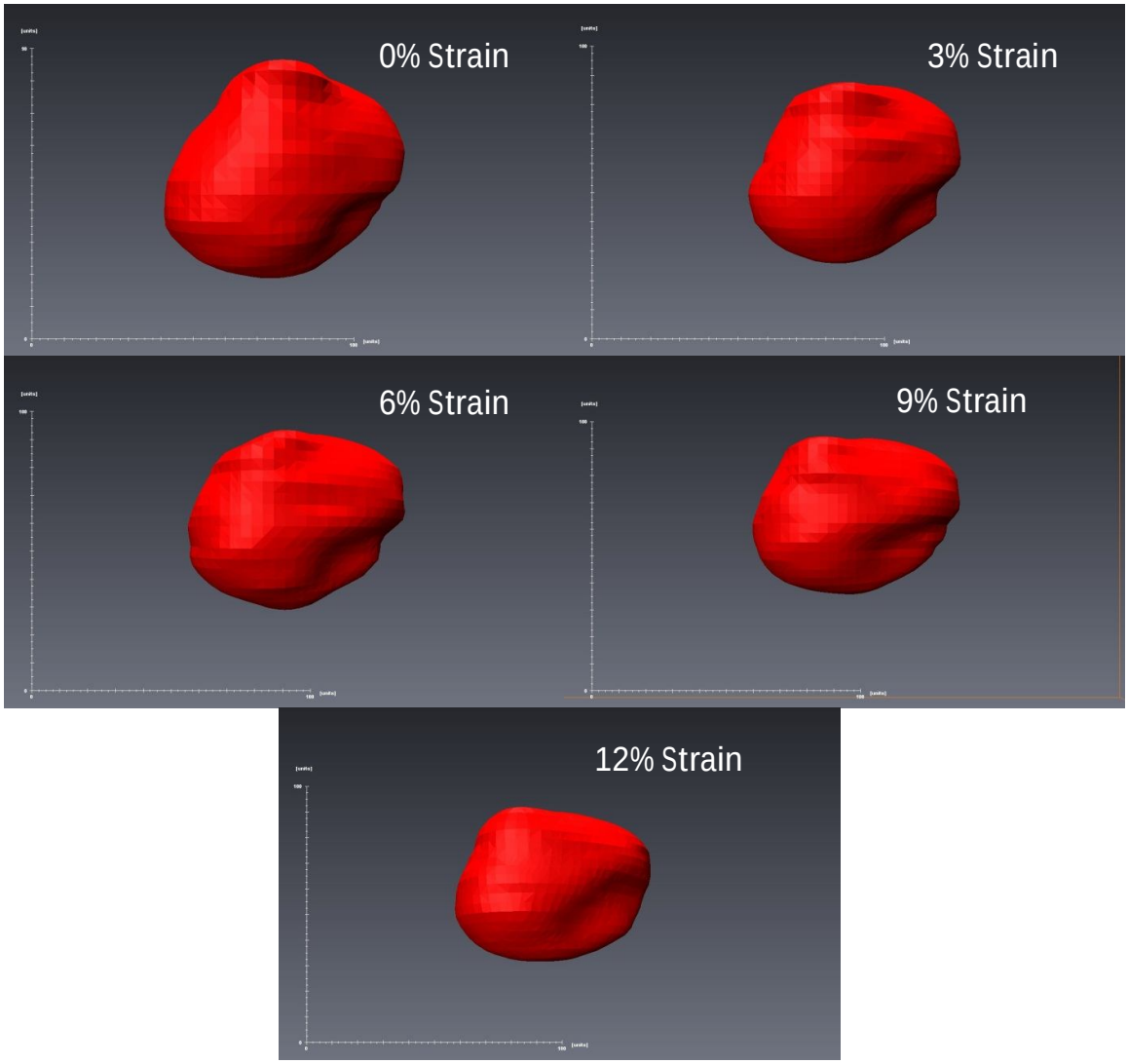

Figure 4.11 3D visualization of same particle at different strains in configuration II.

4.6 DETERMINATION OF PARTICLE ROTATION

The next step was to determine the rotation of particles with respect to the z-axis and xy plane (Figure 3.19). This task was conducted using AVIZO software. There is no tool in AVIZO to perform this task automatically. Therefore, manual tools such as “2d length” and “3d angle” were used to acquire the measurements. Particles that were generated in the volume generation process were considered for determination of the angle. This whole

process was conducted using the "*labelfield*" file format, rather than the "*binary*" format of AVIZO. It was challenging to measure both λ and κ at the same time. Therefore, λ was determined first for all particles and κ was determined in the next step. The process to determine those angles varied from one to another. It was necessary to determine the long (major) axis of the particle which would be used in the next step for determining λ and κ. The "2d length" module was used for this task. The long axis was drawn to fix the "orthoslice" at the tip point of that particle. Figure 4.12 illustrates an example of fixing the "orthoslice" at the particle. The "3d angle" tool was used to measure the angle between the particles with respect to xy axes. The procedure for determining angles λ and κ is presented in Figures 4.13 and 4.14, respectively. Since all angles were determined manually, there was a possibility of operational error. To avoid this error, finding the tip point, setting up the "orthoslices", and drawing the lines were done carefully. Illustrative examples of determining λ and κ in AVIZO are depicted in Figures 4.15 and 4.16, respectively.

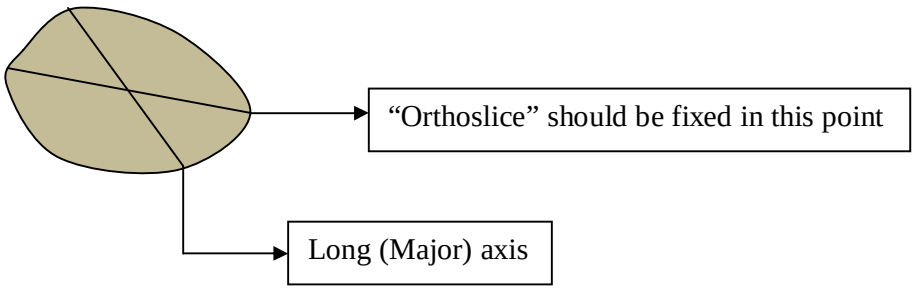

Figure 4.12 Illustrative example of fixing the "orthoslice" at the particle.

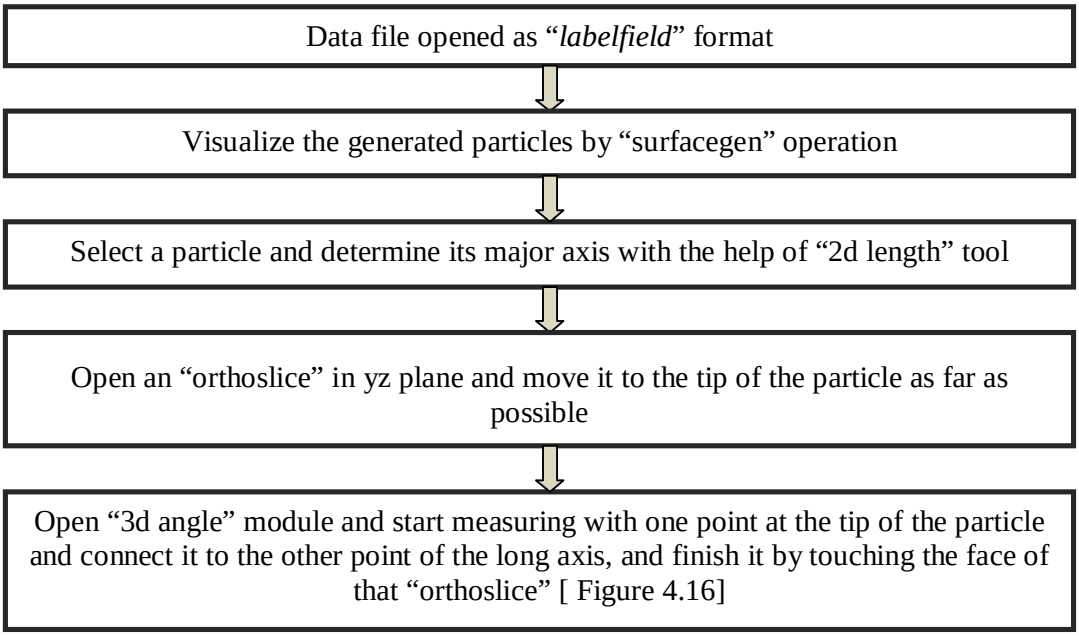

Figure 4.13 Flowchart of steps to measure angle λ.

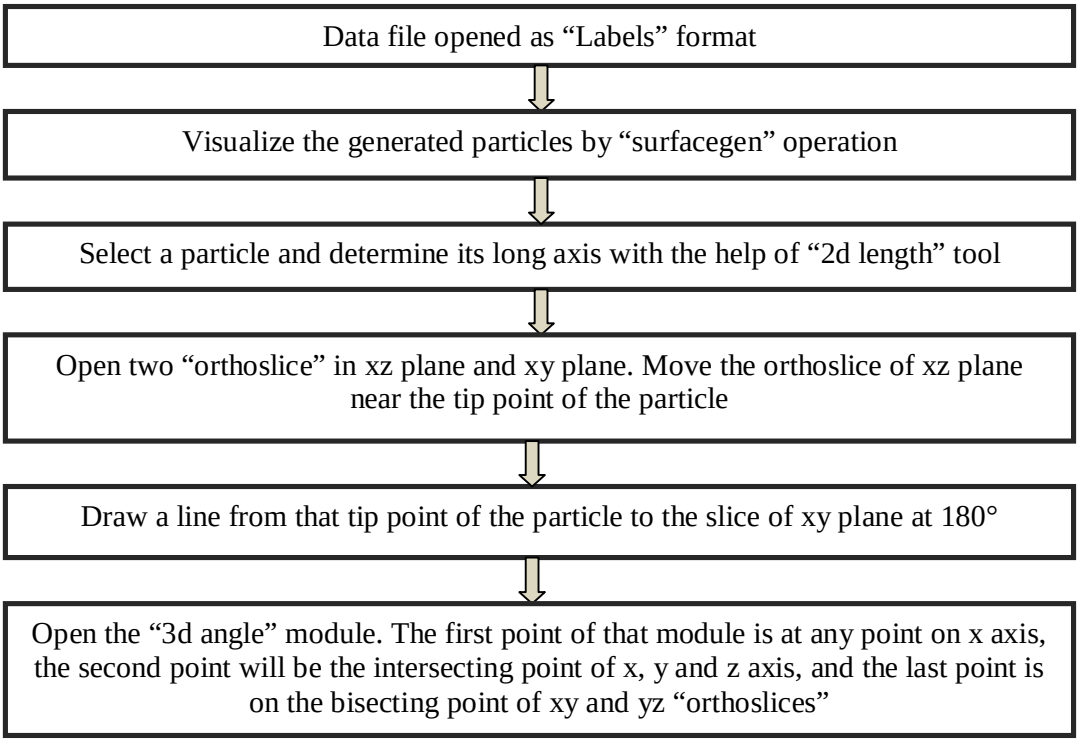

Figure 4.14 Flowchart of steps to measure angle κ.

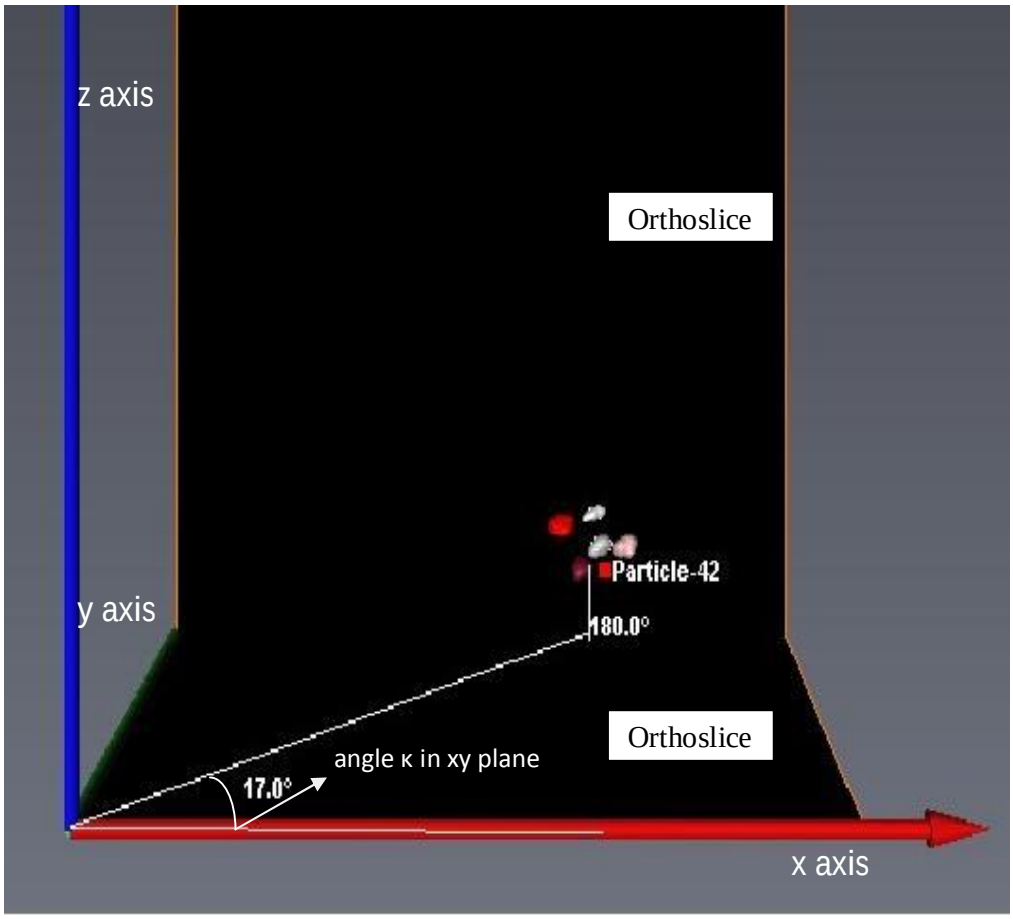

Figure 4.15 Illustrative example to determine angle κ.

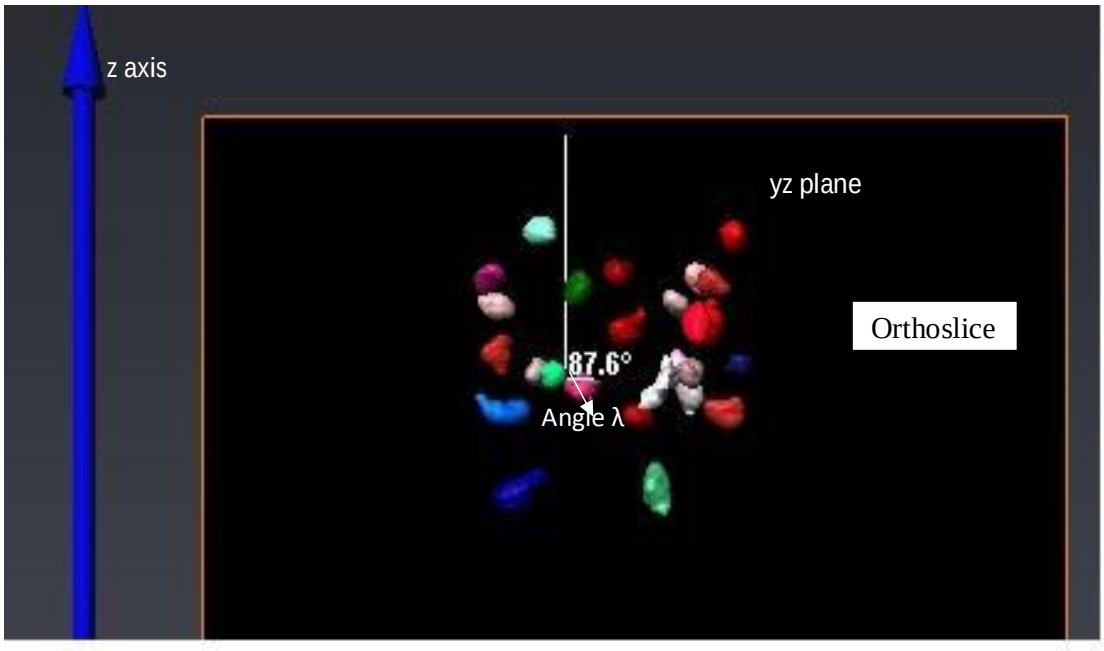

Figure 4.16 Illustrative example to determine angle λ.

CHAPTER FIVE
RESULTS AND DISCUSSION

5.1 INTRODUCTION

Chapter 4 describes the processing of data files, the 3D shape generation of particles, and analysis of particle orientation angle. The data of the analyzed particles are mainly presented and discussed in this Chapter, which also includes visualization of the generated particles at different regions and their subsequent analyses.

5.2 PARTICLES VISUALIZATION

This section describes particle identification and compares their volume under different compaction strains. Sixty particles were tracked and colored for the analysis of volumetric and rotational behavior. Table 5.1 lists the number of tracked particles for the two die configurations and Figures 5.1 and 5.2 display an image of the tracked particles for 0% compaction strain for configurations I and II, respectively. The images of tracked particles in different strains are presented in Appendix A.

Table 5.1 Number of particles generated at different regions of the two die configurations.

Configuration	# of Scans	Zone	# of Particles
I	11	I	9
		II	8
II	5	I	5
		II	38

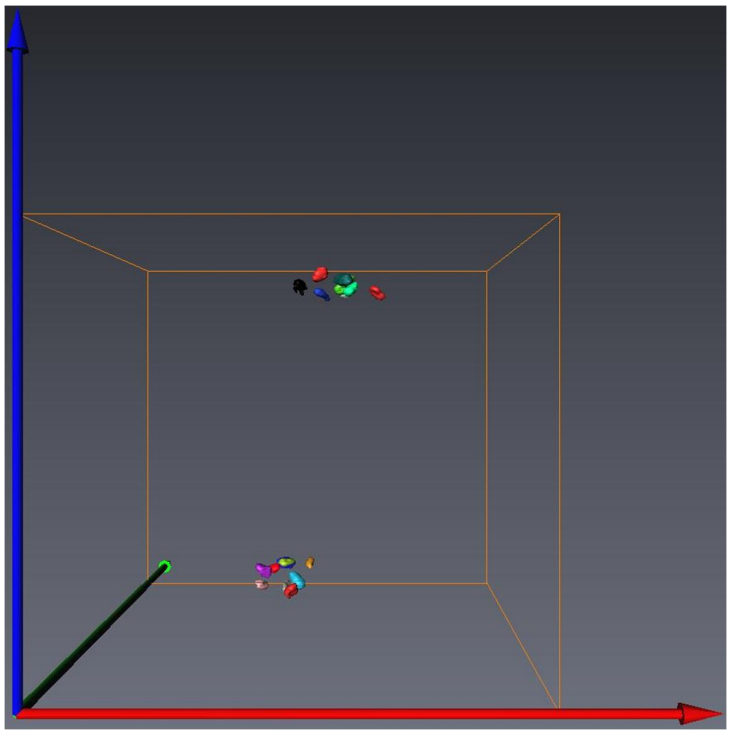

Figure 5.1 Particles for configuration I at 0% compaction strain.

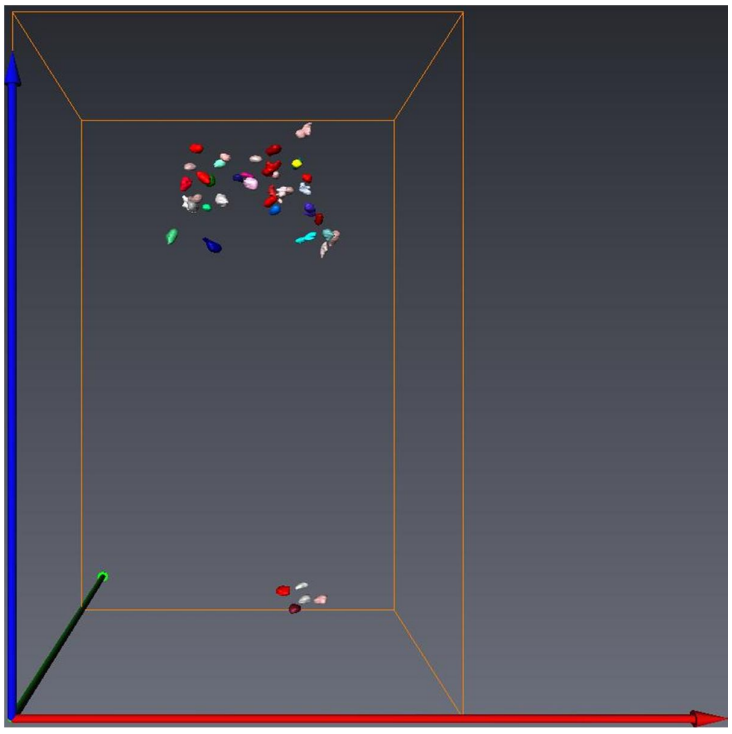

Figure 5.2 Particles for configuration II at 0% compaction strain.

5.3 VOLUMETRIC ANALYSIS

A certain number of particles were tracked and colored at locations of interest for each scan. AVIZO software provides all the desired measurements using the *material statistics* option. It provides the volume size in voxel and compares the present volume with the initial volume to calculate the change in particles volumetric strain. It was observed that as the compaction strain increases, there is a significant change in the volumetric strain of the particles, as depicted in Figures 5.3 through 5.6.

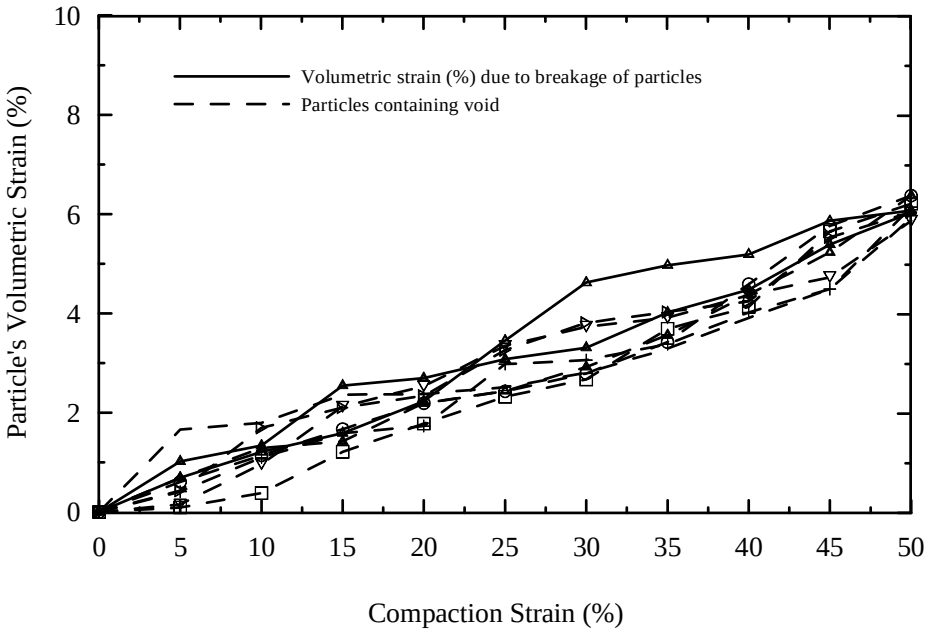

Figure 5.3 Volumetric analysis of particles in zone I of configuration I.

Figure 5.3 depicts the volumetric analysis for zone I of configuration I, which shows that the volumetric strain of the particles decreased along with compaction strain. The maximum and minimum volumetric strain for the nine particles of zone I are about 6.4% and 5.8%, respectively. The average particles volumetric strain is 2.87% and 6.12% for 25% and

50% compaction strains, respectively. The change of volumetric strain was initially negligible for the particles. Then the volumetric strain decreased significantly after 25% compaction strain. The presence of loading plate near that particle region influenced the behavior. The breaking of some particles at high compaction strains also resulted decrease in volumetric strain. It was observed that there was a presence of voids in some particles. These voids facilitated the breakage of particles and yielded more volumetric strain. Table 5.2 presents the data of the volumetric strain of the particles for configuration I.

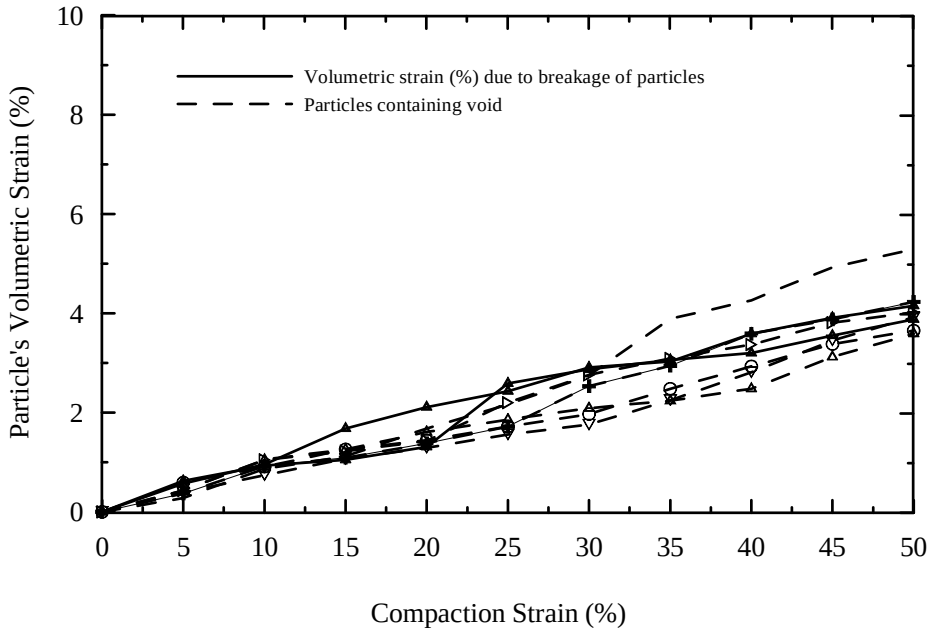

Figure 5.4 Volumetric analysis of particles in zone II of configuration I.

The volumetric analysis for zone II of configuration I is shown in Figure 5.4. One can notice that the volumetric strain for particles is much less than zone I, since it was near the bottom of the die (see Figure 4.6). On average, the particles volumetric strain decreased at the end of compaction by 8%. The average values for particles volumetric strain are 2.04% and 4.10% for 25% and 50% compaction strains, respectively. There was a noticeable decrease in

volumetric strain after 40% compaction strain since some particles began to break into small pieces at high compaction strains.

Table 5.2 Particles volumetric strain data for volume analysis of configuration I.

		Compaction Strain (%)										
		0	5	10	15	20	25	30	35	40	45	50
		Particles Volumetric Strain (%)										
Particles in Zone-I	1	0	1.66	1.80	2.36	2.38	2.51	2.80	3.29	3.91	4.47	5.92
	2	0	0.41	1.10	1.59	1.73	2.98	3.06	3.38	4.02	4.49	6.14
	3	0	0.61	1.14	1.67	2.19	2.43	2.79	3.42	4.59	5.76	6.37
	4	0	0.43	1.69	2.11	2.34	3.26	3.81	4.03	4.24	5.53	6.04
	5	0	0.69	1.29	1.42	2.19	2.44	2.92	3.56	4.38	5.23	6.41
	6	0	0.15	0.96	2.12	2.54	3.35	3.73	3.91	4.37	4.73	5.86
	7	0	0.09	0.38	1.21	1.78	2.32	2.67	3.69	4.13	5.65	6.21
	8	0	1.02	1.34	2.55	2.69	3.08	3.31	4.02	4.48	5.39	6.03
	9	0	0.69	1.21	1.59	2.23	3.45	4.62	4.97	5.19	5.86	6.07
Particles in Zone-II	11	0	0.28	0.87	1.12	1.68	2.16	2.75	3.89	4.26	4.93	5.29
	12	0	0.37	0.92	1.09	1.38	1.72	2.53	2.94	3.59	3.88	4.23
	13	0	0.59	0.91	1.26	1.44	1.79	1.97	2.48	2.93	3.38	3.65
	14	0	0.43	1.05	1.22	1.43	2.20	2.76	3.09	3.37	3.81	4.02
	15	0	0.62	0.93	1.05	1.31	2.59	2.87	3.06	3.20	3.55	3.88
	16	0	0.39	0.74	1.07	1.29	1.56	1.76	2.25	2.81	3.45	3.92
	17	0	0.57	0.96	1.68	2.11	2.43	2.91	3.03	3.59	3.91	4.15
	18	0	0.43	1.05	1.26	1.61	1.86	2.09	2.24	2.48	3.12	3.59

Figure 5.5 depicts the change in volumetric strain of particles in zone I of configuration II versus the compaction strain (%), which shows that the volumetric strain of the particles decreased with the increase of compaction strain in a similar fashion as demonstrated in configuration I. The volumetric strain of the particles decreased by 1.00%, 1.72%, 2.82%, and 3.91% at 3%, 6%, 9%, and 12% compaction strains, respectively. The tracked particles exhibited a minimum volumetric strain of 3.57% whereas; the maximum value for the volumetric strain is 4.17%. However, the final average value of volumetric strain is 3.91%. The volumetric strain of particles in zone I was significantly higher than zone

II due to the presence of the loading plate near the top of the die, which caused the particles to compact and break down into small pieces. Particles far away from zone I were less affected by the loading plate, thus, volumetric strain was insignificant.

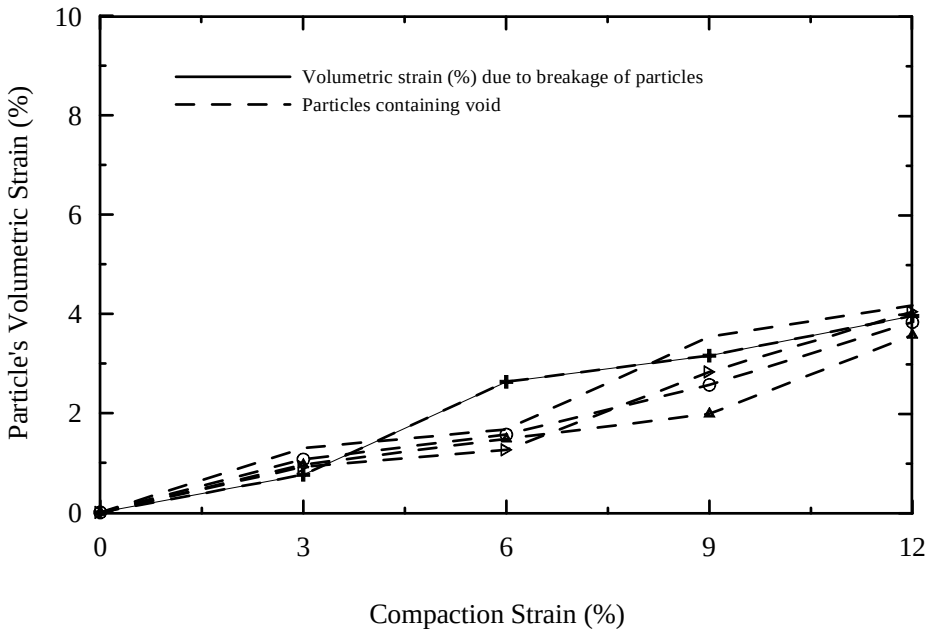

Figure 5.5 Volumetric analysis of particles in zone I of configuration II.

The volumetric strain of the particles versus compaction strain within zone II of configuration II is shown in Figure 5.6 which displays a similar trend to the previous volume analysis. The volumetric strain of particles was insignificant initially; however, it decreased with increasing compaction strains and finally reached 2.6% at 12% compaction strain. The highest value of volumetric strain is 3.81%, whereas the lowest is 1.07% among the 38 tracked particles. The volumetric strain was less in this particular region, compared to zone I, since this zone was adjacent to the bottom of the die. The values of particles volumetric strain for configuration II are listed in Table 5.3.

5.3.1 Discussion of Volumetric Analysis

It is evident that a noticeable change in particles volumetric strain is observed as compaction strain increases from the plots of volumetric analysis. On average, the particles volumetric strain decreased by 6% and 4% for zones I and II of configuration I, respectively (Figure 5.7). The volumetric strain was much less for configuration II than configuration I since configuration II was subjected to only 12% compaction strain, compared to 50% compaction strain for configuration I. Figure 5.8 shows that the final volumetric strain value of particles for zones I and II of configuration II is about 4% and 2.5%, respectively. However, it is easy to observe from Figures 5.7 and 5.8 that the volumetric strain of the particles decreased in zone I more than zone II, because zone I was adjacent to the loading plate for the two die configurations.

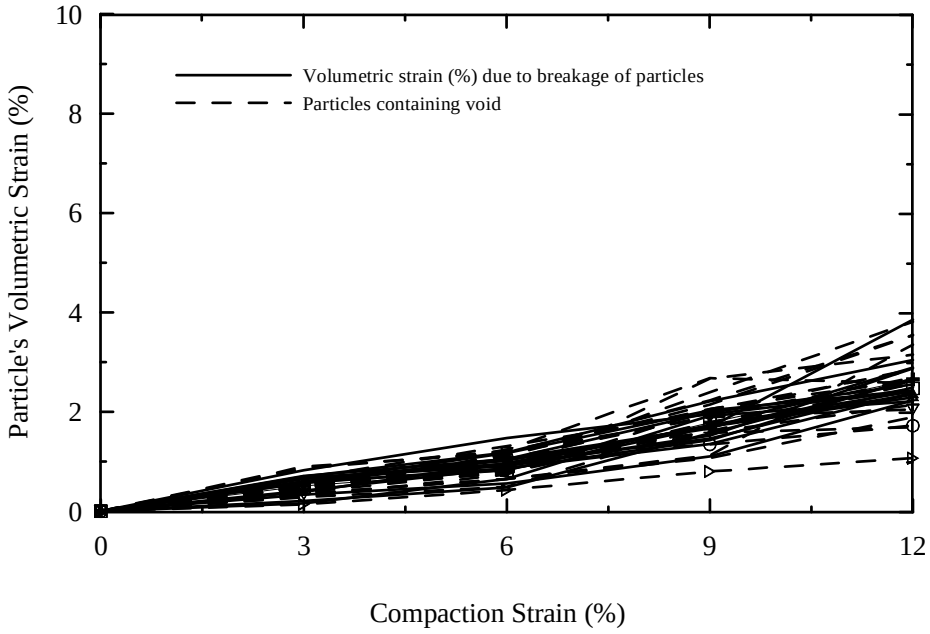

Figure 5.6 Volumetric analysis of particles in zone II of configuration II.

Table 5.3 Particles volumetric strain data for volume analysis of configuration II.

	Compaction Strain (%)					
	Particle	0	3	6	9	12
		Particles Volumetric Strain (%)				
Particles in zone II	1	0	0.35	0.65	1.13	3.35
	2	0	0.51	0.81	1.78	2.65
	3	0	0.55	1.08	1.34	1.72
	4	0	0.14	0.43	0.80	1.07
	6	0	0.34	1.17	1.89	2.05
	7	0	0.46	0.82	1.79	2.47
	8	0	0.39	0.97	1.71	2.34
	9	0	0.59	0.83	1.70	2.29
	10	0	0.55	1.05	1.59	2.14
	11	0	0.40	0.97	2.13	2.48
	12	0	0.35	0.65	1.07	1.89
	13	0	0.68	0.92	1.73	2.41
	14	0	0.29	0.74	2.05	2.83
	15	0	0.60	1.02	1.99	2.55
	16	0	0.90	1.17	2.23	3.54
	17	0	0.65	0.96	1.46	2.49
	18	0	0.82	1.47	1.95	2.42
	19	0	0.50	1.06	1.92	2.68
	20	0	0.59	1.17	2.03	2.43
	21	0	0.67	1.31	1.98	2.86
	22	0	0.56	1.24	2.67	2.58
	23	0	0.70	1.18	2.21	3.04
	24	0	0.48	0.76	2.67	3.15
	25	0	0.57	1.02	1.67	2.89
	26	0	0.51	0.89	1.61	2.57
	28	0	0.86	1.21	2.06	2.65
	29	0	0.41	0.87	1.35	2.39
	30	0	0.42	1.12	2.14	3.54
	31	0	0.67	0.91	1.52	2.87
	32	0	0.33	0.56	1.10	2.23
	33	0	0.71	1.05	1.99	2.55
	34	0	0.48	0.93	2.40	3.81
	35	0	0.38	0.79	1.58	1.69
	36	0	0.57	0.86	1.43	2.67
	37	0	0.28	0.49	1.73	2.34
	38	0	0.16	0.65	1.93	2.21
	39	0	0.60	1.06	1.69	3.85
	40	0	0.20	0.48	1.57	2.63
Particles in zone I	41	0	1.30	1.67	3.54	4.17
	42	0	0.76	2.63	3.16	3.96
	43	0	1.07	1.57	2.57	3.83
	44	0	0.92	1.26	2.83	4.04
	45	0	0.96	1.48	1.98	3.57

This change in particles volumetric strain was due to the presence of voids in powders, breakage of particles into small pieces and elasticity. The presence of voids in the particles helped to initiate the breakdown of particles, especially for configuration I when the specimen had experienced high compaction strains (Figure 5.9). It was difficult to track the small fragments of the broken particles at high compaction strains. This breakdown caused a significant change in volumetric strain of particles after 40% compaction strain for both configurations. However, the voids were neglected during the coloring of particles in order to acquire the true measurement for the volume analysis. The breakdown of particles in subsequent scans is depicted in Figure 5.10.

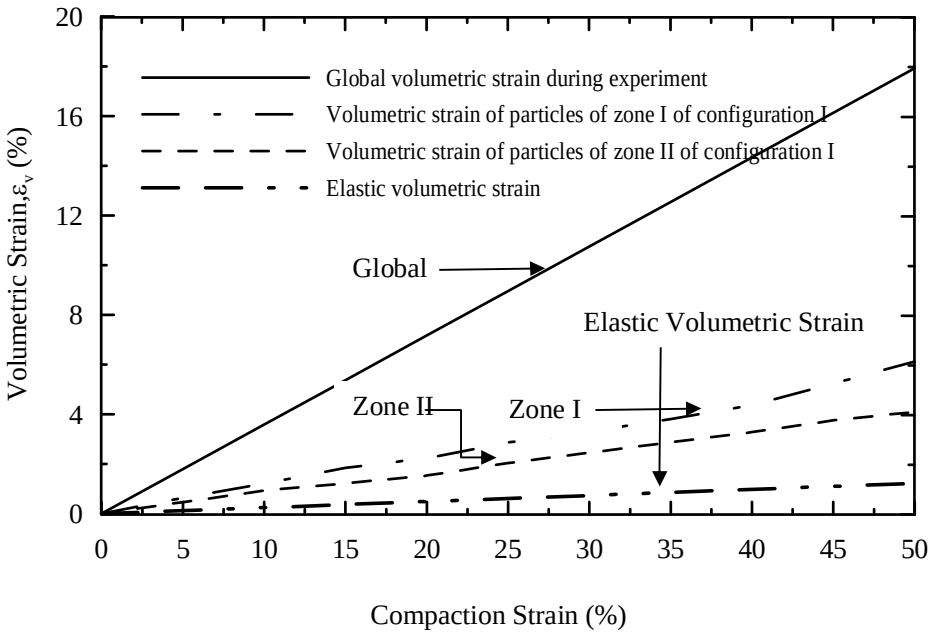

Figure 5.7 Comparison of volumetric strain in different zones of configuration I.

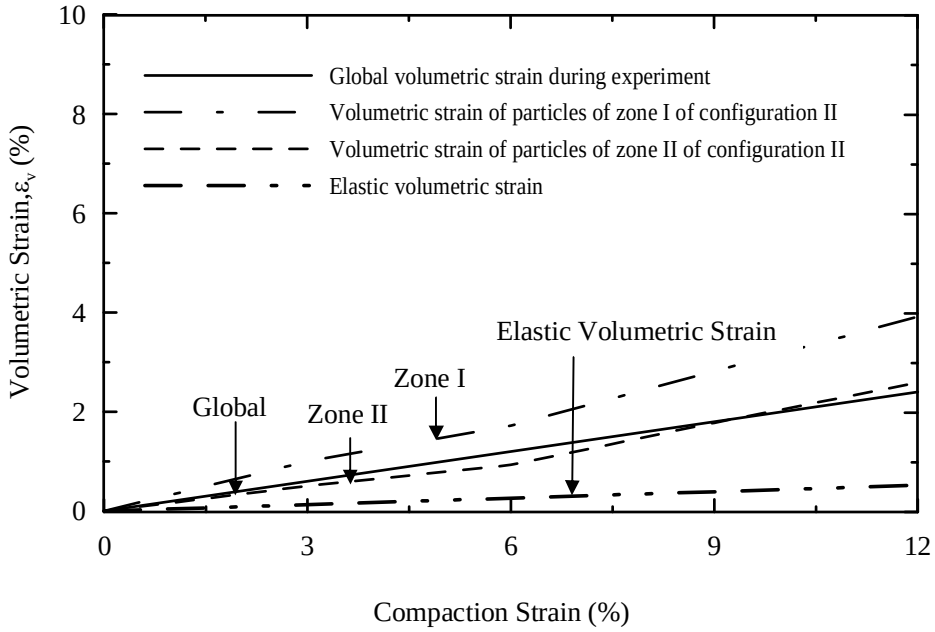

Figure 5.8 Comparison of volumetric strain in different zones of configuration II.

The volumetric strain is referred as the change in volume with respect to the initial volume of the specimens as

$$\varepsilon_v = \frac{\Delta V}{V_o}. \quad \ldots \quad (5.1)$$

Where, ΔV = change in volume and,

V_o = the initial volume.

$$\varepsilon_v = \frac{\Delta H \cdot A}{H_o \cdot A} = \frac{\Delta H}{H_o} \quad \ldots \quad (5.2)$$

Where, ΔH = change in height and,

H_o = the initial height of the specimen.

The initial height of the specimen was 2.79 and 5.03 mm for configurations I and II, respectively (Table 3.2). The value for change in height was obtained from Figures 3.16 and 3.17. Then, global volumetric strain was calculated using Equation 5.2 and displayed in

Figures 5.7 and 5.8. The final global volumetric strain for the specimen was 18% and 3% for configurations I and II, respectively. Configuration II exhibited low global volumetric strain since it experienced less compaction. It also observed that the global volumetric strain decreased linearly with the increase in axial strain.

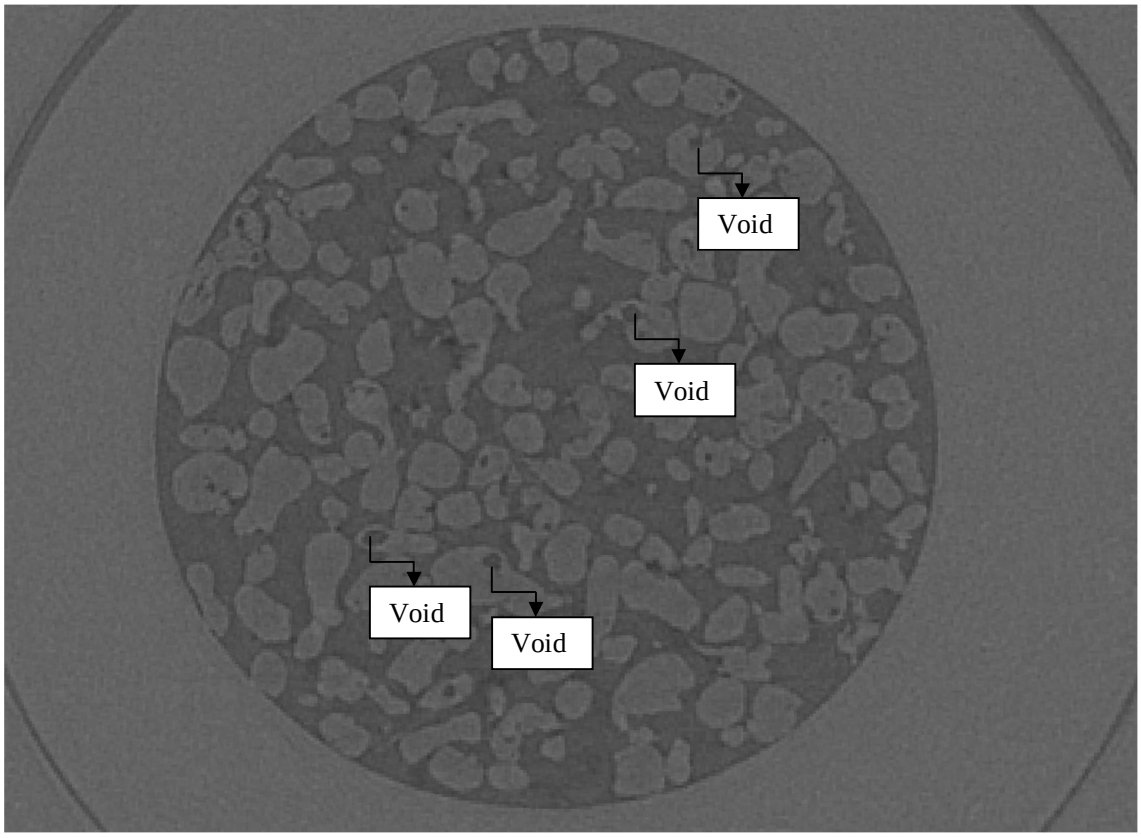

Figure 5.9 Example of presence of voids in powder specimen.

Another considerable contributing factor that influences the particle volumetric strain is the elastic volumetric change. The volume of the particles decreases due to the elastic behavior of the aluminum powder. The elastic volumetric strain is calculated as follows:

The mean stress, $P = \frac{\sigma_1+\sigma_2+\sigma_3}{3}$

Here, $\sigma_2 = \sigma_3$

Assuming coefficient of earth pressure at rest $K_o = \frac{\sigma_3}{\sigma_1}$ has value of 0.5

Yields $P = \frac{\sigma_1 + 2 \text{ X } 0.5\sigma_1}{3} = \frac{\sigma_1 + \sigma_1}{3} = \frac{2\sigma_1}{3}$ … (5.3)

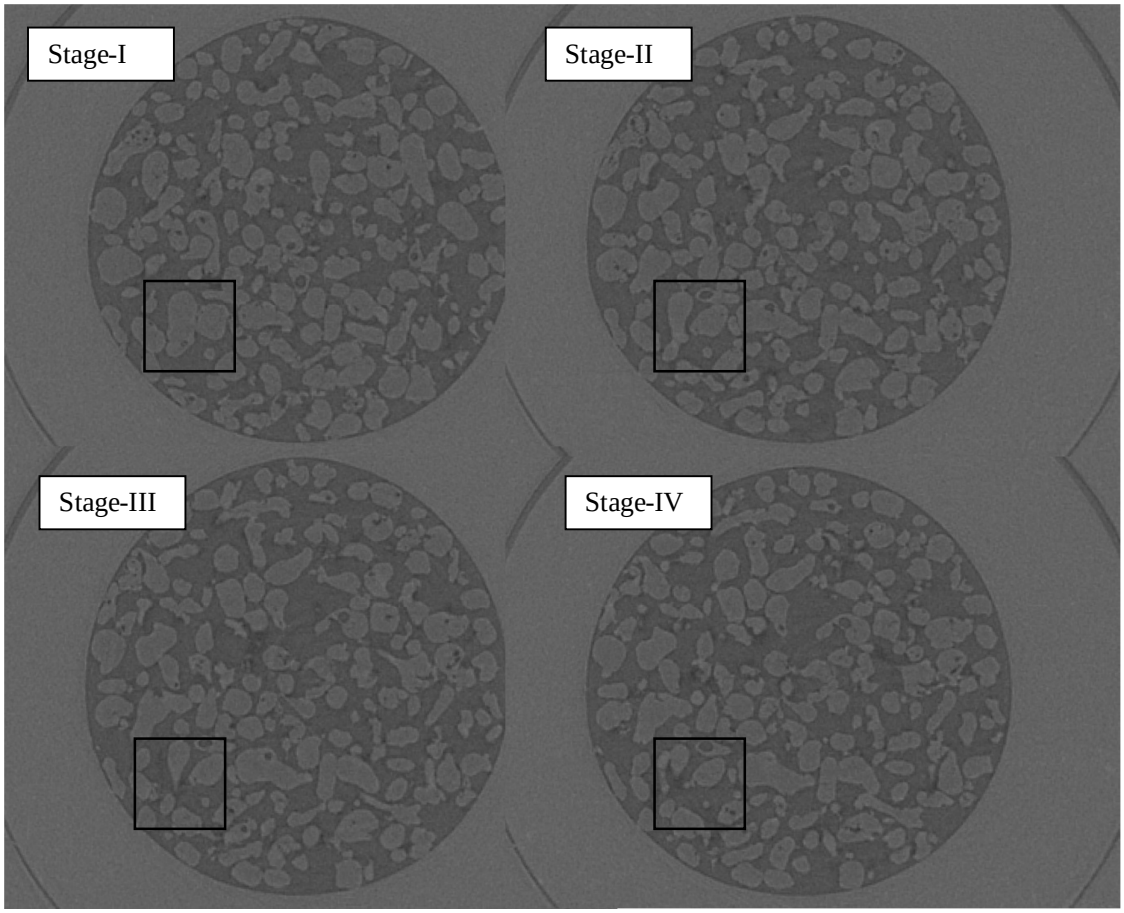

Figure 5.10 Example image showing break down of particles.

The elastic volumetric strain was calculated from $P = K\varepsilon_v$ where K is the bulk modulus of the aluminum powder with a value of 76 GPa (http://en.wikipedia.org/wiki/Aluminium) and P is the mean stress calculated using Equation

5.3 and the value of axial stress is taken from Figures 3.16 and 3.17. Then, ε_v is calculated using $\varepsilon_v = P / K$. It is observed that the elastic volumetric strain has values of 1.22% and .52% at 50% and 12% compaction strains for configurations I and II, respectively. Configuration II exhibited less elastic volumetric strain compared to configuration I since it experienced less stress during compaction (Figures 3.16 and 3.17). However, there is a difference between global volumetric strain and the elastic volumetric strain since there are some voids inside the specimen. One can notice that the values of elastic volumetric strain are very close to the particles volumetric strain values of both configurations. Figures 5.11 and 5.12 show the plots for mean stress versus global volumetric strain for configurations I and II, respectively.

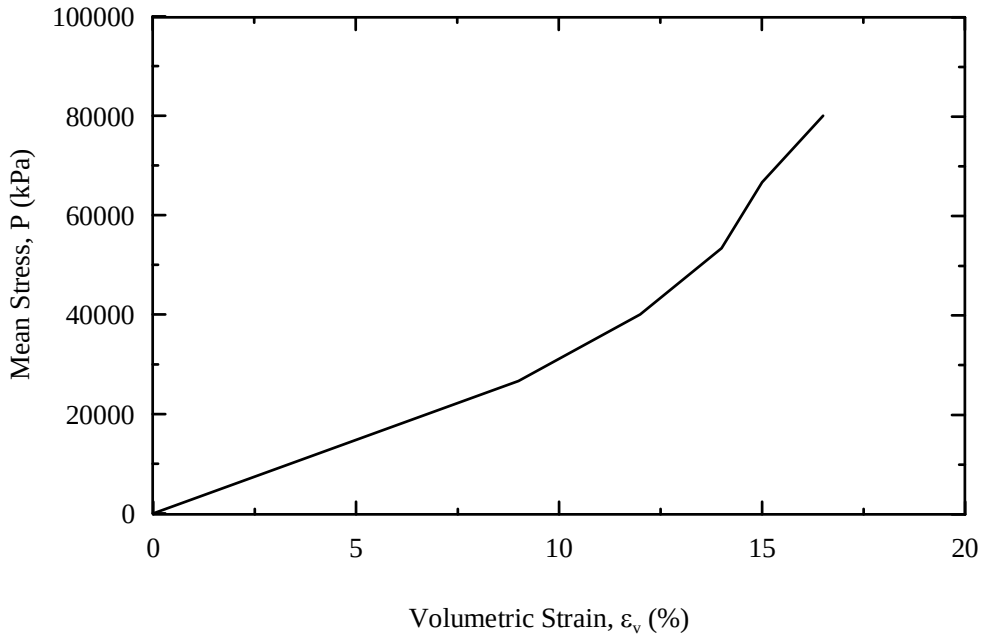

Figure 5.11 Mean stress versus global volumetric strain for configuration I.

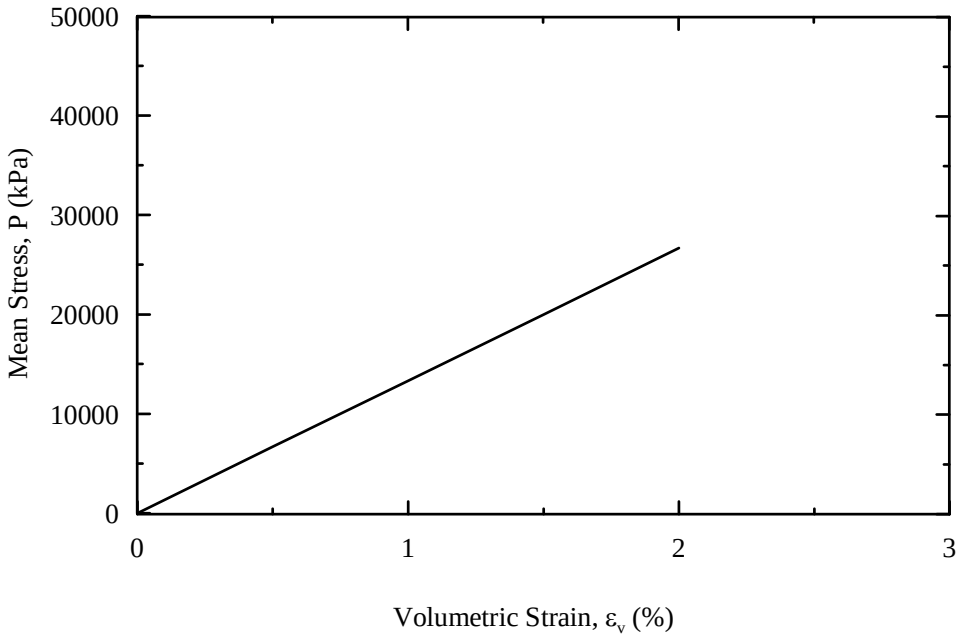

Figure 5.12 Mean stress versus global volumetric strain for configuration II.

5.4 ROTATIONAL BEHAVIOR ANALYSIS

Rotational angles in xy plane and with respect to the z-axis are denoted as κ and λ, respectively (see Figure 3.19). Particles were rotated and translated in both xy plane and with respect to the z-axis with application of an increased compaction strain. Rotational behavior was investigated for the same particles that were identified for volumetric analysis. Figures 5.13 through 5.20 show the rotational behavior analysis for different regions of the two dies.

Figures 5.13 and 5.14 show the rotational behavior of particles in zone I of configuration I. Particles exhibited a similar trend in rotating for both angles. For this region, the particles rotated to an average of 40° with respect to the z-axis during the application of compaction strains; a rotation of about 17° was detected in the xy plane. Initially, there was no major rotation observed up to 10% compaction strain; however, the particles showed a significant rotation when compaction strain reached 20%. The selected particles were not

exactly at the top of the die, but rather their positions were 40 to 50 pixels below the surface. As a result, there was a delay to act with applied compaction. Tables 5.4 and 5.5 list the values of $\Delta\lambda$ and $\Delta\kappa$, for zone I of configuration I respectively.

The rotational characteristic of the particles in zone II of configuration I is depicted in Figures 5.15 and 5.16. Particles from this region exhibited a similar rotational value, since this zone was near the bottom of the die (see Figure 4.6). Particles rotated 25° and 10° with respect to the z-axis and in the xy plane, respectively at the end of compaction process. The particles again exhibited a similar behavior as zone I of small rotation in xy plane compared to the rotation, with respect to the z-axis and insignificant rotation like zone I up to 15% compaction strain for both angles. However, they showed a significant rotation after 20% compaction strain, which is similar to the behavior of particles in zone I. The tracked particles showed the highest and lowest value for $\Delta\lambda$ of 32.55 and 19.65° respectively, whereas the maximum and minimum values for rotation in the xy plane were 14.15° and 9.5°, respectively. The values of changes in both angles are listed in Tables 5.6 and 5.7.

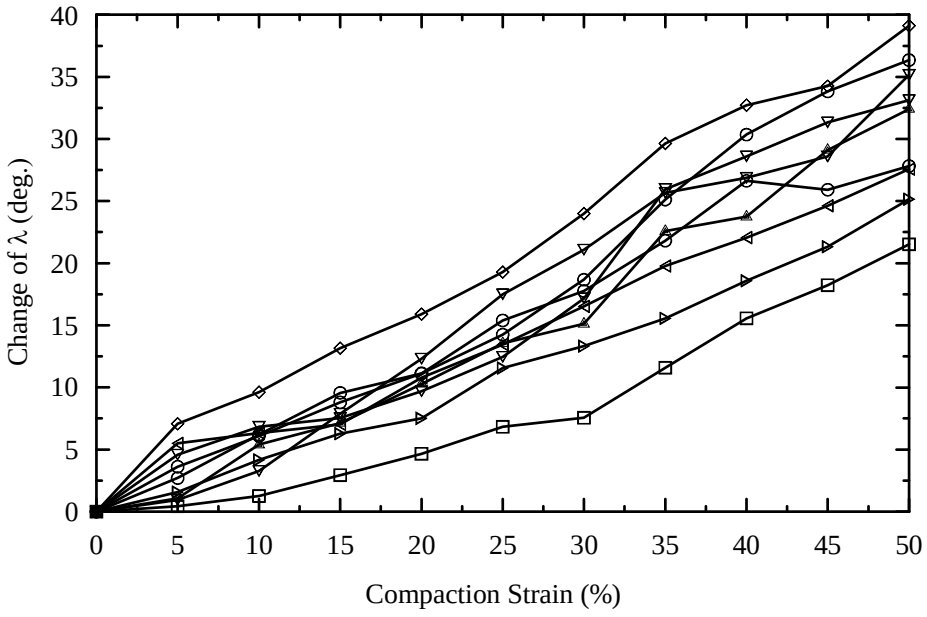

Figure 5.13 Rotational behavior analysis of angle $\Delta\lambda$ in zone I of configuration I.

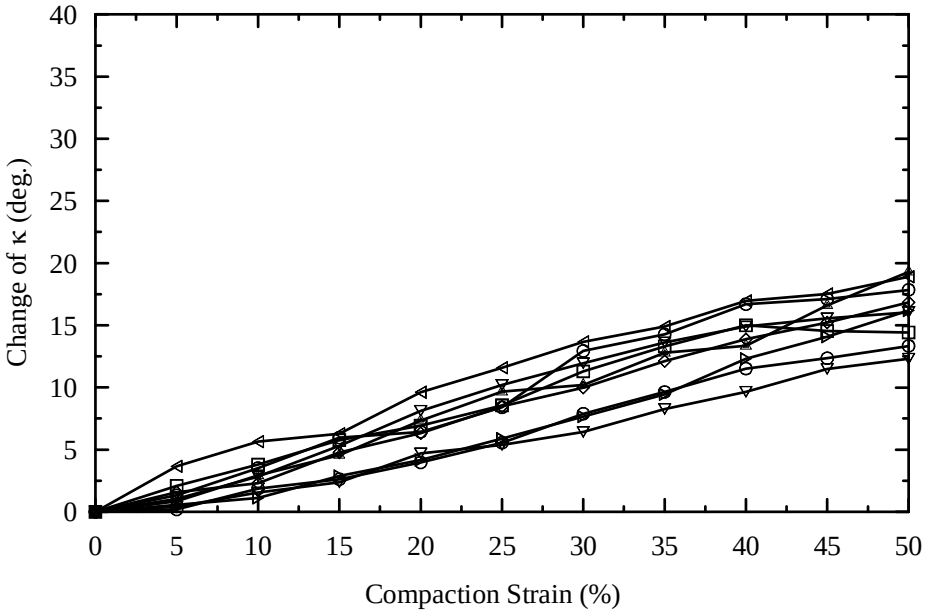

Figure 5.14 Rotational behavior analysis of angle Δκ in zone I of configuration I.

Table 5.4 Values of Δλ for zone I of configuration I.

Compaction Strain (%)	Particle								
	1	2	3	4	5	6	7	8	9
	Δλ (deg.)								
0	0	0	0	0	0	0	0	0	0
5	1.08	2.70	0.95	5.50	1.57	3.62	0.43	7.08	4.58
10	5.39	6.19	3.27	6.33	4.18	6.09	1.25	9.62	6.83
15	7.13	9.56	7.88	7.03	6.28	8.80	2.94	13.17	7.54
20	10.29	11.13	12.32	10.78	7.52	11.12	4.66	15.90	9.69
25	13.56	15.39	17.50	13.45	11.56	14.25	6.83	19.28	12.45
30	15.12	17.76	21.09	16.52	13.32	18.67	7.56	23.99	17.17
35	22.58	21.81	25.67	19.78	15.57	25.12	11.59	29.65	25.97
40	23.75	26.63	26.87	22.07	18.59	30.35	15.57	32.73	28.60
45	29.11	25.91	28.59	24.63	21.33	33.83	18.23	34.25	31.35
50	32.41	27.82	35.15	27.58	25.16	36.35	21.52	39.12	33.14

Table 5.5 Values of Δκ for zone I of configuration I.

Compaction Strain (%)	Particle								
	1	2	3	4	5	6	7	8	9
	Δκ (deg.)								
0	0	0	0	0	0	0	0	0	0
5	0.84	1.33	1.05	3.65	0.57	0.19	2.10	1.57	0.40
10	2.93	3.52	2.84	5.64	1.11	1.87	3.80	2.30	1.56
15	4.56	5.97	5.31	6.28	2.89	2.62	5.76	4.78	2.37
20	7.34	6.43	8.13	9.63	4.18	3.97	6.93	6.33	4.71
25	9.67	8.40	10.19	11.58	5.89	5.56	8.56	8.49	5.38
30	10.21	12.94	11.95	13.67	7.67	7.89	11.29	9.99	6.42
35	12.78	14.27	13.63	14.89	9.45	9.64	13.31	12.11	8.26
40	13.35	16.70	14.89	16.98	12.31	11.52	14.99	13.87	9.64
45	16.61	17.11	15.56	17.53	14.08	12.35	14.53	15.23	11.49
50	19.29	17.85	16.05	18.91	16.19	13.34	14.43	16.85	12.32

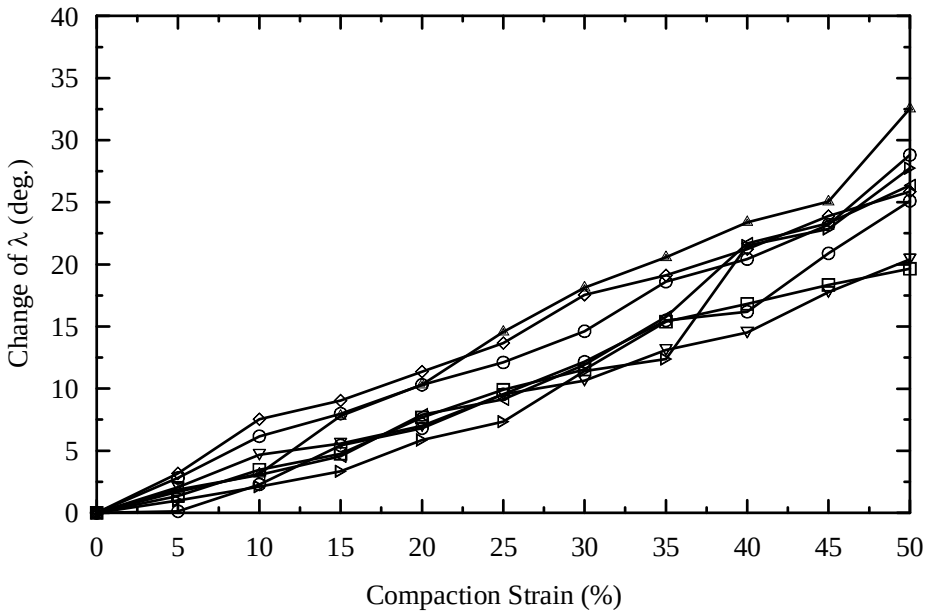

Figure 5.15 Rotational behavior analysis of angle Δλ in zone II of configuration I.

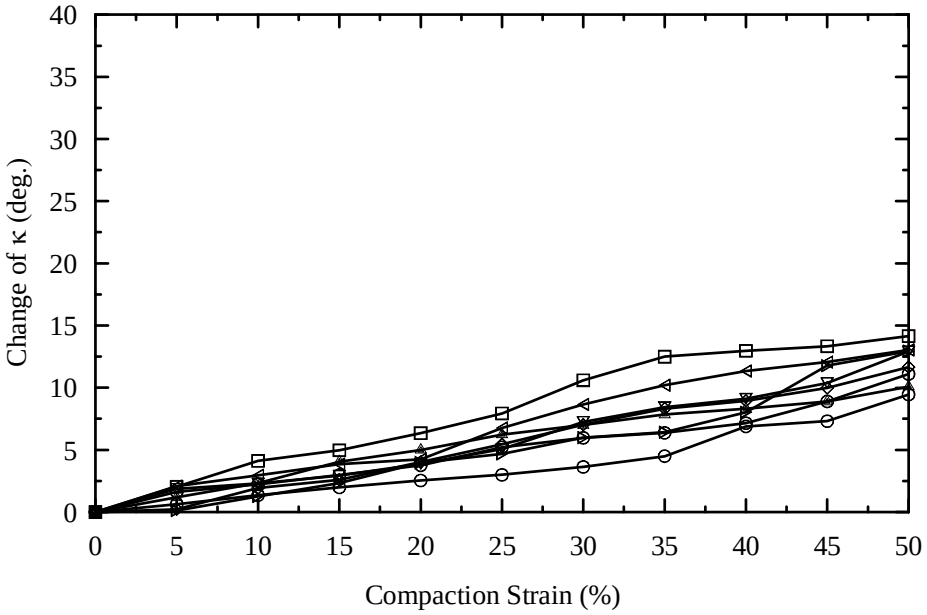

Figure 5.16 Rotational behavior analysis of angle Δκ in zone II of configuration I.

Table 5.6 Values of Δλ for zone II of configuration I.

Compaction Strain (%)	Particle							
	11	12	13	14	15	16	17	18
	Δλ (deg.)							
0	0	0	0	0	0	0	0	0
5	1.69	0.13	2.07	1.87	0.99	2.81	1.35	3.19
10	3.15	2.29	4.68	3.05	2.11	6.17	3.48	7.54
15	7.79	5.43	5.57	4.56	3.35	7.99	4.76	9.05
20	10.32	6.81	6.99	7.91	5.87	10.31	7.69	11.37
25	14.58	9.54	9.54	9.13	7.34	12.11	9.91	13.67
30	18.12	12.16	10.65	11.93	11.42	14.62	11.53	17.56
35	20.56	15.49	13.12	15.76	12.38	18.61	15.39	19.13
40	23.39	16.19	14.51	21.68	21.53	20.43	16.83	21.24
45	25.05	20.89	17.76	23.32	22.85	23.19	18.36	23.89
50	32.55	25.11	20.41	26.36	27.76	28.81	19.65	25.85

Table 5.7 Values of Δκ for zone II of configuration I.

Compaction Strain (%)	Particle							
	11	12	13	14	15	16	17	18
	Δκ (deg.)							
0	0	0	0	0	0	0	0	0
5	1.18	0.63	1.87	2.08	0.11	1.62	2.03	0.23
10	2.32	1.35	2.31	2.95	1.26	2.23	4.11	1.93
15	4.05	1.98	2.92	3.85	2.32	2.98	4.97	2.61
20	4.99	2.54	3.87	4.24	3.99	3.76	6.34	4.01
25	6.23	2.99	5.07	6.76	4.67	5.21	7.93	5.46
30	6.99	3.63	7.24	8.66	5.99	5.97	10.61	7.02
35	7.85	4.50	8.43	10.21	6.41	6.37	12.49	8.32
40	8.31	6.89	9.11	11.35	8.03	7.15	12.97	8.94
45	8.89	7.31	10.37	12.06	11.76	8.90	13.34	9.99
50	10.09	9.45	12.92	13.03	12.95	11.10	14.15	11.67

The rotational behavior of particles for zone I of configuration II is depicted in Figures 5.17 and 5.18. Figure 5.17 shows the change in Δλ of the particles, with respect to the z-axis versus the compaction strain. Particles belonging to this region rotated finally at 15° with respect to the z-axis, showing a maximum and minimum rotational value of 25° and 10°, respectively. The rotational value was low at 3% and 6% compaction strains. However, a significant rotation was observed after 9% compaction strain. Table 5.8 summarizes the results of both Δλ and Δκ for zone I of configuration II.

Figure 5.18 shows the rotational behavior of the particles in the xy plane of zone I for configuration II and the average values of Δλ observed for 3%, 6%, 9%, and 12% compaction strains were 1°, 3.8°, 6°, and 7.4°, respectively. Particles rotated to a maximum 10° and a minimum of 3.5° at 12% compaction strains. Figures 5.17 and 5.18 show that the values of Δκ are much less than the value of Δλ which indicates particle rotated more with respect to the z-axis when compared to the rotation in xy plane for this particular region.

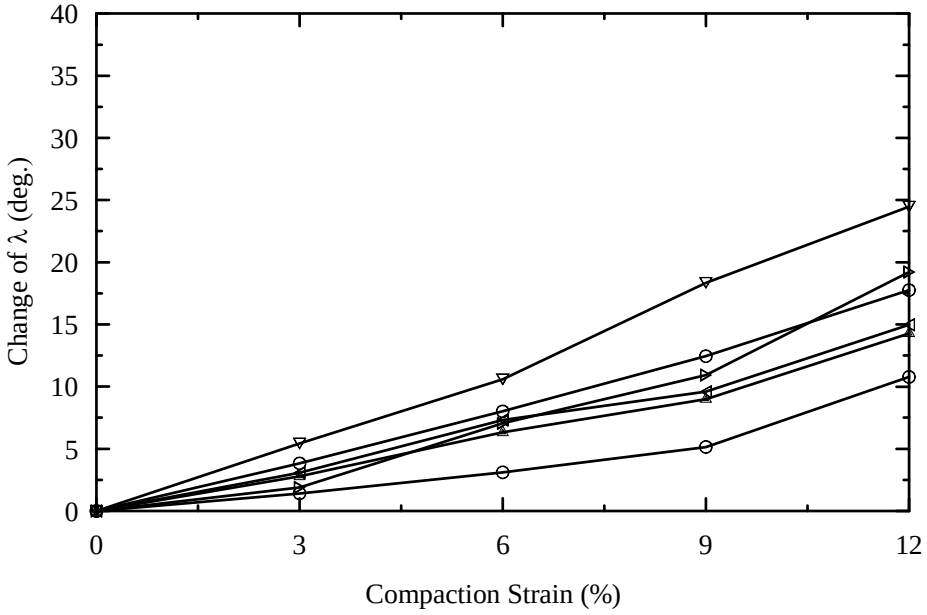

Figure 5.17 Rotational behavior analysis of angle Δλ in zone I of configuration II.

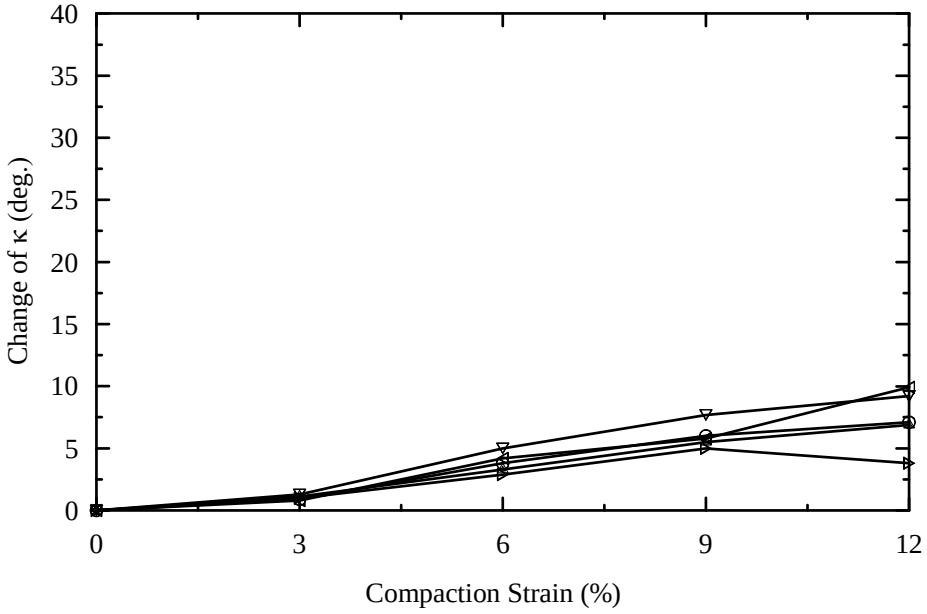

Figure 5.18 Rotational behavior analysis of angle Δκ in zone I of configuration II.

Table 5.8 Values of Δλ and Δκ for zone I of configuration II.

Particle	Compaction Strain (%)				
	0	3	6	9	12
	Δλ (deg.)				
41	0	2.78	6.32	9.01	14.29
42	0	1.42	3.11	5.15	10.78
43	0	5.44	10.58	18.36	24.48
44	0	3.08	7.32	9.59	14.98
45	0	1.89	7.05	10.93	17.76
Δκ (deg.)					
41	0	1.10	3.30	5.50	6.90
42	0	0.90	3.80	6.00	7.10
43	0	1.30	5.00	7.70	9.20
44	0	0.80	4.20	5.80	9.90
45	0	1.00	2.90	5.00	3.80

The rotational behavior of particles in zone II of configuration II is depicted in Figures 5.19 and 5.20. Due to the curved boundary of the die (see Figure 4.7), particles rotated more in zone II compared to zone I. Since there was no support to resist the movement of particles, a significant amount of rotation was recorded. Particle rotation with respect to the z-axis yielded a final average rotation value of 25°. Particles rotated 6°, 11°, 16°, and 22° for compaction strains of 3%, 6%, 9%, and 12%, respectively. The maximum and minimum values of particle rotation with respect to the z-axis was 30.27° and 7.16°, respectively, showing a noticeable change for Δλ after a 6% compaction strain. Table 5.9 lists the values of Δλ and Δκ for zone II of configuration II.

Figure 5.20 shows the rotational behavior of the particles in the xy plane of zone II for configuration I. It is observed that the particles rotated a very small amount in the xy plane. They exhibited a major rotation at 9% compaction strain after an insignificant rotation at the initial condition. The maximum rotation was 11.20° at 12% compaction strain. In spite of the presence of a curved boundary, the value of Δκ is very low, compared to the value of Δκ of zone I, since the particles were far away from the loading plate.

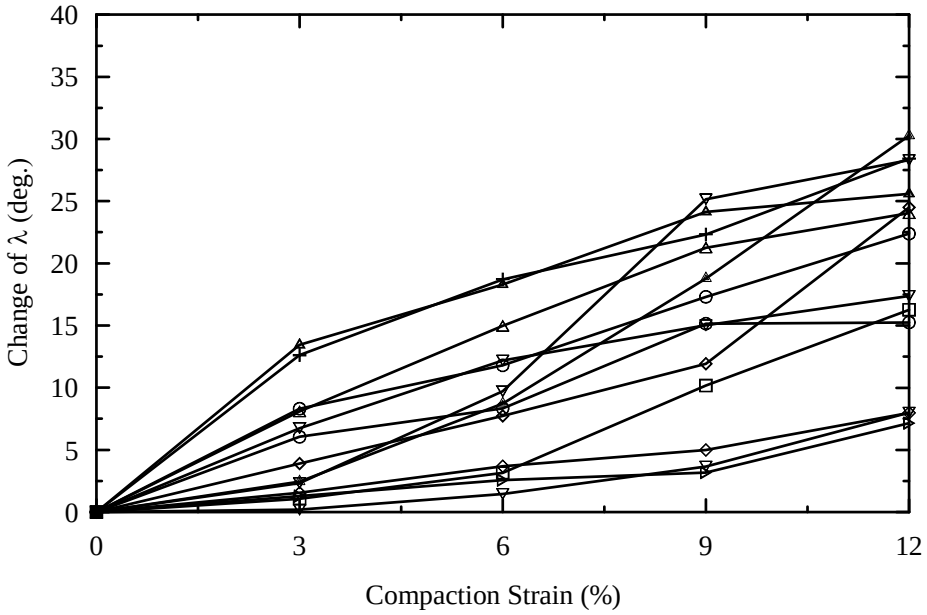

Figure 5.19 Rotational behavior analysis of angle Δλ in zone II of configuration II.

5.4.1 Discussion of Rotational Behavior Analysis

The rotational behavior of two different zones of the two die configurations is presented in Figures 5.21 through 5.24 which show that the values of both Δλ and Δκ are higher for configuration I than configuration II due to higher strains for configuration I (50%). Particles close to the loading plate in zone I, exhibited higher values for both Δλ and Δκ than the denoted angles of zone I. Particles rotated 26° and 32° in zones I and II, respectively with respect to the z-axis at 50% compaction strain. The values for rotation in xy plane were 16° and 11° in zones I and II, respectively. There was a noticeable change in Δλ and Δκ values after 40% compaction strain in zone I, due to a significant change in volume reduction of the particles. This noticeable change was due to the breakdown of particles into small fragments at high compaction strains or difficulties to identify the fragments of particles.

Table 5.9 Values of Δλ and Δκ for zone II of configuration II.

Particle	Compaction Strain (%)				
	0	3	6	9	12
	Δλ (deg.)				
1	0	2.45	8.73	18.80	30.27
2	0	6.04	8.34	15.15	15.25
3	0	6.76	12.18	15.02	17.39
8	0	1.27	2.57	3.17	7.16
10	0	8.31	11.80	17.31	22.39
11	0	1.08	3.14	10.17	16.27
12	0	1.54	3.68	4.99	7.98
13	0	2.33	9.71	25.15	28.31
14	0	0.20	1.45	3.67	8.01
36	0	3.90	7.73	11.93	24.50
37	0	12.62	18.73	22.33	28.42
38	0	8.09	14.99	21.27	24.04
39	0	13.45	18.30	24.14	25.39
Δκ (deg.)					
1	0	1.20	2.70	4.74	4.70
2	0	0.80	2.50	4.20	5.20
3	0	1.00	2.50	3.70	5.00
8	0	1.00	2.90	4.40	5.90
10	0	0.70	2.40	3.80	4.50
11	0	0.70	2.40	3.90	6.50
12	0	0.80	2.90	4.20	8.10
13	0	0.70	1.20	3.30	5.60
14	0	1.10	2.50	3.60	6.60
36	0	0.60	1.60	2.80	11.20
37	0	1.60	1.90	3.00	5.30
38	0	1.40	1.80	2.90	4.50
39	0	0.30	0.60	0.90	0.60

Figures 5.23 and 5.24 show the behavior for both Δλ and Δκ of configuration II. It is apparent that the particles rotated more with respect to the z-axis, in comparison to the rotation in xy plane. They exhibited an average rotation Δλ rotation of 17° and 19° in zones I and II, respectively; whereas the final rotational value of Δκ was 7.5 ° and 6° for the same zones. However, the rotation with respect to the z-axis of the particles was higher in zone II since the particles had no support to resist their movement, due to presence of a curved boundary which caused the particles to rotate even more.

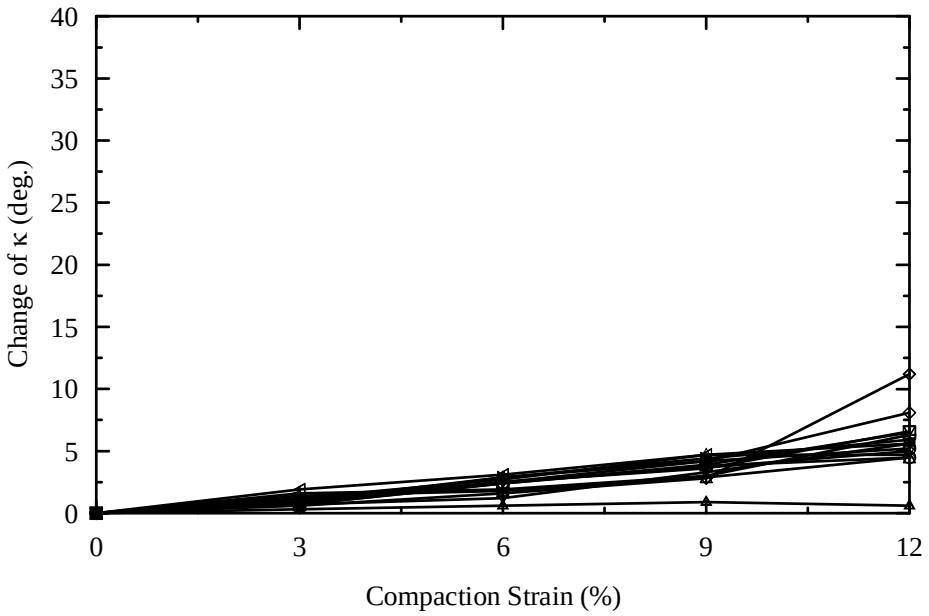

Figure 5.20 Rotational behavior analysis of angle Δκ in zone II of configuration II.

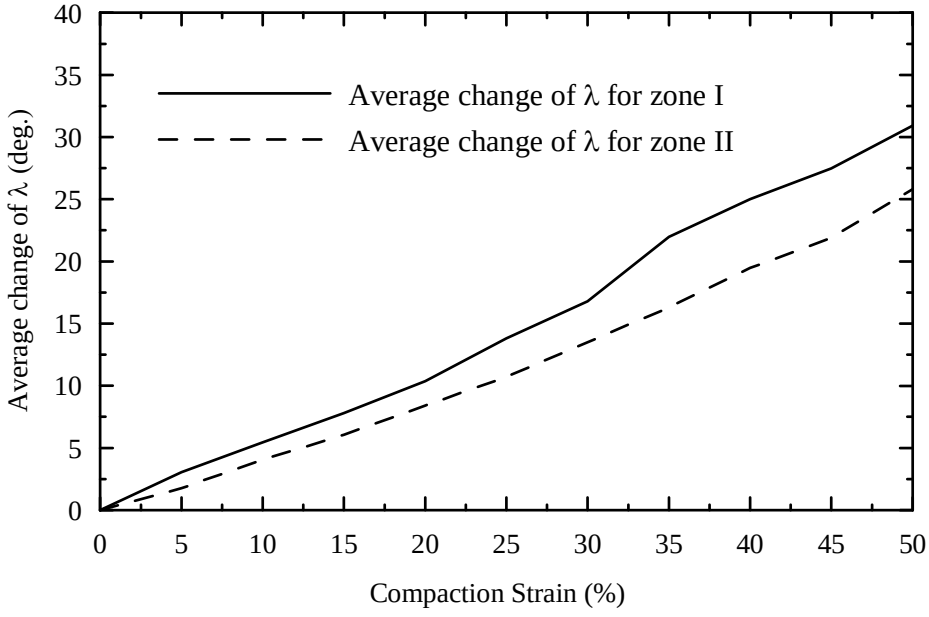

Figure 5.21 Rotational behavior analysis of Δλ of configuration I.

The particles showed a specific trend of rotating in all zones of the two configurations. The value of $\Delta\lambda$ and $\Delta\kappa$ increased simultaneously, as the compaction strains increased. Particles oriented either clockwise or counterclockwise in the xz plane, from an initial condition to the final stage compaction. An illustrative example of the orientation of a group of particle from 0% to 12% is depicted in Figure 5.25.

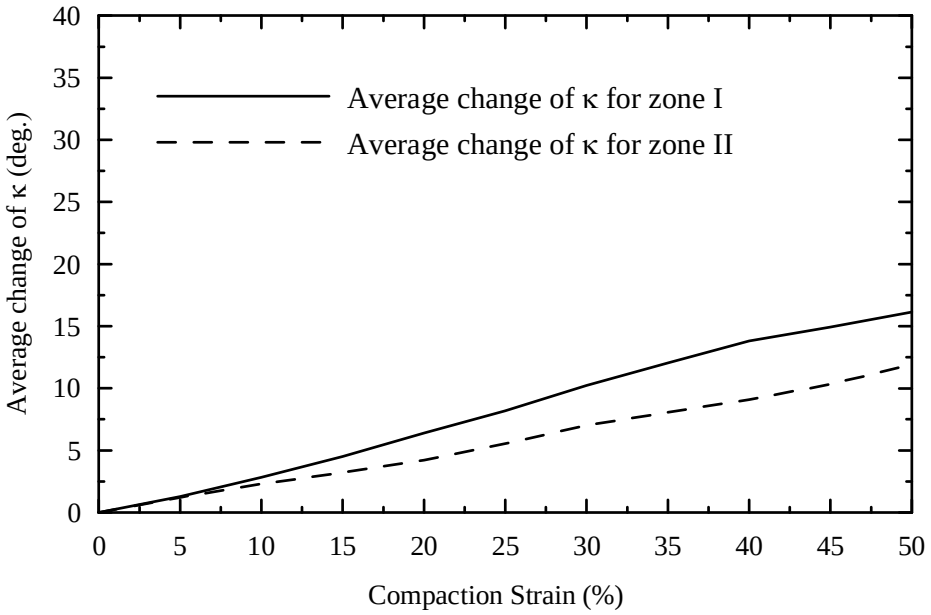

Figure 5.22 Rotational behavior analysis of $\Delta\kappa$ of configuration I.

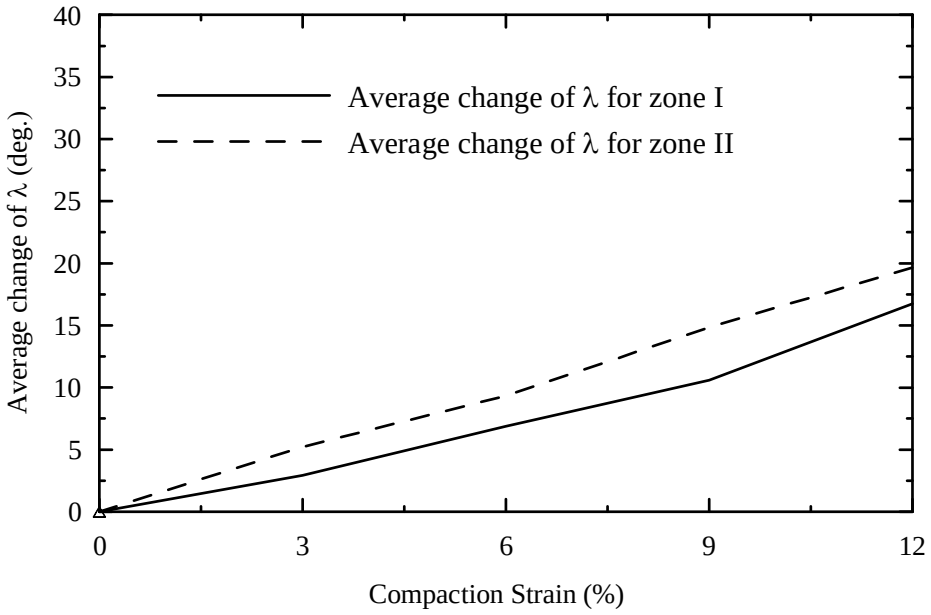

Figure 5.23 Rotational behavior analysis of Δλ of configuration II.

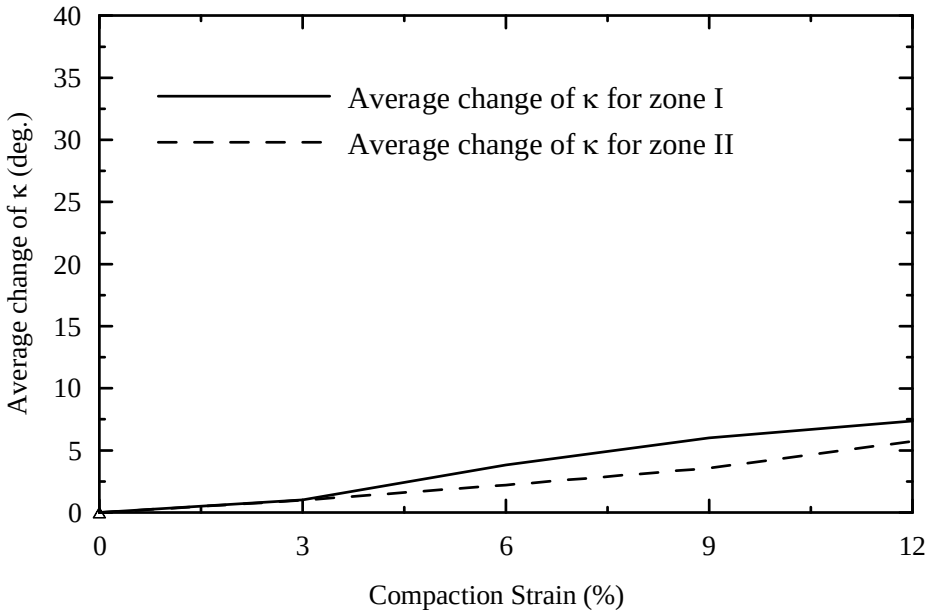

Figure 5.24 Rotational behavior analysis of Δκ of configuration II.

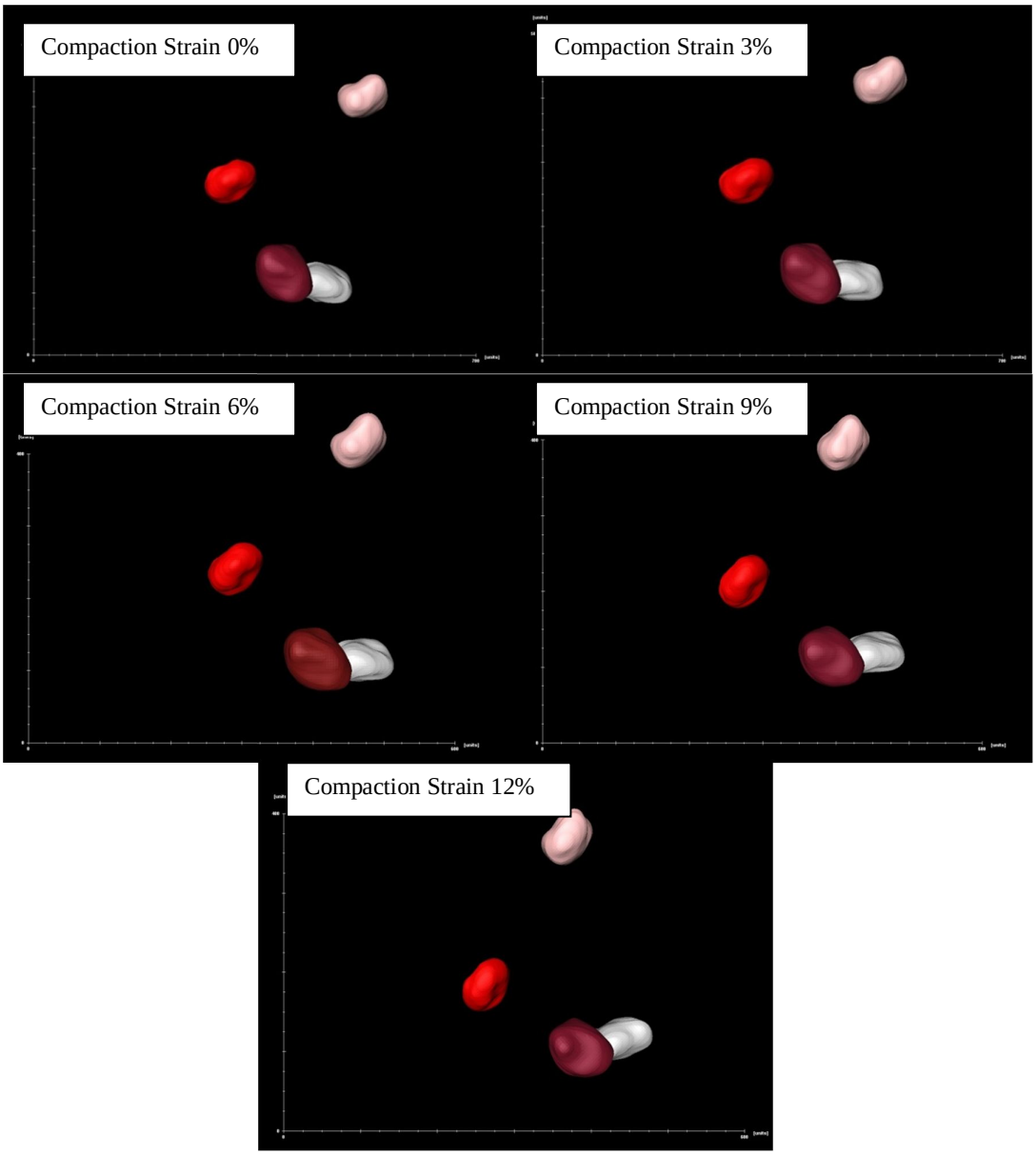

Figure 5.25 Example of orientation of a group of particles under different compaction strains of configuration I.

CHAPTER SIX
SAND-CONE INTERACTION DURING CONE PENETRATION TEST (CPT)

6.1 INTRODUCTION

SMT technology was employed to investigate the behavior of sand during the Cone Penetration Test (CPT). A model CPT test was conducted in the laboratory while acquiring the SMT scans to visualize and quantify the sand particle position. AVIZO visualization software was used for the analysis. This Chapter summarizes specimen preparation procedure, CPT scans analysis, and the results.

6.2 EXPERIMENTAL WORK

6.2.1 Specimen Description

Particles size between sieves #40 (0.42 mm) and #50 (0.3 mm) of F-75 sand was used in the experiment. It is a natural silica sand with rounded to sub-rounded particles. The sand was rinsed with distilled water after sieving and was dried in preparation for testing. Few glass beads were placed within sand mix to serve as a tracer to track particles. The penetration test was conducted on a cylindrical specimen contained inside an acrylic tube with an inner diameter of 8.9 mm and a height of 52 mm (see Figure 6.1). The specimen was prepared and placed inside the test cell (Figure 6.2). The cone was advanced into the sand at a rate of 0.5 mm/minute using a stepper motor.

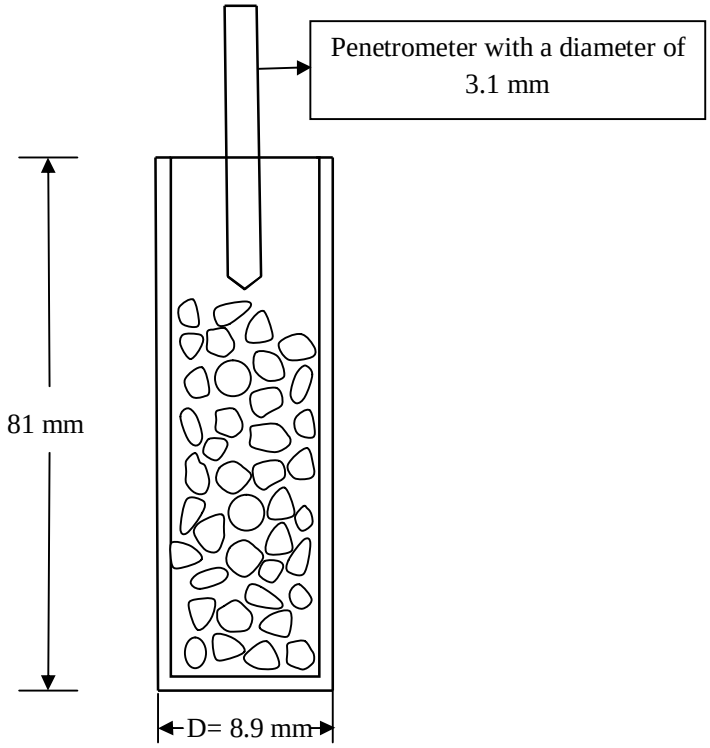

Figure 6.1 Geometric configuration of the specimen.

6.2.2 SMT Scanning

SMT scans of CPT were conducted on April 20, 2011 at Argonne National Laboratory, Chicago using beam-13D of GSECARS sector. Nine sets of scans were acquired at progressing penetration depths. The scans were acquired as an “unbinned” format in order to achieve a high resolution. They correspond to 2 mm penetration intervals from 0 mm to 12 mm of penetration depth. The last two scans were acquired at 17 and 22 mm penetration depths. The scans have a spatial resolution of 8.11 μm/ pixel. Table 6.1 represents a summary of the scans and Figure 6.3 shows the load versus penetration depth of the experiment.

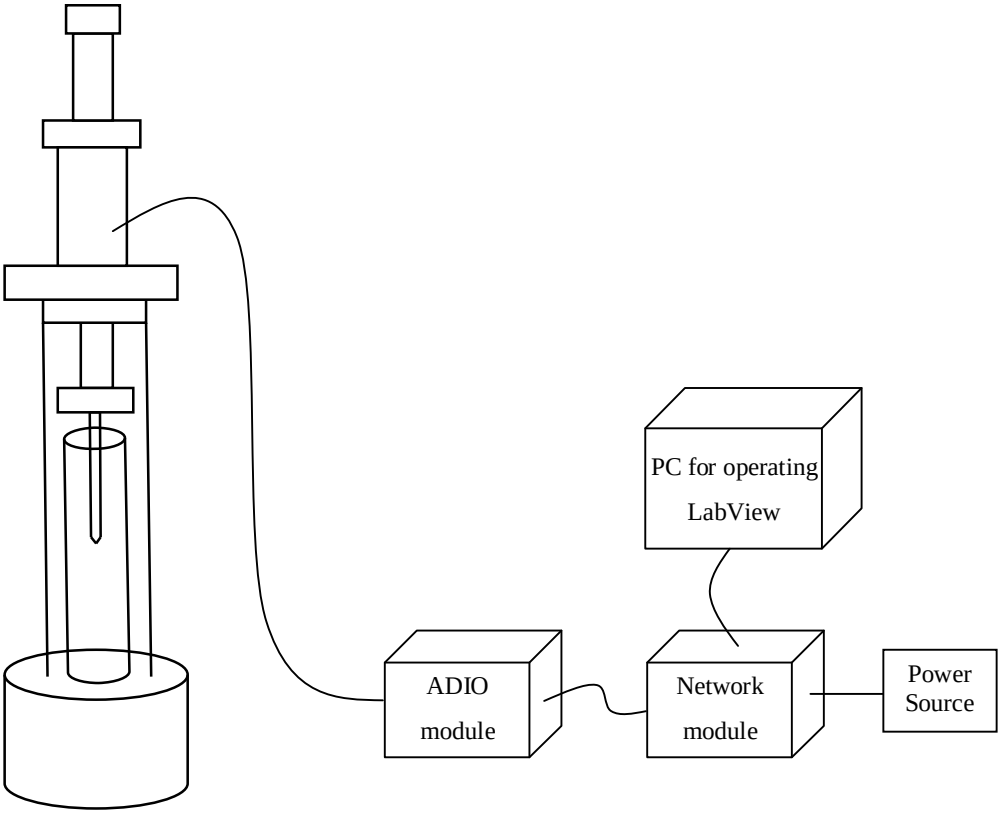

Figure 6.2 Schematic diagram of the experimental setup.

6.2.3 Scans Processing

The scans were saved as "*recon.volume"* format. The initial steps of scans processing were described in Figure 4.1. It contains some overlapping portions and Section 4.3 described the process of removing and stitching the slices. The slices were combined only in the xz plane. IDL software was used to compile the slices. Figure 6.4 shows an example of an axial slice. The AVIZO visualization software was used for tracking few sand particles. The procedure for tracking particles was described in Section 4.4. Glass beads of a size 0.15-0.25 mm were used as a tracer (Figure 6.4). Figure 6.5 depicts an example of tracked particles under two different penetration depths.

Table 6.1 Summary of scans for Cone Penetration Test.

Specimen Dimension (mm)	Mass of Soil (g)	Mass of Glass Bead (g)	Scanning Energy (kev)	Resolution (μm/pixel)	Cone Penetration Depth at scan (mm)
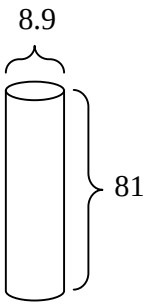	4.63	.06	33.08	8.11	0
					2
					4
					6
					8
					10
					12
					17
					22

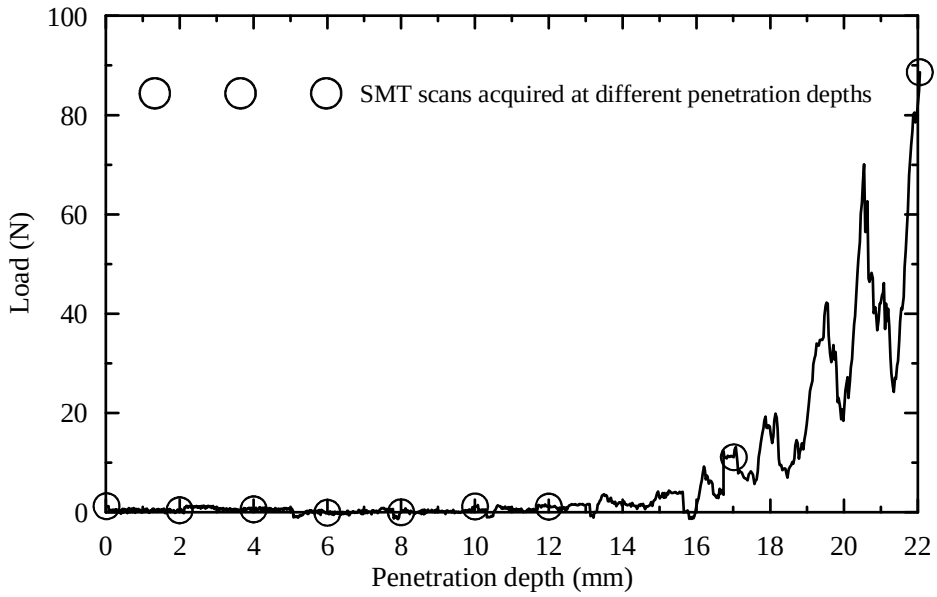

Figure 6.3 Load penetration curve during CPT.

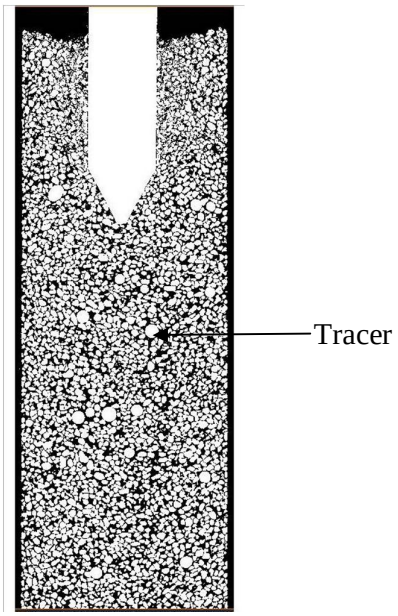

Figure 6.4 Example axial SMT image of CPT.

6.3 RESULTS

The tracked particles were evaluated in the x (lateral) and z (axial) directions for their movement analysis. The scanned image was divided into three zones denoted as zones I, II, and III. The three zones were differentiated according to their depth as shown in Figure 6.6. A total of 30 particles were identified and tracked (Table 6.2). Figure 6.5 shows the tracked particles for 0 and 2 mm penetration depths and the images of the subsequent penetration depths are listed in Appendix B.

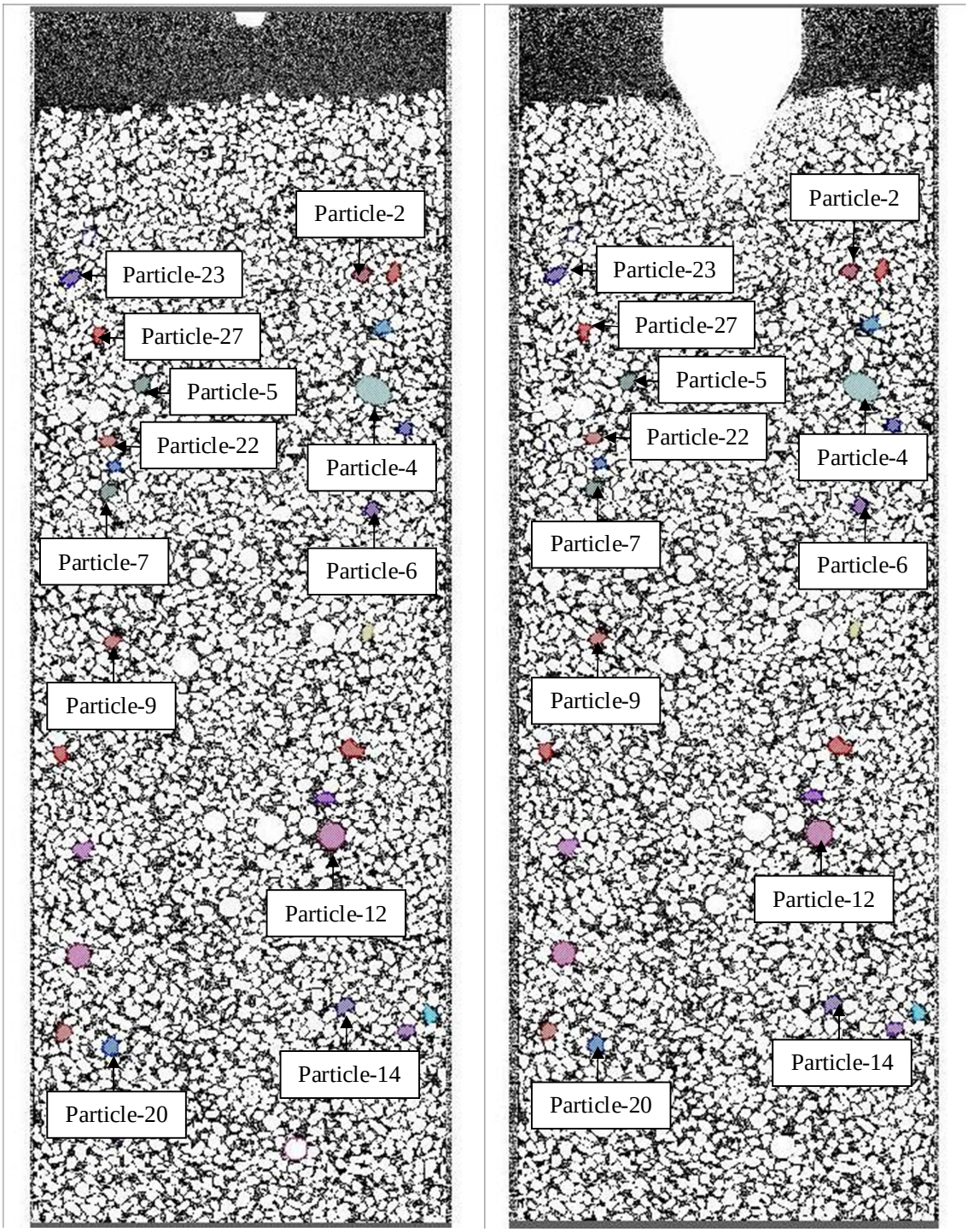

Figure 6.5 Example of same particles tracked under different penetration depths (not all the tracked particles are labeled).

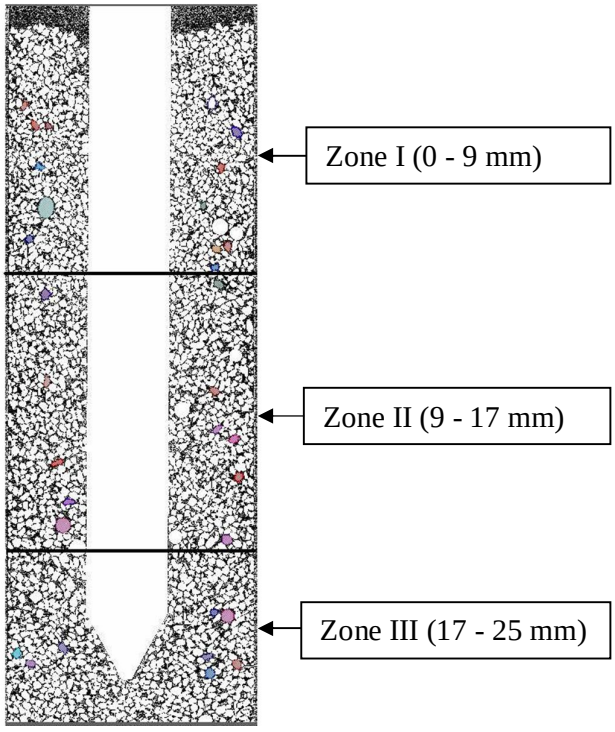

Figure 6.6 Different zones used for movement analysis in CPT.

Table 6.2 Number of particles identified and tracked in different zones of the specimen.

Zones	# of tracked particles
I	12
II	9
III	9
Total = 30 particles	

6.3.1 Movement in the Vertical Direction (z-axis)

- **Zone I**

Figure 6.7 depicts the particles movement in the z-axis versus the penetration depth for zone I. All particles of zone I showed a similar trend during the penetration. They exhibited no movement during the first 4 mm penetration, followed by an upward movement up to 17 mm penetration and a downward movement after that. The upward movement was due to the small overburden pressure at the top of the specimen. With continuous cone advancement, a down-drag of particles caused the particles to move downward.

- **Zone II**

The movement of particles in zone II versus the penetration depth is depicted in Figure 6.8. Since the particles were positioned 9 mm below the top of the specimen, sand particles did not move until the cone reached 12 mm penetration. Then the particles began to move downward along with the cone. The particles showed no upward movement due to the increased overburden pressure. They showed an average movement percentage of 4.22% and 5.50% at 17 mm and 22 mm penetration depths, respectively.

- **Zone III**

Figure 6.9 shows the percentage of movement in the z-axis versus the penetration depth for zone III, where the particles showed a similar trend as zone II. Zone III represents a depth 17 to 25 mm (see Figure 6.6) and the behavior of particles is similar to zone II. A final average value of 4.7% and 9.06% was observed at 17 and 22 mm penetration depths, respectively. The downward movement of the particles increased as the cone advanced further into the soil as shown in Figures 6.8 and 6.9.

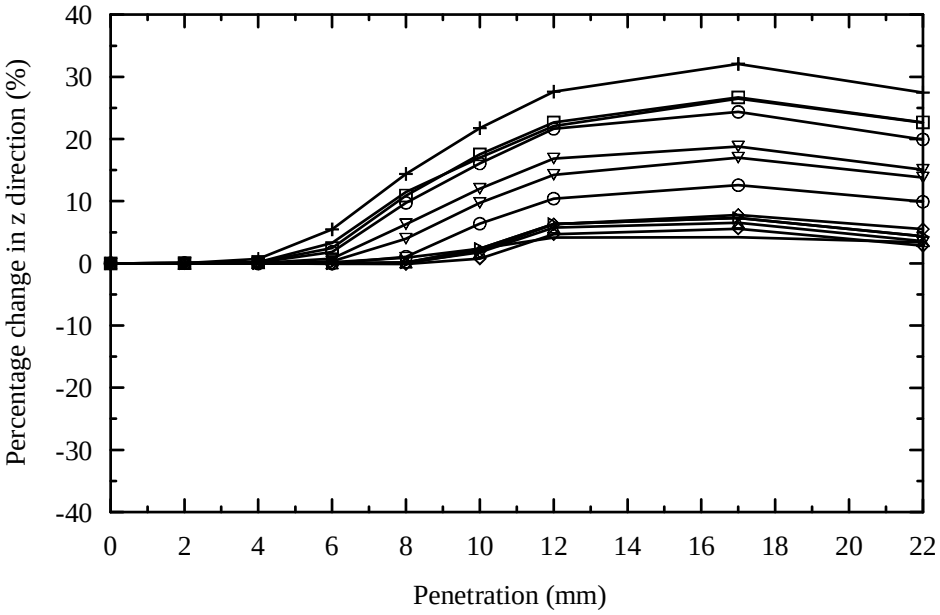

Figure 6.7 Percentage change in the z-direction for zone I.

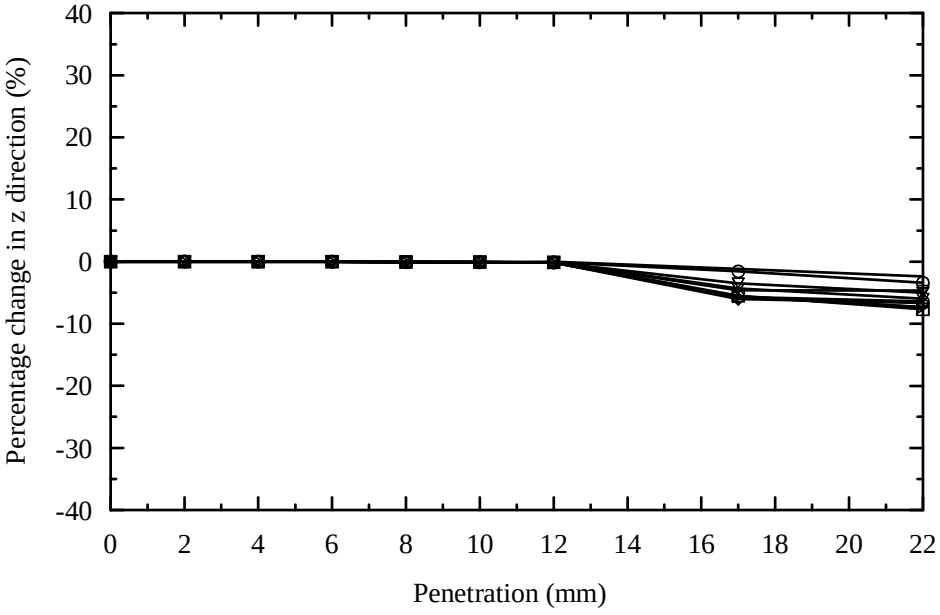

Figure 6.8 Percentage change in the z-direction for zone II.

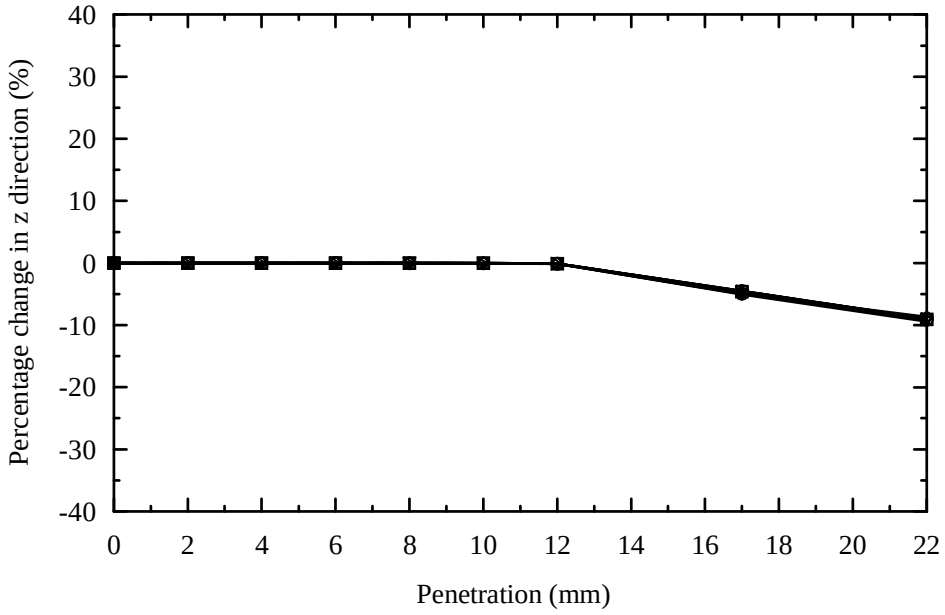

Figure 6.9 Percentage change in the z-direction for zone III.

6.3.2 Movement in the Lateral Direction (x-axis)

The penetration depth of the cone versus the percentage of movement in the x-direction is depicted in Figures 6.10 through 6.12. The percentage of movement in the lateral direction means whether the particle approaches the cone or moving away from the cone. Figures 6.10 through 6.12 show that the particles move away from the cone to make room for the advancing cone in most cases.

- **Zone I**

Figure 6.10 shows that the particles moved 8% at the end of the experiment in zone I. Particles showed a significant movement when the cone approached them. This zone was near the top of the specimen and there was room for the particles to move upward. Therefore, particles of zone I showed more movement than zones II and III.

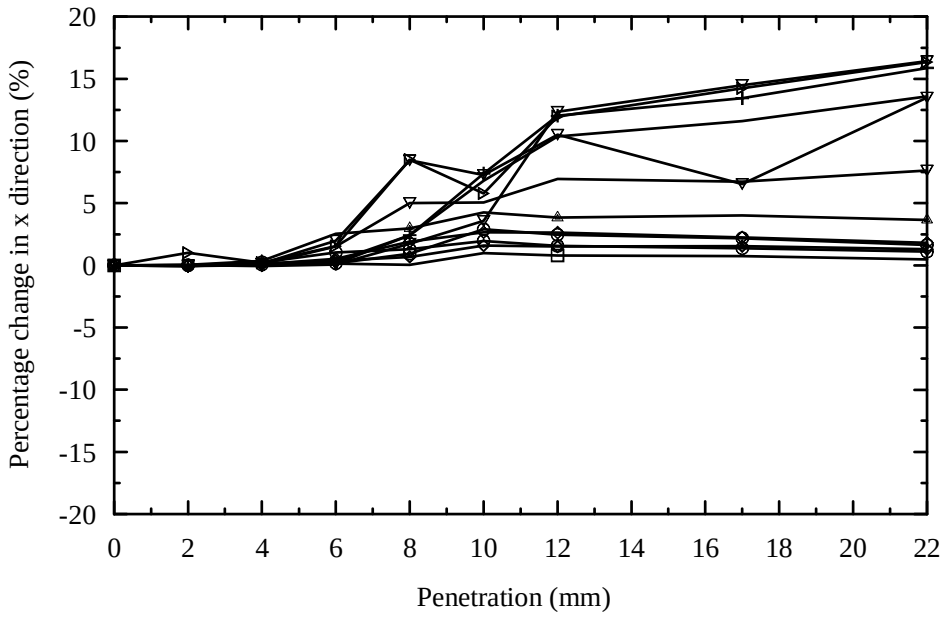

Figure 6.10 Percentage change in the x-direction for zone I.

- **Zones II and III**

The movement of the particles of zone II in the x-direction (Figures 6.11) is similar to the trend in the z-direction. There was no movement up to 12 mm penetration as the cone did not reach the particles yet. Particles began to move away from the cone when it was penetrating from 12 mm to 22 mm. Figure 6.12 shows the percentage of change in movement for x-direction versus the penetration depth of the cone for zone III where the particles showed a small movement compared to zones I and II. The movement of the particles was insignificant since there was no space for the particles to move at the bottom of the specimen like zone I.

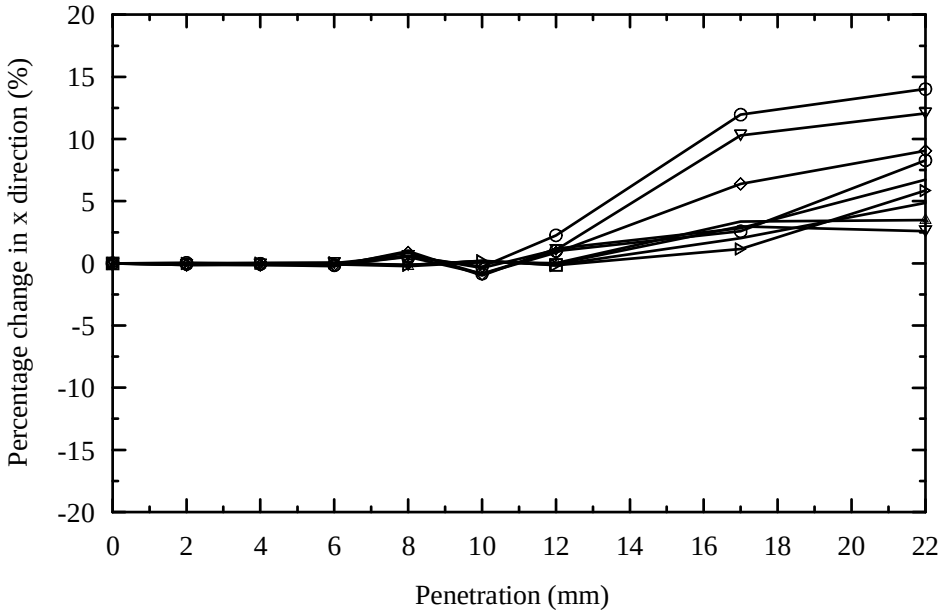

Figure 6.11 Percentage change in the x-direction for zone II.

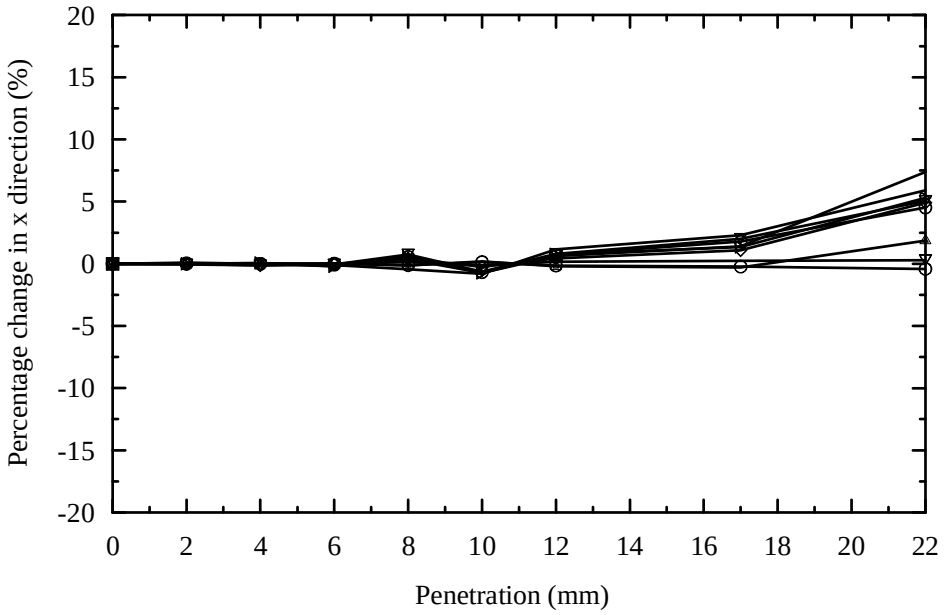

Figure 6.12 Percentage change in the x-direction for zone III.

6. 4 DISCUSSIONS

A total of 30 particles were identified, tracked, and analyzed in this part of the research. The behavior of particles varied in different zones due to their position in the specimen. The movement of particles in zone I was more significant when compared to zones II and III, due to the initial overburden pressure. Particles within zones II and III showed no upward movement but rather downward movement due to an increased overburden pressure, as well as a down-drag which forced the particles to move downward. Particles within zones II and III began to move later since it requires more time for the cone to reach them. The lateral movement of the particles (x-direction) is mainly due to making room for the cone as it advanced towards them.

The average percentage movement in the z (axial) and x (lateral) directions for all zones versus the penetration depth is presented in Figures 6.13 and 6.14. The final average value of movement in the x-direction for zones I, II, and III were 8%, 7.43%, and 3.8%, respectively, whereas in the z-direction, the values were 12.6% (upward), 5.5% (downward), and 9% (downward), respectively.

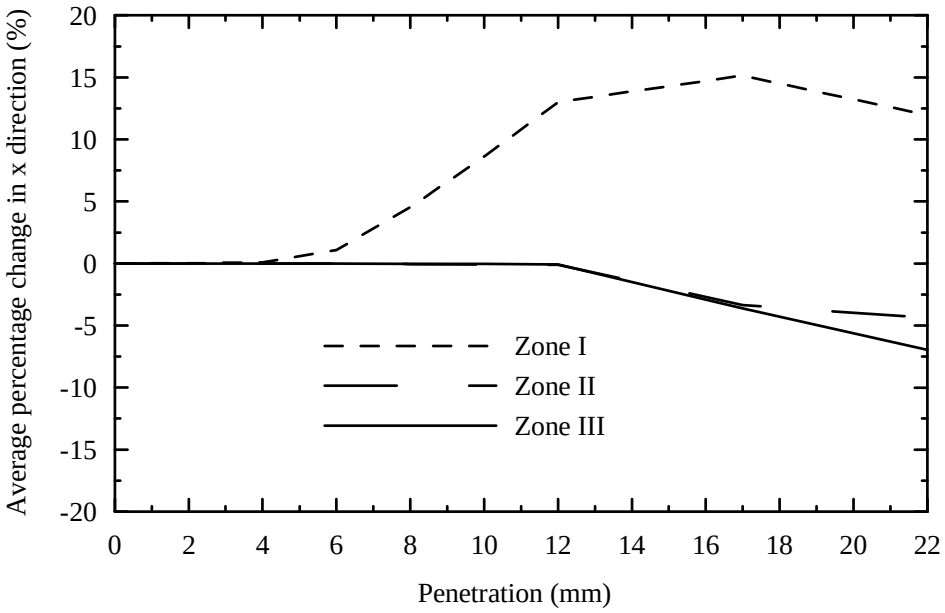

Figure 6.13 Average percentage change in the z-direction for all zones.

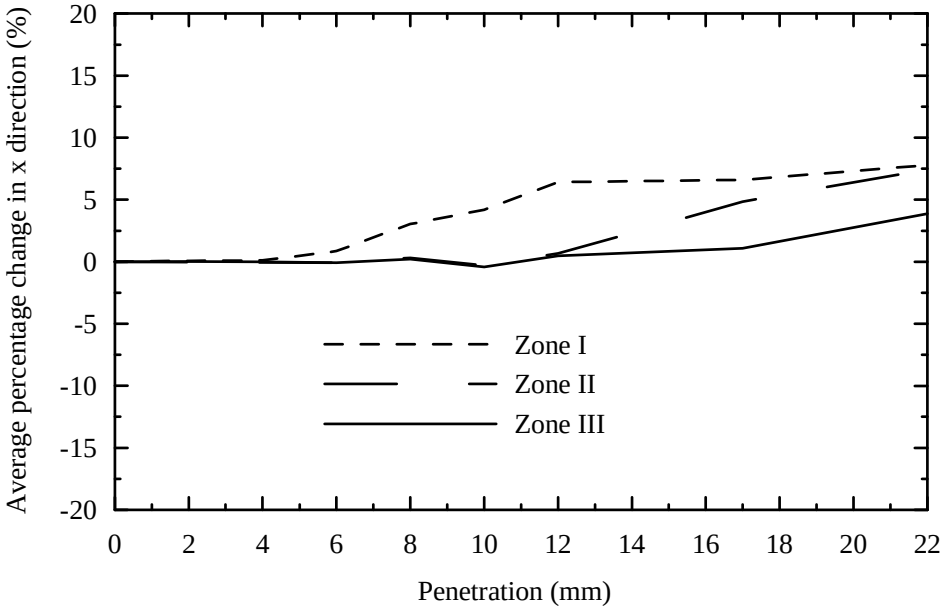

Figure 6.14 Average percentage change in the x-direction for all zones.

CHAPTER SEVEN
SUMMARY, CONCLUSIONS AND RECOMMENDATIONS

7.1 SUMMARY AND CONCLUSIONS

The thesis has two objectives, with the first to investigate the rotational behavior of powder during compaction. Two die configurations were scanned at different compaction strain levels to achieve the first objective. The state of the art SMT system was used to acquire the scans. The scans were analyzed using AVIZO software to quantify the volumetric compressibility and rotational behavior. The second objective of this thesis focused on quantifying the position of the particles under different penetration depths. A Cone Penetration Test (CPT) was conducted on a small specimen and scans were collected at various penetration depths.

The following conclusions are drawn from the thesis:

1. Synchrotron Microtomography (SMT) is an excellent tool for analyzing the volumetric compressibility and rotational behavior of powders.

2. The volumetric analyses of the powder after generating the 3D shape by AVIZO showed that the volumetric strain of the particles decreased by 2.5% and 4% at two configurations. Initially, there was no volumetric strain; however, some particles broke down into small fragments at high compaction strains, and it was difficult to identify that small pieces. As a result, volumetric strain was observed at high compaction strains. Some gases were entrapped into the powder during the manufacturing process, which created void cavities inside the powder, thus assisting in particle breakage at high compaction strains. The elastic volumetric strain behavior of the aluminum powder is another factor which contributes to the change in volumetric strain of the particles. However, the value of the particles volumetric strain

was less for configuration II, since it experienced relatively low compaction strain compared to configuration I.

3. The analyses showed that particles near the loading area and curved boundary displayed more rotation. Most particles showed no significant rotation at the early stage of applying compaction, but exhibited more rotation at a higher compaction strain.

4. Sand particles at the top of the specimen showed an upward movement in the z-direction at the beginning of penetration, due to a small overburden pressure. However, particles at the middle and the bottom parts of the specimen showed no upward movement, but rather a downward movement.

5. The scans showed that particles move laterally to make room for the advancing cone. An average 6% movement was observed in the x-direction.

7.2 RECOMMENDATIONS

The followings are recommended for future work:

1. The data presented from the powder analysis for a rotational angle may be compared with the values obtained from numerical models, such as the discrete element method (DEM). An algorithm may also be developed for tracking the same particle automatically.

2. The image analysis is highly dependent on the resolution of the scans. For example, it was very difficult to track small broken pieces of the particles at higher compaction strains for powder analysis. Therefore, searching for other scanning techniques which are capable of generating scans with a resolution down to nano-scale is desirable. Moreover, this technique offers quantification of nano-size structures together with a visualization technique (Jinnai, 2007).

3. The analysis of CPT should be simulated using a numerical model to verify the result, as well as to obtain additional measurements such as surface area, volume, size, etc.

REFERENCES

Alramahi, B. A. (2004). "Assessment of Shearing Phenomenon and Porosity of Porous Media Using Microfocus Computed Tomography." MS Thesis, Louisiana State University, Baton Rouge, LA.

Alshibli, K. A., Okeil, M. A., & Alrahmani, B. (2008). "Update of Correlations between Cone Penetration and Boring Log data". Baton Rouge: LTRC.

Aluminum Powder Metallurgy. (2011). "http://www.aluminum.org/Content/NavigationMenu/TheIndustry/PowderandPaste/PowderMetallurgy.PDF".

Anandrajah, A. (2004). "Sliding and rolling constitutive theory for granular materials." *Journal of Engineering Mechanics*, 130(6), 665-680.

Brown, R. L., and Richards, J.C. (1961). "Profile of granules through apertures."*Trans, Instn. Chem. Engrs., 38, 243-256*.

Brown, R. L., and Richards, J.C. (1970). *Principles of Powder Mechanics*, 1st ed., Pergamon Press, Hungary.

Carlton, R. R., and Adler, A.M. (2006). *Principles of Radiographic Imaging*, 4th ed., Thomson Delmar Learning, Canada.

Chtourou, H., Guillot, M., Gakwaya, A., and Guillot, M. (2002). "Modeling of the metal powder compaction process using the cap model. Part I: Experimental material characterization and validation." *International Journal of Solids and Structures*, 39(4), 1059–1075.

Coulomb, C. (1776). "Essai sur an application des regles des maxims et minimus a quelques problems de statique retfis a i'architecture." Memoires de Savants Etrangers de I Academie des Science de Paris.

Cutress, J. O., and Pulfer. R. F. (1967). "X-ray Investigation of Flowing Powders." *Powder Technology*, 1(4), 213-220.

Dawes, J. G. (1952). "Dispersion of dust deposits by blasts of air." Safety in Mines Res. Estab., Res. Rep. 36, Sheffield.

Hughes, C. V., and Neel, S. T. (2000). “Basics of Computed Tomography.” The American Society for Nondestructive Testing.

ImagiX CT High Resolution System. (2011). “http://www.xviewct.com/industrial-ct-systems/imagix-computed-tomography-system”.

Farley, R., and Valentin, F. H. H. (1968). “Effects of Particle Size upon the Strength of Powders.” *Powder Technology*, 1(6), 344-354.

Gardiner, G. C. (1962). “Limiting conditions for flow of a cohesive granular material down an inclined plane (chute) or between parallel inclined walls (bin or channel).”*Chem. Engng. Sci.*, 17, 1079-1086.

Geniev, G. A. (1958). “Problems of the dynamics of a granular medium.” Acad building architect. USSR cent. Aci. Investing. Inst. Build. Construction, Scientific Communic.

Gokee, A., and Findik, F. (2008). “Mechanical and Physical Properties of Sintered Aluminum Powders.” *AMME Journal*, 30(2), 157-164.

Hagen, G. (1852). “Druck und bewegung des trockenen sandes.” *Berliner Monats-berichte akad. D. Wiss.*, s35-s42.

Hasan, A. (2009). “Micro characterization of deformations in granular materials during shear.” Ph. D. Dissertation, Louisiana State University, Baton Rouge, LA.

Ibukuro, K., Charnsangavez, C., Cinqualbre, A. B., Herron, D. H., and Wallace, S. (1995). “Helical CT angiography with Multiplanar Reformation: Techniques and Clinical Applications.” *RadioGraphics*, 15, 671-682.

Jenike, A. W. (1961). “Gravity flow of bulk solids.” Utah Engng. Expt. Stn., 52, 29-33.

Kamm, R., Steinberg, M. A., and Wulff, J. (1949). “Lead-Grid Study of Metal Powder Compaction.” *Trans. Am. Inst. Mining Met. Eng*., 694–706.

Kong, C.M., and Lannutti, J. J. (2000). “Localised densification during the compaction of alumina granules: the stage I–II transition.” *J. Am. Ceram. Soc*., 83, 685–690.

Kuhn, M. R. (2002). “Particle rotations in granular materials.” *15th ASCE Engineering Mechanics Conference*, Columbia University, New York, USA.

Mahesh, M. (2002). "The AAPM/RSNA physics tutorial for residents." *RadioGraphics*, 22, 949-962.

Manke, I. (2011). "http://www.helmholtz-berlin.de/forschung/funkma/werkstoffe/methoden/x-tomo/index_en.html".

Matkin, D. T., Munho, W., and Valentine, T. M. (1973). "Some factors affecting the reactive hot-pressing behavior of alumina." *Journal of Materials Science*, 8, 1625-1632.

Mori, Y., Sato, M., and Osakada, K. (1999). "Prediction of fracture generated by elastic recoveries of tools, in multi-level powder compaction using finite element simulation." *Int. J. Machine Tools Manuf.*, 39, 1031–1045.

Oda, M., and Iwashita, K. (1999). *An Introduction Mechanics of Granular Materials*, A.A Balkema Publishers, Rotterdam, Netherlands.

Oh, W., and Lindquist, W. (1999). "Image thresholding by indicator kriging." *Transactions on Pattern Analysis and Machine Intelligence, IEEE*, 21(7).

Olinek, J., Anand, C., and Beliehumeur, C. T. (2004). "Experimental Study on the Flow and Deposition of Powder Particles in Rotational Molding." Wiley Interscience (www.interscience.wiley.com).

Rankine, W. J. W. (1857). "On the stability of loose earth." Phil. *Trans. Roy. Soc. Lond*., 147, 9-27.

Razavi, M., Muhunthan, B., and Hattamleh, O. (2007). "Representative Elementary Volume Analysis of Sands Using X-Ray Computed Tomography." *Geotechnical Testing Journal*, 30(3), 212–219.

Reed, J. S. (1988). *Introduction to the Principles of Ceramic Processing*, 1st ed., Wiley, New York.

Reisner, W. (1968). "The behavior of granular materials in flow out of hoppers." *Powder Technology*, 1(5), 257-264.

Resource Center, NDT. (2011). http://www.ndt-ed.org.

Reynolds, O. (1885). "On the dilatancy of media composed of rigid particles in contact: with experimental illustrations." *Phil. Mag*., 5(20), 469-481.

Rydberg, J., Buckwalter, K. A., Caldemeyer, K. S., Alsen, A. M., Kopecky, K. K. (2000). "Multisection CT: Scanning Techniques and Clinical Applications." 20, 1787-1806.

Schulze (2010). "http://www.dietmar-schulze.de/grdle1.pdf".

Shahinpoor, M. (1983). *Advances in the Mechanics and the Flow of Granular materials*, 1st ed., Trans Tech publication, Germany.

Siemens Medical, (2011). "http://www.medical.siemens.com/siemens/zh_CN/gg_ct_FBAs/files/brochures/CT_History_and_Technology.pdf".

Sinka, J. C., Cocks, A. C. F., and Tweed, J. H. (2001). "Constitutive data for powder compaction modeling." *Journal of Engineering Materials and Technology*, 123(2), 176-183.

Sumner, E. D., Thompson, H. O., Poole, W. K., and Grizzle, J. E. (1966). "Particle Size Distribution and Hopper Flow Rates." *Jnl pharm*. Sci., 55, 1441-1446.

Takei, M., Doh, D., and Ochi, M. (2007). "Electrical CT Image Reconstruction Technique for Powder in Petroleum Refinery Process." *Powder Technology*, 44(3), 481-490.

Thompson, K. E., Willson, C. S., and Zhang, W. (2006). "Quantitative complex reconstruction of particulate materials from microtomography images." *Powder Technology*, 163, 169-182.

Train, D. (1957). "Transmission of forces through a powder mass during the process of pelleting." *Trans. Inst. Chem. Eng*., 35, 258–266.

Yang, Y. (2011). "Measurement of spatial variation of density of compacted powders using synchrotron microtomography." MS Thesis, Louisiana State University, Baton Rouge, LA.

APPENDIX A: PARTICLES UNDER DIFFERENT COMPACTION STRAINS IN TWO CONFIGURATIONS OF POWDER ANALYSIS.

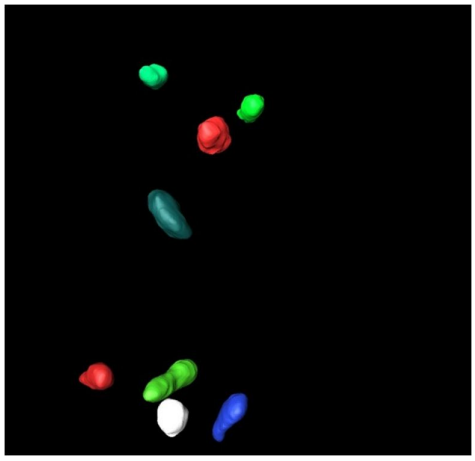

Figure: Particles at 0% compaction strain of zone I in configuration I.

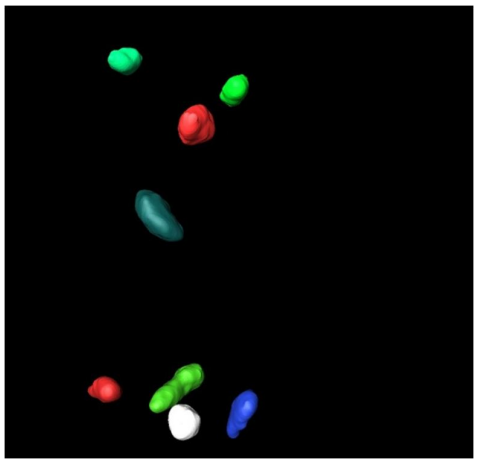

Figure: Particles at 5% compaction strain of zone I in configuration I.

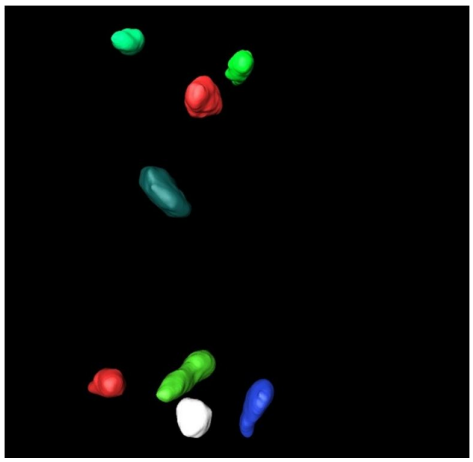

Figure: Particles at 10% compaction strain of zone I in configuration I.

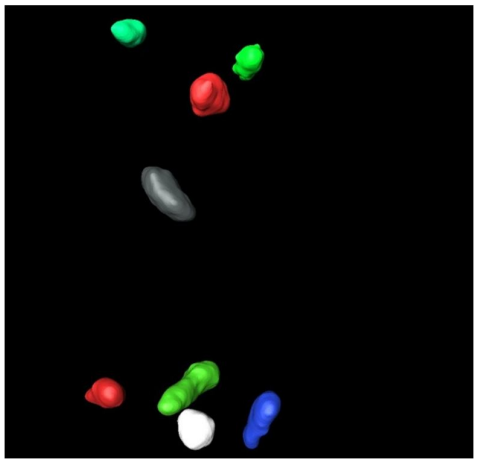

Figure: Particles at 15% compaction strain of zone I in configuration I.

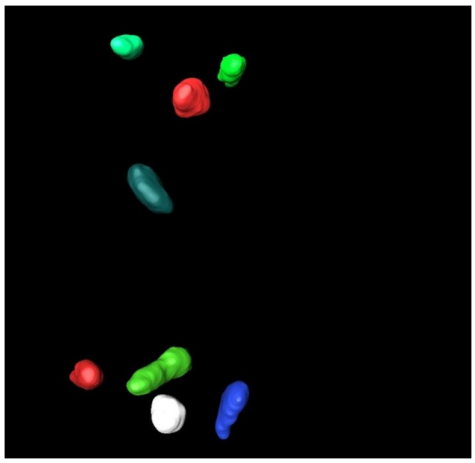

Figure: Particles at 20% compaction strain of zone I in configuration I.

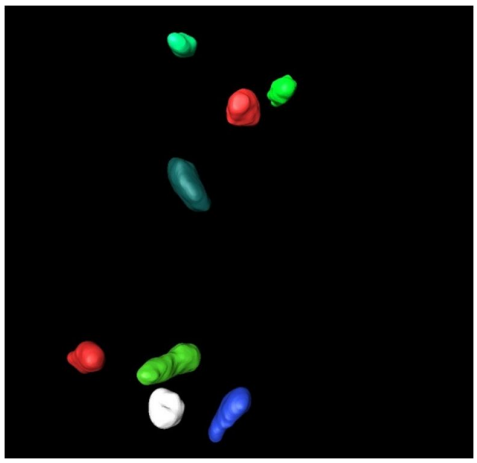

Figure: Particles at 25% compaction strain of zone I in configuration I.

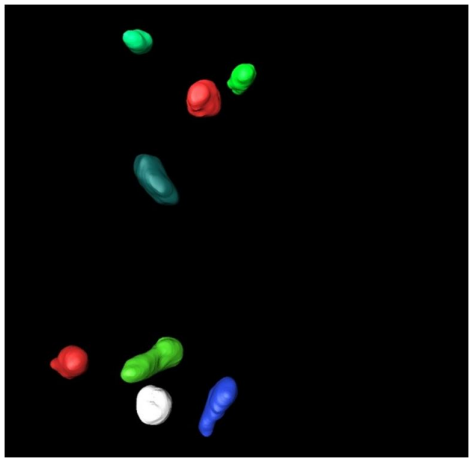

Figure: Particles at 30% compaction strain of zone I in configuration I.

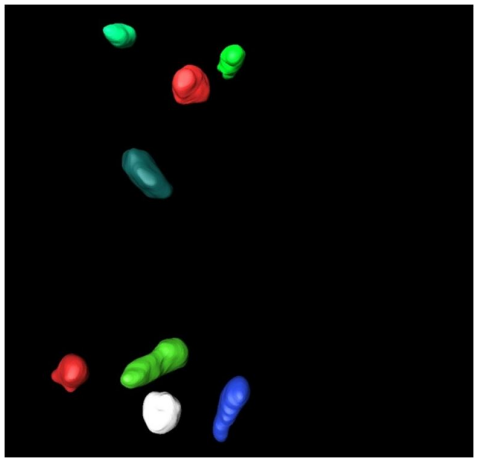

Figure: Particles at 35% compaction strain of zone I in configuration I.

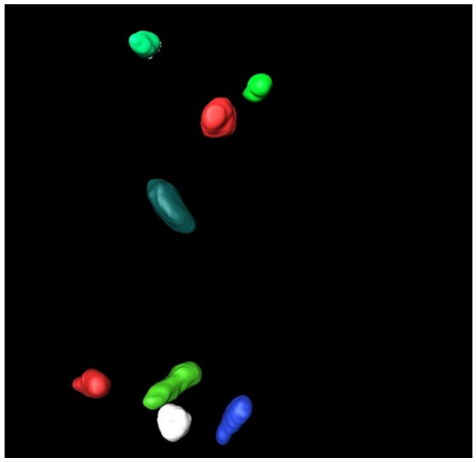

Figure: Particles at 40% compaction strain of zone I in configuration I.

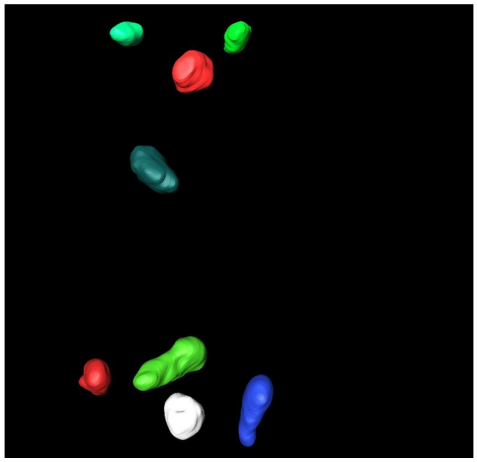

Figure: Particles at 45% compaction strain of zone I in configuration I.

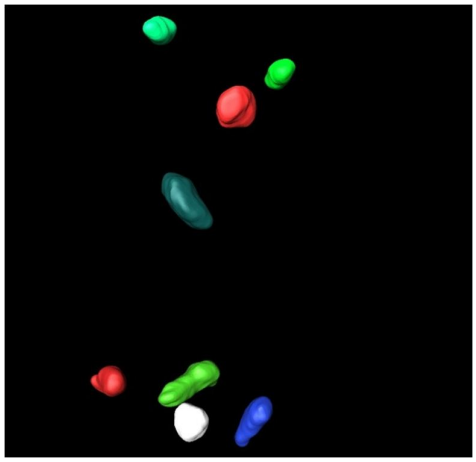

Figure: Particles at 50% compaction strain of zone I in configuration I.

Figure: Particles at 0% compaction strain of zone II in configuration I.

Figure: Particles at 5% compaction strain of zone II in configuration I.

Figure: Particles at 10% compaction strain of zone II in configuration I.

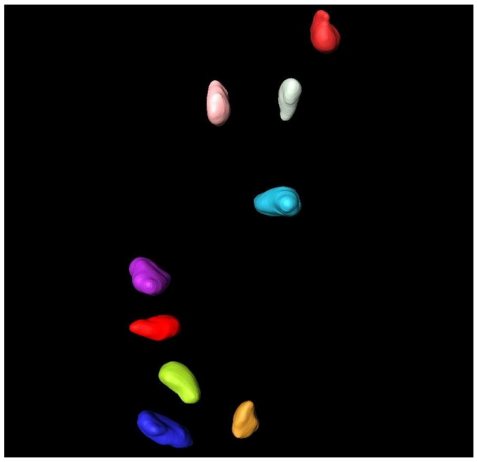

Figure: Particles at 15% compaction strain of zone II in configuration I.

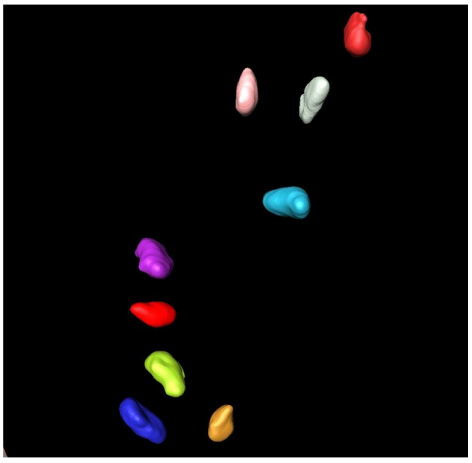

Figure: Particles at 20% compaction strain of zone II in configuration I.

Figure: Particles at 25% compaction strain of zone II in configuration I.

Figure: Particles at 30% compaction strain of zone II in configuration I.

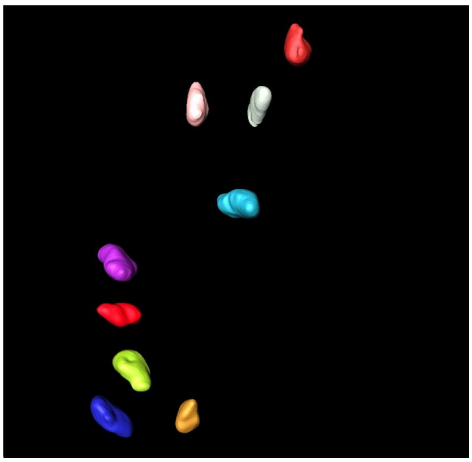

Figure: Particles at 35% compaction strain of zone II in configuration I.

Figure: Particles at 40% compaction strain of zone II in configuration I.

Figure: Particles at 45% compaction strain of zone II in configuration I.

Figure: Particles at 50% compaction strain of zone II in configuration I.

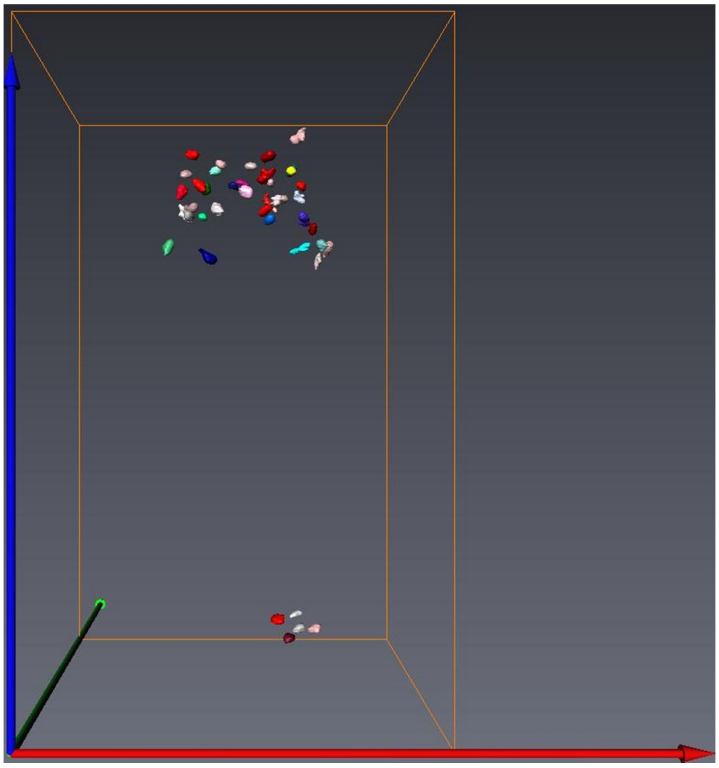

Figure: Particles at 0% compaction strain in configuration II.

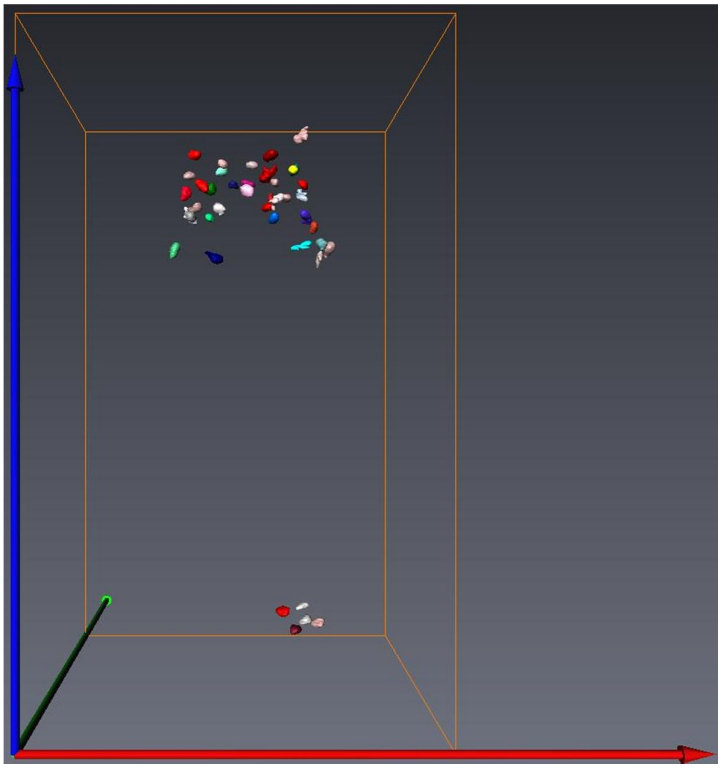

Figure: Particles at 3% compaction strain in configuration II.

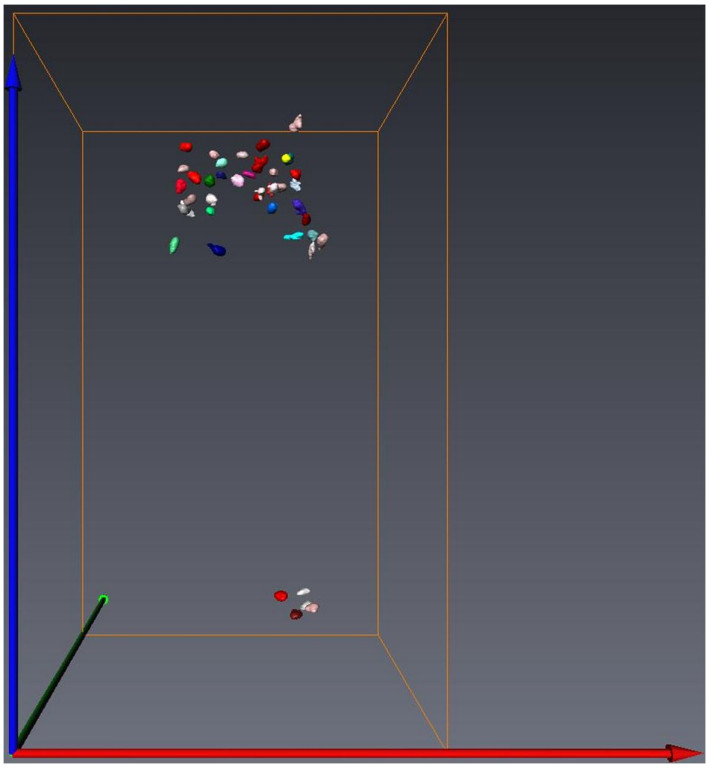

Figure: Particles at 6% compaction strain in configuration II.

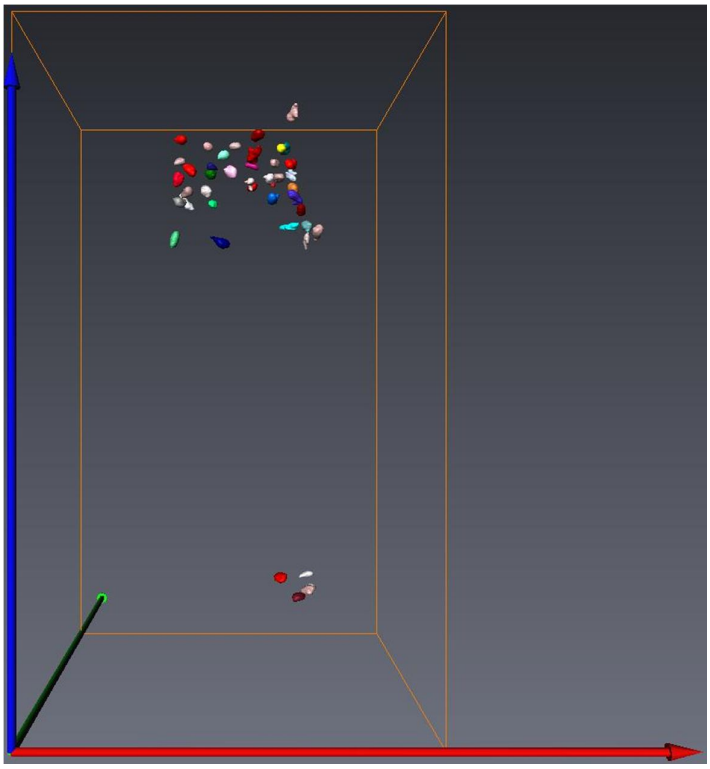

Figure: Particles at 9% compaction strain in configuration II.

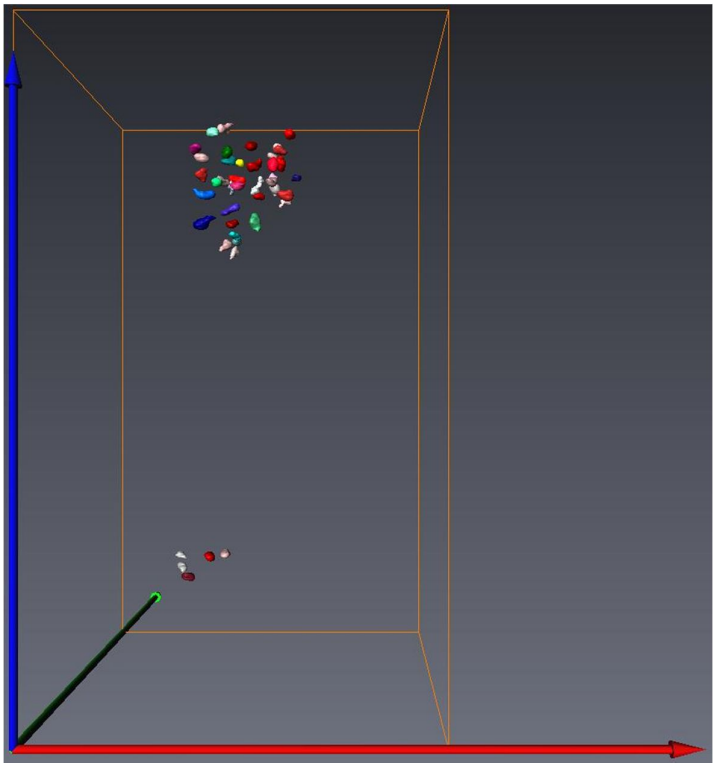

Figure: Particles at 12% compaction strain in configuration II.

APPENDIX B: IMAGES OF TRACKED PARTICLES UNDER DIFFERENT PENETRATION DEPTHS DURING CPT.

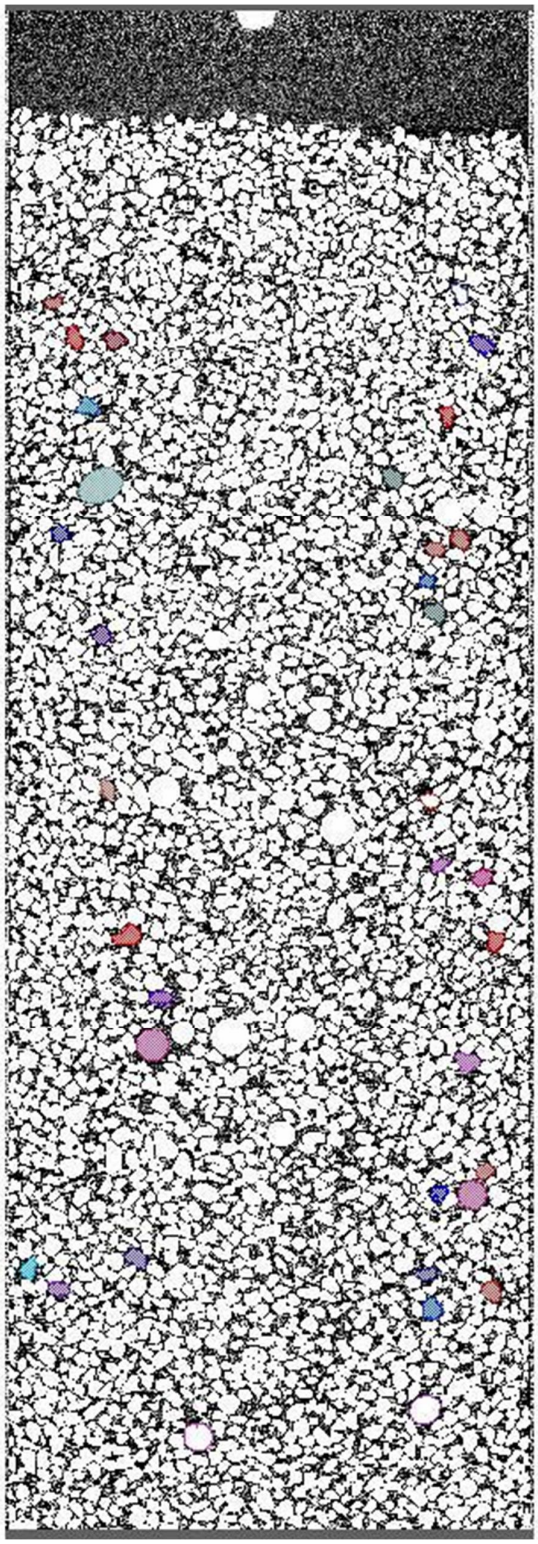

Figure: Penetration at 0 mm.

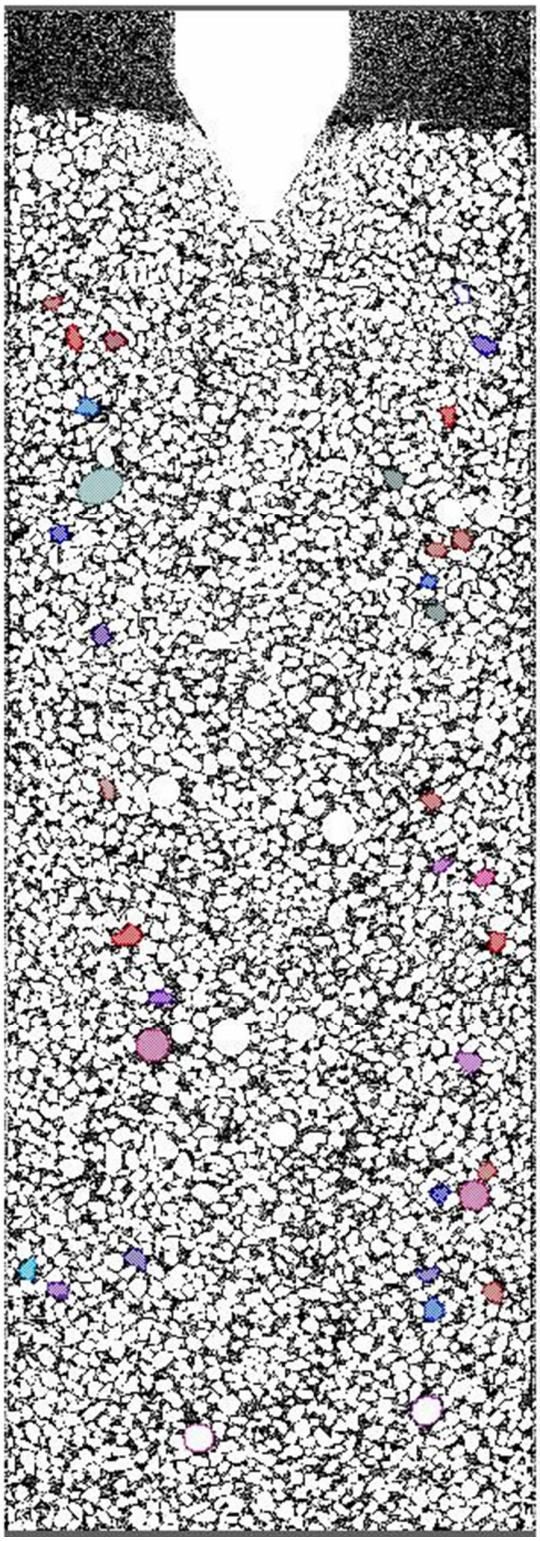

Figure: Penetration at 2 mm.

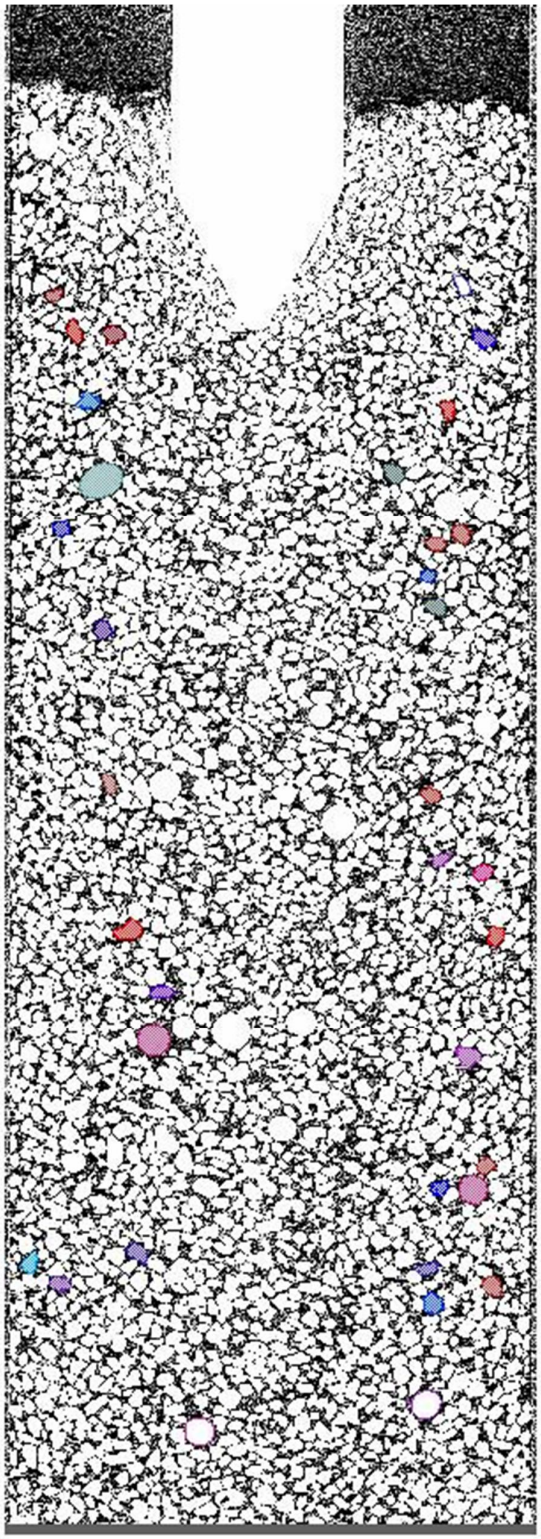

Figure: Penetration at 4 mm.

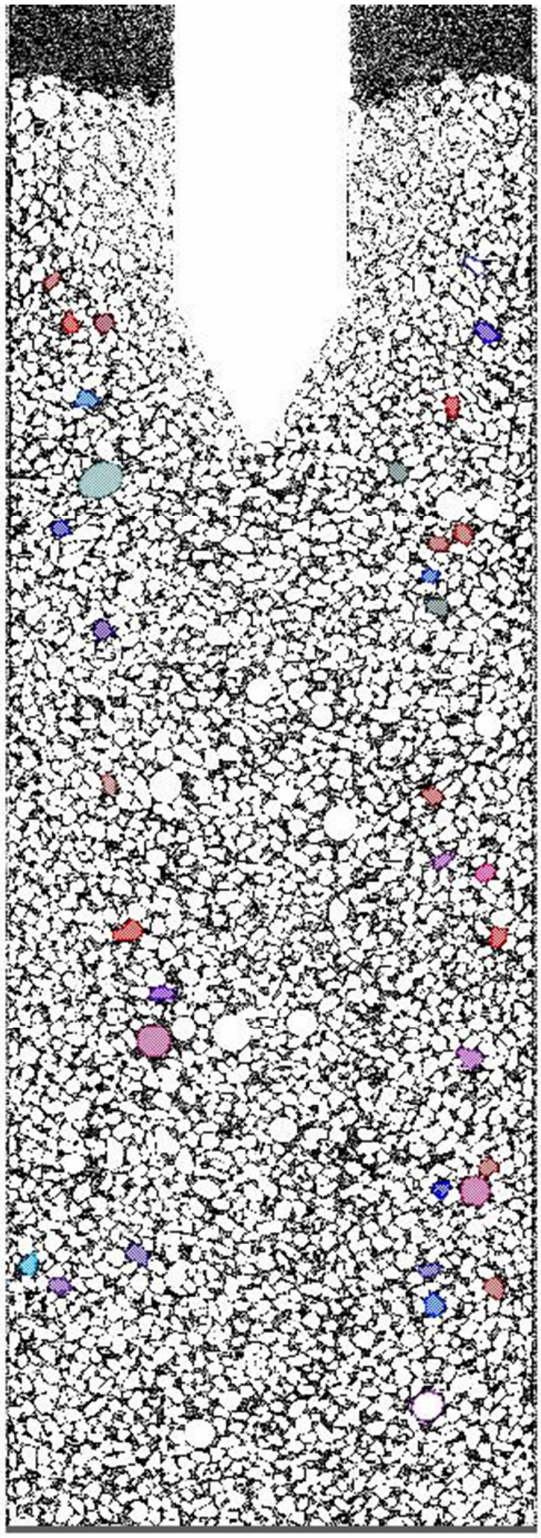

Figure: Penetration at 6 mm.

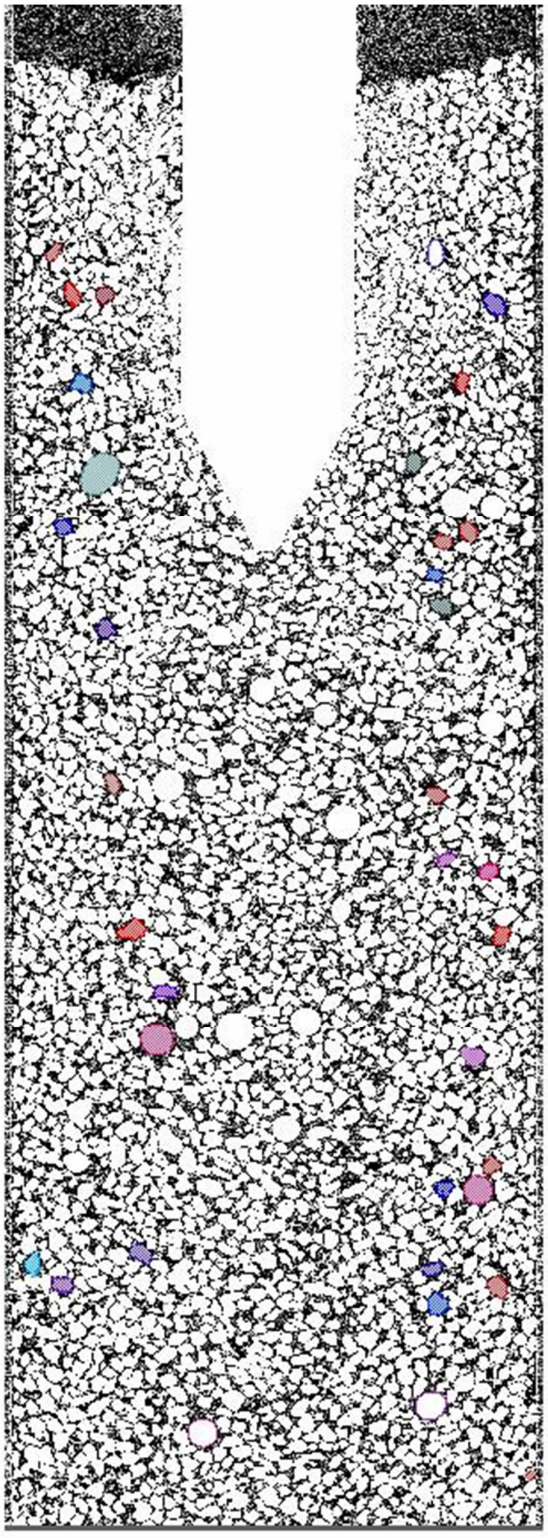

Figure: Penetration at 8 mm.

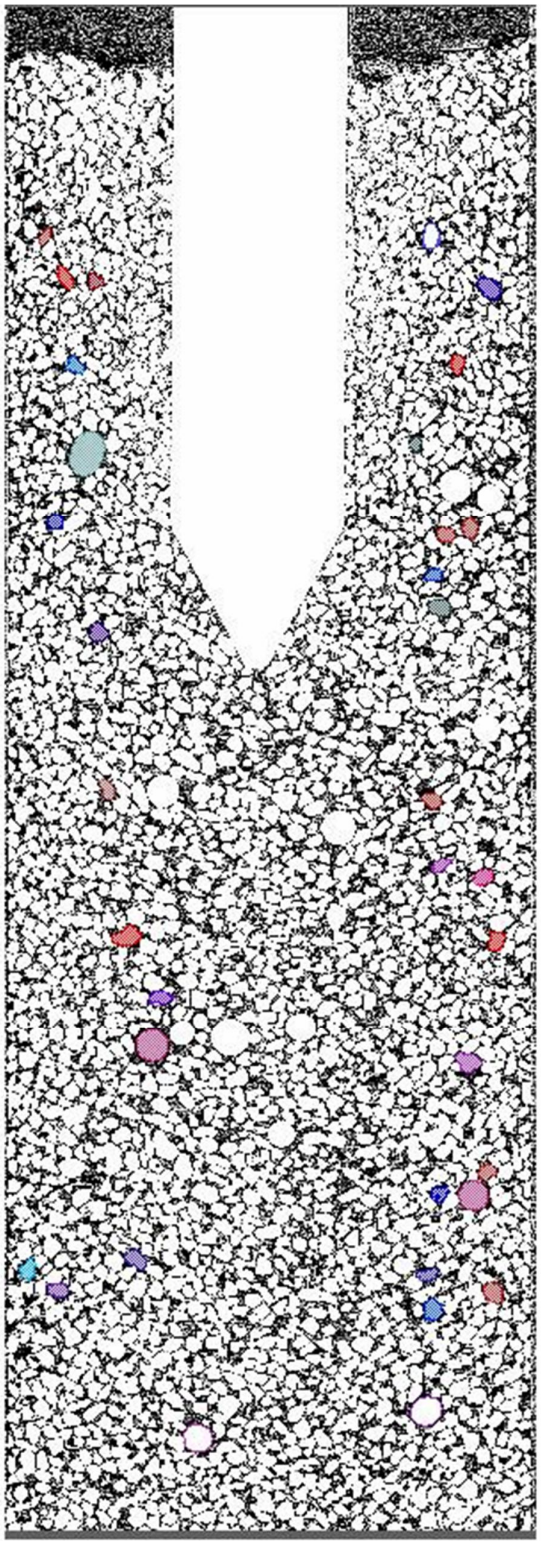

Figure: Penetration at 10 mm.

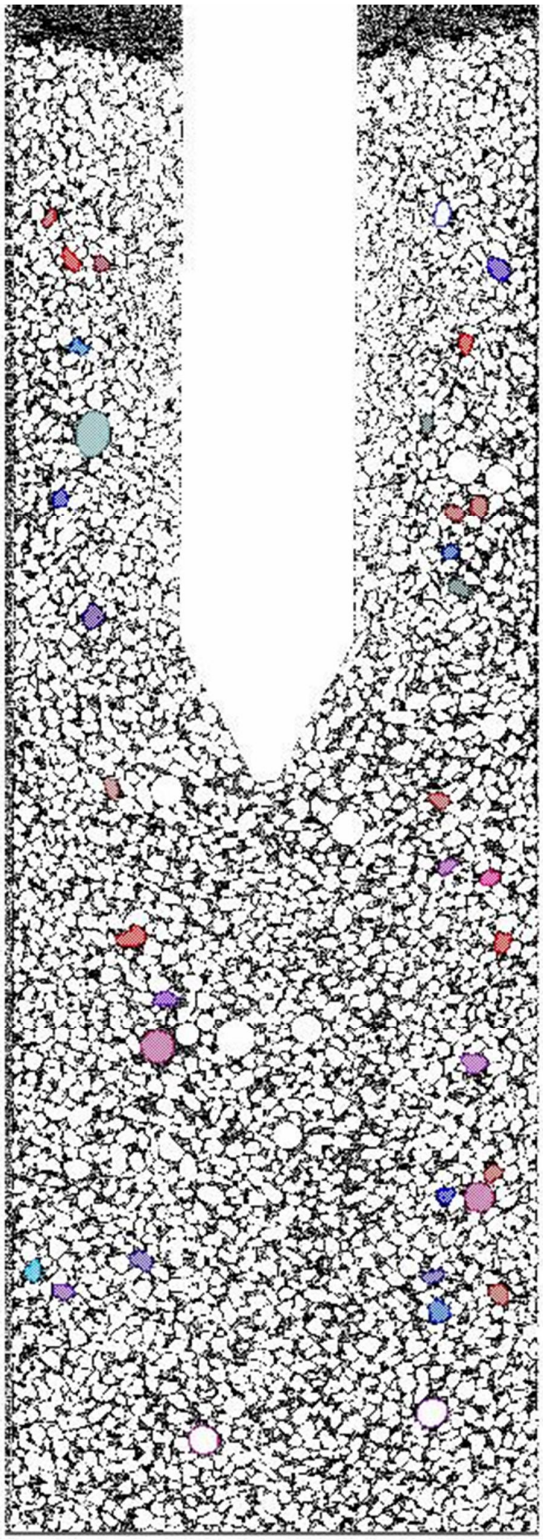

Figure: Penetration at 12 mm.

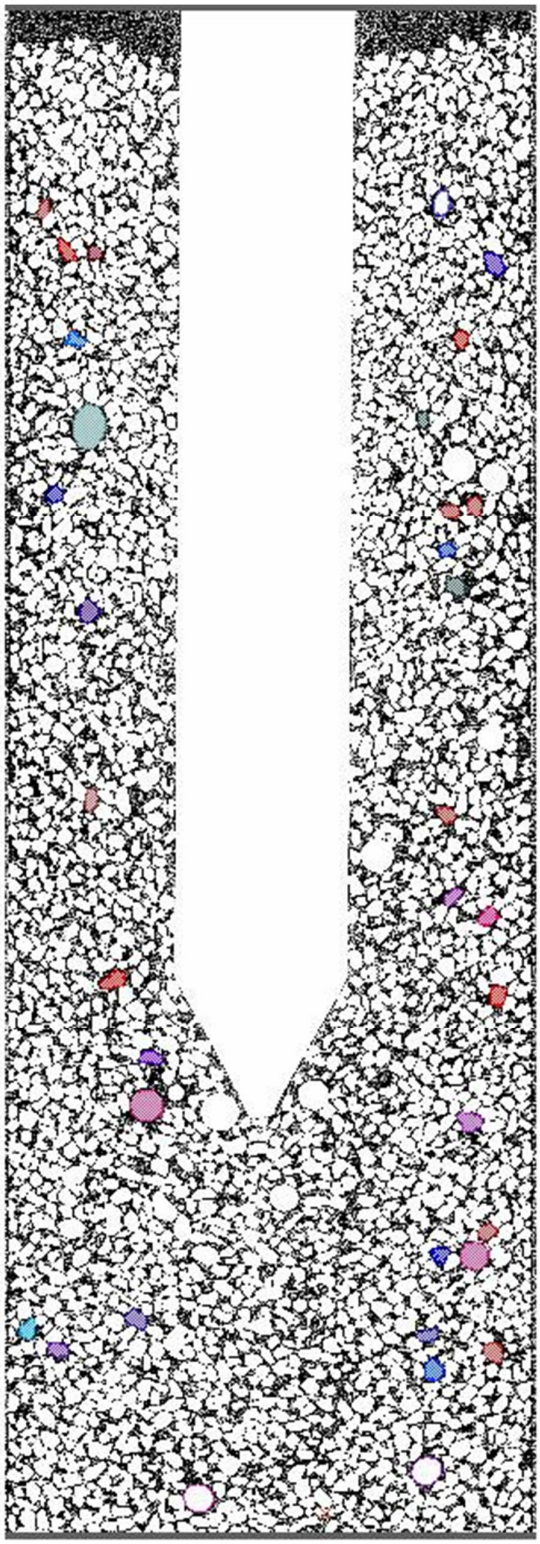

Figure: Penetration at 17 mm.

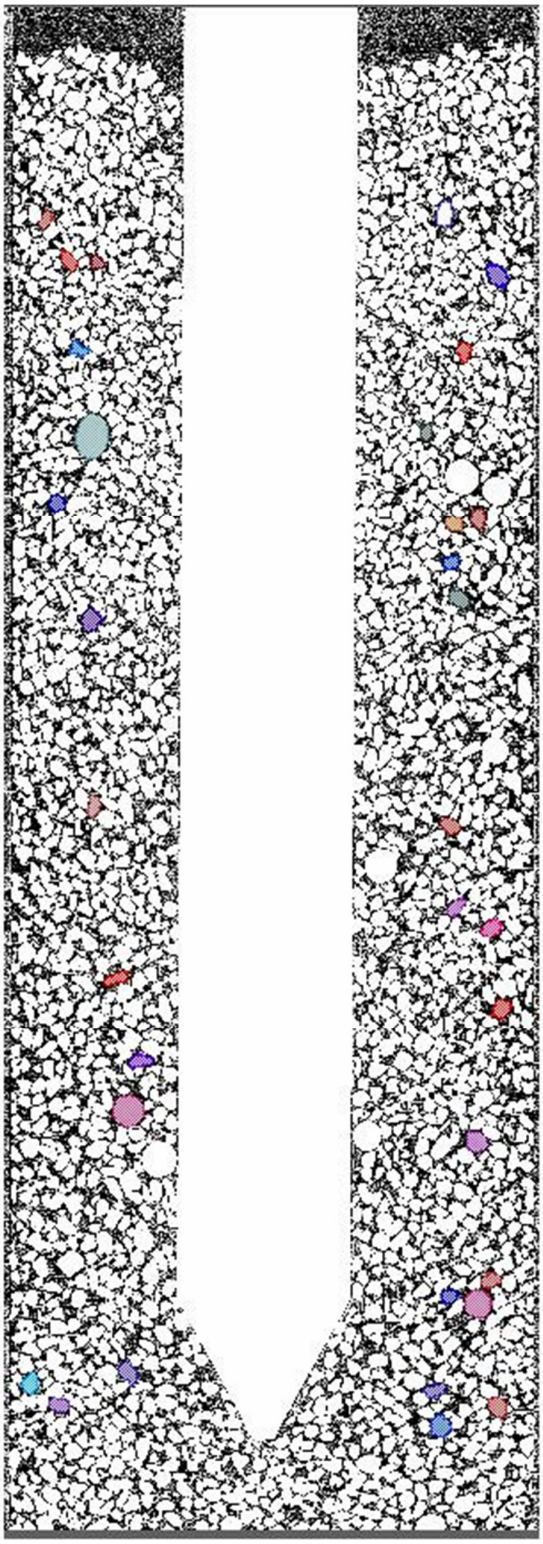

Figure: Penetration at 22 mm.

VITA

The author, Md. Nafiul Haque, was born on Wednesday, January 1, 1986, in Thakurgaon, a small town of Bangladesh. He moved with his family to Dhaka, the capital of Bangladesh in 1992. He finished his high school from Notredame College in 2002, and then enrolled in the Bangladesh University of Engineering and Technology (BUET) to pursue a bachelor's degree. He received a Bachelor of Science in Civil Engineering degree in January, 2008. After receiving his degree, he moved to Singapore in June of 2008 to work in a private company named Ground Instrumentation and Engineering (GIE) as a geotechnical engineer. His task was to monitor various soil instrumentation and soil investigation projects. He left the company on June, 2009, and returned to his own country. He came to the USA in the Spring of 2010 to pursue his master's degree at Louisiana State University (LSU). He worked with Dr. Khalid Alshibli for one and half years as a research assistant in anticipation of earning his Master of Science degree in Civil Engineering in December of 2011. Md. Haque hopes to attend civil engineering school in the Fall of 2011 to pursue a doctorate degree.